

© Copyright by Yanan Wang 2014

All Rights Reserved

**SYNTHESIS AND OPTICAL SPECTROSCOPY STUDY OF TWO-DIMENSIONAL
CRYSTALS: GRAPHENE AND BEYOND**

A Dissertation

Presented to

the Faculty of the Department of Electrical and Computer Engineering

University of Houston

In Partial Fulfillment

Of the Requirements for the Degree

Doctor of Philosophy

in Electrical Engineering

by

Yanan Wang

August 2014

**SYNTHESIS AND OPTICAL SPECTROSCOPY STUDY OF TWO-DIMENSIONAL
CRYSTALS: GRAPHENE AND BEYOND**

Yanan Wang

Approved:

Chair of the Committee
Jiming Bao, Assistant Professor,
Electrical and Computer Engineering

Committee Members:

Dmitri Litvinov, John and Rebecca
Moores Professor,
Electrical and Computer Engineering
Vice Provost and Dean of the Graduate
School

Shin-Shem Steven Pei, Professor,
Electrical and Computer Engineering

Viktor Hadjiev, Research Scientist,
Mechanical Engineering

Haibing Peng, Assistant Professor,
Physics

Suresh K. Khator, Associate Dean,
Cullen College of Engineering

Badri Roysam, Professor and Chair,
Electrical and Computer Engineering

ACKNOWLEDGEMENTS

I would like to express my deepest gratitude to my advisor, Dr. Jiming Bao for his great guidance and advice throughout my study and research at university of Houston.

I thank Dr. Shin-Shem Pei, Dr. Dmitri Litvinov, Dr. Viktor G. Hadjiev, and Dr. Haibing Peng for their great advice and their willingness to be on my dissertation committee.

I thank Dr. Francisco Robles-Hernandez, Dr. Paul Ruchhoeft, and Dr. Han Q. Le for their valuable discussion and generous offering of experiment facilities.

I thank all the collaborators and all the group mates from Dr. Jiming Bao's group. Special thanks go to Sirui Xing and Su-chi Chang from Dr. Shin-Shem Pei's group for their contribution to this research work.

Last but not least, I deeply thank my parents for their unconditional love, support, and sacrifice.

**SYNTHESIS AND OPTICAL SPECTROSCOPY STUDY OF TWO-DIMENSIONAL
CRYSTALS: GRAPHENE AND BEYOND**

An Abstract

of a

Dissertation

Presented to

the Faculty of the Department of Electrical and Computer Engineering

University of Houston

In Partial Fulfillment

Of the Requirements for the Degree

Doctor of Philosophy

in Electrical Engineering

by

Yanan Wang

August 2014

ABSTRACT

The discovery of graphene, a single atomic layer of hexagonally packed carbons, can be considered as the opening of an epic of two-dimensional (2D) materials. With the restriction in dimensions and the weak interlayer reactions, these isolated layer crystals have exhibited distinctive properties from their bulk forms. Moreover, integrating heterogeneous layered crystals is expected as a promising approach to produce materials with complex structures and well-engineered properties.

Therefore, this dissertation emphasizes on synthesizing ideal 2D building blocks, graphene and transition metal dichalcogenides (TMDCs) crystals via chemical vapor deposition (CVD), exploring their optical spectroscopic signatures, and verifying the practicability of artificial stacking with the simplest case, twisted bilayer graphene (tBLG). After evaluating several key factors, millimeter size of monolayer hexagon graphene crystals have been harvested with designed recipe. Synthesis of bilayer hexagon graphene domains, monolayer and few-layer MoS₂ and WS₂ crystals in micrometer size have also been demonstrated. In addition, hundreds-of-micrometer sized twisted bilayer graphene domains have been achieved by artificial staking of two monolayer graphene hexagons, of which crystal orientation mismatch can be directly estimated by the misalignment of edges. Raman and photoluminescence spectroscopy are utilized not only to determine the number of layers and the quality of as-grown samples, but also to characterize the underlying crystalline and even electronic structures. This study provides valuable insight of synthesizing, processing, and characterizing 2D crystals in engineered approaches and paves a way for introducing them into electronic and photonic application.

TABLE OF CONTENTS

Abstract	vii
Table of Contents	viii
List of Figures	xii
List of Tables	xxiii
Chapter 1 Introduction	1
Chapter 2 Basic Properties of Graphene	5
2.1 Monolayer Graphene	6
2.2 Bernal Stacked Bilayer Graphene	8
2.3 Twisted Bilayer Graphene- Graphene Superlattices	9
Chapter 3 Synthesis of Hexagon Graphene Crystals by Designed Chemical Vapor Deposition Process	12
3.1 Synthesis Methods of Graphene	13
3.1.1 Mechanical Exfoliation	13
3.1.2 Liquid Phase Exfoliation	15
3.1.3 Thermal Decomposition of SiC	16
3.1.4 Chemical Vapor Deposition on Metals	17
3.1.5 Comparison of Different Synthesis Methods	19
3.2 Chemical Vapor Deposition of Graphene	20
3.2.1 Overview of Chemical Vapor Deposition	20

3.2.2 Chemical Vapor Deposition System	20
3.2.3 Experiment Details of Chemical Vapor Deposition of Graphene	22
3.3 Key Factors in Chemical Vapor Deposition of Graphene	23
3.3.1 Type of Metal Substrates and Growth Kinetics	23
3.3.2 Pretreatment of Cu Foils	27
3.3.3 Methane and Hydrogen Concentration	33
3.3.4 Duration of Growth	37
3.3.5 Rules of Thumb	38
3.4 Synthesis of Hexagon-Shaped Graphene Crystals	39
Chapter 4 Transfer and Artificial Stacking of Graphene Crystals	44
4.1 Transfer Methods	44
4.1.1 Removal of Catalytic Metal Substrates	45
4.1.2 Polydimethylsiloxane (PDMS) Assistant Transfer	46
4.1.3 Polymethyl-Methacrylate (PMMA) Assistant Transfer	47
4.1.4 Thermal Release Tape Assistant Large-Scale Transfer	48
4.2 Experiment Details of PMMA Assistant Wet Transfer	49
4.2.1 General Protocol	49
4.2.2 Removal of Back Side Graphene by Plasma Etching	51
4.2.3 Minimizing of Cracking during Transfer	53
4.2.4 PMMA Residue /Substrate Doping Effects and Post-Annealing	54
4.2.5 Visualization of Graphene by Oxidizing Cu Foils	56

4.3 Transfer of Monolayer Graphene Crystals	58
4.4 Creation of Twisted Bilayer Graphene by Artificial Stacking	60
Chapter 5 Raman Spectroscopy Study of Hexagon Graphene Crystals	65
5.1 Principle of Raman Spectroscopy	66
5.1.1 Raman Scattering Effects	66
5.1.2 Raman Spectroscopy	68
5.1.3 Phonon Modes	69
5.1.4 Raman Modes in Graphene	69
5.1.5 Rules of Thumb	72
5.2 Experimental Details of Raman Measurement	75
5.2.1 Overview of Dispersive Raman Microscopy	75
5.2.2 Operation of Commercial Raman Microscopes	77
5.2.3 Setups and Operation of Lab-Built Raman Systems	78
5.2.4 Spectrum Analysis	79
5.3 Raman Spectroscopy Study of Monolayer Hexagon Graphene Crystals	80
5.3.1 Uniformity	80
5.3.2 Defects, Edges and Boundaries	83
5.3.3 Dispersive Behaviors	87
5.3.4 Summary	89
5.4 Raman Spectroscopy Study of Bilayer Hexagon Graphene Domains Synthesized by CVD	90

5.4.1 Overview	90
5.4.2 Raman Features of Bernal Stacked Bilayer Graphene	91
5.4.3 Raman Features of Twisted Bilayer Graphene — G Resonance	96
5.4.4 Raman Features of Twisted Bilayer Graphene — Folded Phonon Modes	101
5.4.5 Raman Features of Twisted Bilayer Graphene — Enhancement of 2D Band	107
5.5 Raman Spectroscopy Study of Bilayer Graphene Domains Synthesized by Artificial Stacking	112
Chapter 6 Synthesis and Optical Spectroscopy Study of 2D TMDCs	116
6.1 Overview of 2D TMDCs	116
6.2 Synthesis of MoS₂ and WS₂ Crystals by Chemical Vapor Deposition	117
6.2.1 Synthesis of MoS ₂ Crystals	118
6.2.2 Synthesis of WS ₂ Crystals	120
6.3 Optical Spectroscopy Study of MoS₂ and WS₂ Crystals	120
Chapter 7 Conclusions and Outlook	125
Reference	127
Appendix I: Journal Publications	148
Appendix II: Conference Presentations	150

LIST OF FIGURES

Figure 1.1 Atomic illustrations (a-d) and corresponding secondary electron microscope (SEM) images (e-h) of various graphitic carbon forms, with blue coordinate system arrows indicating degree of dimensionality.	1
Figure 2.1 Illustration of building carbon materials of all other dimensionalities from graphene .	5
Figure 2.2 Schematic drawings of graphene cells in real space (a) and in phase (reciprocal) space (b). (c) High resolution STM image of graphene on graphite substrate	6
Figure 2.3 3D representation of orbital diagram of carbon atom (a), sp^2 hybridization (b), and electronic band structure of graphene (c). The region near the Fermi level in one K point has been enlarged in the right panel	8
Figure 2.4 Schematic drawings of Bernal stacked graphene cells in real space: (a) top view, (b) side view with certain angle. The shaded rhombus in (a) indicates the conventional unit cell	8
Figure 2.5 3D representation of intrinsic AB-stacked BLG without band gap (a), and opening of band gap by changing the doping level through potassium adsorption (b)	9
Figure 2.6 Schematic drawings and corresponding STM images of tBLG superlattice with rotation angle of 3.5° (a) and 21° (b). (c) TEM images and diffraction patterns of tBLG with rotation angle of 6.0° , 7.3° , 15.2° , 21.8° (from left to right)	10
Figure 2.7 Low energy electron microscope images and corresponding diffraction patterns of a hexagon tBLG single crystal with rotation angle of 23° (a) and a twinning structure of AB-stacked (0°) and tBLG with rotation angle of 17° (b)	11

Figure 3.1 Schematic illustration of the main graphene production techniques developed in the past ten years	12
Figure 3.2 (a) Subcentimeter single-crystal graphene grains on oxidized copper (up) and on a SiO ₂ /Si wafer (down). (b) Roll-to-roll transfer of 30 in. graphene films. (c) Multilayer graphene film (up) and 3D graphene form (down) supplied by Graphene Supermarket	13
Figure 3.3 (a) Graphene on 300 nm SiO ₂ imaged with white light. (b) Same sample imaged with monochromatic light, the trace displays steplike changes in the contrast for 1, 2, and 3 layers. (c) Transfer of peeled graphene flakes from tape to SiO ₂ /Si substrate	14
Figure 3.4 (a) Illustration of LPE process. (b) Illustration of chemical reduction of graphite oxide. (c) Biodegradable nanocomposites of amyloid fibrils and graphene	16
Figure 3.5 (a) Schematic drawing of graphene-SiC ($6\sqrt{3} \times 6\sqrt{3}$)R30 unit cells. (b) STM images of hexagonal graphene lattice grown on Si-face with a (6×6) unit cell.....	16
Figure 3.6 (a) CVD grown graphene film on 3 in. 300 nm thick Ni on a SiO ₂ /Si substrate. (b) A transferred wafer-scale graphene film on a PET substrate. (c) Dark-field TEM image and corresponding diffraction pattern of CVD grown graphene film, scale bar 500nm	18
Figure 3.7 Different synthesis methods allow a wide choice in terms of size, quality, and price for any particular application	19
Figure 3.8 (a) Schematic of the CVD system applied for graphene growth in this study. (b-d) Photos of main components, heating furnace, mechanical pump and turbo pump, mass	

flow controller, respectively	21
Figure 3.9 (a-b) Raman mapping and schematic of a graphene domain grown on Cu with isotopic carbon labels. (c) Growth kinetics in CVD-produced graphene on Ni and Cu	25
Figure 3.10 Binary phase diagrams of transition metals and carbon: (a) Ni-C, (b) Cu-C	25
Figure 3.11 SEM images for graphene islands with (a) hexagonal shape, (b) six-lobed flower shape, and (c) dendrite shape	27
Figure 3.12 Overview (a) and close-up (b) SEM images of graphene islands grown on Cu foil using our APCVD system	28
Figure 3.13 Morphology of graphene islands grown on Cu(100) (left), Cu(110) (middle), and Cu(111) (right) with different CH ₄ /H ₂ ratio by LPCVD (a-f), and APCVD (g-l). Scale bars are 5 μm except for 5d and 5j, which are 1 μm	29
Figure 3.14 SEM images of graphene grown on a Cu foil with different surface morphology ...	30
Figure 3.15 Typical SEM images of graphene samples produced with a H ₂ -rich (a) and O ₂ -rich (b) annealing process, respectively	32
Figure 3.16 SEM images of the inner (left) and outer (right) surfaces of Cu cylindrical foil after synthesis	33
Figure 3.17 SEM images of a graphene sample suffering H ₂ etching during a slow cooling process	34
Figure 3.18 The average size of graphene grains grown for 30 min at 1000 °C on Cu foil using 30 ppm methane in Ar mixture at 1 atm, as a function of partial pressure of hydrogen. Scales bars are 10 μm (top two images) and 3 μm (bottom two images)	35

Figure 3.19 SEM images of graphene samples grown with fixed CH ₄ flow rate (0.008 sccm) but varied H ₂ flow rate (35 sccm (a), 30 sccm (b), respectively)	36
Figure 3.20 A zoomed in view of graphene sample in Figure 3.19 (a)	37
Figure 3.21 Growth recipes for monolayer hexagon-shaped graphene single crystals (not in scale)	39
Figure 3.22 SEM images of as-grown samples under different conditions: (a) H ₂ -rich No. 1, (b) H ₂ -rich No. 2, (c) O ₂ -rich No. 1, with modest magnifications	41
Figure 3.23 Zoom-in SEM images of as-grown samples under different conditions: (a) H ₂ -rich No. 1, (b) H ₂ -rich No. 2, (c) O ₂ -rich No. 1, (d) O ₂ -rich No. 2, (e) O ₂ -rich No. 3	41
Figure 3.24 Growth recipe for bilayer hexagon graphene samples by CVD (not in scale)	43
Figure 4.1 Removal of catalytic metal substrate by chemical etching (a), electrochemical reaction (b), and mechanical exfoliation (c)	45
Figure 4.2 (a) Transfer process with a pre-patterned PDMS stamp. (b) PMMA assistant transfer process applied on perforated substrates and flat substrates. (c) Thermal release tape based roll-to-roll technique to realize transferring of 30-inch size of graphene.	48
Figure 4.3 Flow chart of PMMA assistant wet transfer applied in this study	49
Figure 4.4 Optical images of transferred graphene samples on SiO ₂ /Si substrate without plasma etching of back side graphene (left), with 5 min Ar plasma etching (middle), with 5 min O ₂ plasma etching (right)	51
Figure 4.5 (a) Comparison of Raman spectra collected from clean SiO ₂ /Si surface and marks of back side graphene on one O ₂ plasma treated sample. (b) Raman spectra of graphene	

samples treated with 5 min Ar plasma and O ₂ plasma back etching, respectively	52
Figure 4.6 Oxidation tests of Cu foils without plasma etching of back side graphene (left), with 5 min Ar plasma etching (middle), with 5 min O ₂ plasma etching (right)	53
Figure 4.7 Photo of graphene domains on oxidized Cu foil	56
Figure 4.8 (a) Optical microscope image of a graphene domain on oxidized Cu foil. (b) A typical Raman spectrum collected from the graphene domain shown in (a)	57
Figure 4.9 (a) Optical microscope image of a graphene domain transferred from oxidized Cu foil onto a 300 nm SiO ₂ /Si substrate. (b) A typical Raman spectrum collected from the graphene domain shown in (a)	57
Figure 4.10 Typical optical microscope images of H ₂ -rich sample (a-b), and O ₂ -rich sample (c) under different magnification	58
Figure 4.11 Typical Raman spectra collected from the H ₂ -rich and O ₂ -rich graphene domain shown in Figure 4.10, respectively	59
Figure 4.12 (a) Optical microscope image of a bilayer graphene sample prepared by artificial stacking of two H ₂ -rich graphene layers. (b) Typical Raman spectra collected from single-layer area and the overlay area outlined in black dash line in (a)	61
Figure 4.13 Optical microscope images of bilayer graphene samples prepared by “together” stacking (a) and “separate” stacking (b) of two O ₂ -rich layers	62
Figure 4.14 Typical Raman spectra collected from single-layer area and overlay areas on samples prepared by “together” stacking and “separate” stacking of two O ₂ -rich layers: overview (a), enlarged view of G band (b), and 2D band (c)	63

Figure 4.15 Photos of PMMA/graphene membrane floating on $\text{Fe}(\text{NO}_3)_3$ solution (a), and bilayer graphene sample transferred onto SiO_2/Si substrate by artificial stacking (b)	64
Figure 5.1 Schematic drawings of Rayleigh and Raman scattering from molecule vibration (a), energy level diagram (b), and spectral view (c)	66
Figure 5.2 (a) Schematic drawings of electronic and first-phonon Brillouin zones of graphene, and electronic dispersion. (b) Γ -point phonon-displacement patterns. (c) Phonon dispersion curve. (d) Raman spectra of pristine (top) and defected (bottom) graphene	70
Figure 5.3 Schematic drawings of first-order G band process, second-order process for the D band (intervalley process), the D'band (intravalley process), and 2D band	71
Figure 5.4 Schematic drawings of dispersive Raman spectroscopy (a) and confocal setup (b) ..	75
Figure 5.5 Commercial Raman system applied in this study	77
Figure 5.6 Configurations of the lab-built micro-Raman systems with visible laser sources (a) and ultraviolet (UV) laser (b)	78
Figure 5.7 Optical microscope image of a H_2 -rich monolayer graphene hexagon (a) and its corresponding Raman mappings of G band, D band, and 2D band (c-d)	80
Figure 5.8 Optical microscope image of another H_2 -rich monolayer graphene hexagon on the same sample (a) and its corresponding Raman mapping of G band, D band, and 2D band (c-d)	80
Figure 5.9 Spectra from point measurement of domains in Figure 5.7 and 5.8, respectively	81
Figure 5.10 Optical microscope image and Raman mappings of a H_2 -rich graphene hexagon ...	82

Figure 5.11 Optical microscope image (a), Raman mapping (c-d), and spectra from two point measurements (e) of single-layer graphene flake prepared by mechanical exfoliation	83
Figure 5.12 (a) Raman spectra obtained in three different regions of a HOPG sample, with excitation laser of 638 nm. (b) Schematic illustration of the atomic structure of the armchair and zigzag edges and first BZ of 2D graphite.	84
Figure 5.13 Optical microscope image (a) and corresponding Raman mapping (b-d) of merged H ₂ -rich hexagons with parallel edges. (e) Spectra measurement from center of domain (blue) and the boundary between domains (green)	85
Figure 5.14 Examples of ordered (a) and disordered (b) grain boundaries	86
Figure 5.15 Optical microscope image (a) and corresponding Raman mapping (b-d) of other merged H ₂ -rich hexagons with rotated edges. (e) Spectra measurement from center of domain (blue) and the boundary between domains (green)	86
Figure 5.16 Raman spectra of a monolayer domain under different laser excitation	88
Figure 5.17 (a) Raman spectra of nanographites for five different laser energy values. (b) Plot of Raman position of 2D band versus excitation laser energy, based on spectra in Figure 5.16	89
Figure 5.18 A typical SEM image of CVD synthesized bilayer graphene domains	90
Figure 5.19 (a) Distribution results from the SEM measurements of over 100 graphene bilayer domains. (b-f) SEM images of typical individual bilayer domains on Cu foil with various rotation angles. The scale bars are 2 μm	91

Figure 5.20 Typical Raman spectra of single-layer and bilayer flakes prepared by mechanical exfoliation	92
Figure 5.21 (a) Electronic band structure of Bernal stacked bilayer graphene (b) The four second-order Raman processes of 2D band	93
Figure 5.22 Fitting result of 2D band in Figure 5.20	94
Figure 5.23 SEM image and Raman spectra of a typical 0-degree bilayer domain	94
Figure 5.24 Fitting results of 2D band in Figure 5.23, with four Lorentzians (left) and three Lorentzians (right), respectively	96
Figure 5.25 SEM image (a) and Raman mappings (b) of a bilayer graphene island consisting of a twinning structure on the second layer	96
Figure 5.26 Raman spectra of bilayer island shown in Figure 5.25	97
Figure 5.27 (a) Raman spectra of 13-degree domain under different laser excitation. (b) Plot of normalized G band intensity versus excitation laser energy (black squares) and fitting result of Gaussian (red line)	98
Figure 5.28 SEM image (a) and Raman mappings at 532 nm (b) of a single crystal bilayer graphene island. (c) Plot of normalized G band intensity versus excitation laser energy (black squares) and fitting result of Gaussian (red line)	99
Figure 5.29 SEM image (a) and Raman mappings at 638 nm (b) of a bilayer graphene island consisting of a twinning structure on the second layer. (c) Plot of G band intensity versus excitation laser energy for the resonant part	100
Figure 5.30 SEM image and Raman spectra of bilayer domain with rotation angle about 25°, with	

excitation of 363.8 nm laser	101
Figure 5.31 Raman spectra of tBLGs with different rotation angles on a Si/SiO ₂ substrate. The * symbols point to the superlattice-induced Raman peaks. Curve coloring corresponds to the excitation laser energy: 1.96 eV (red), 2.41 eV (green), and 2.54 eV (blue)	102
Figure 5.32 Raman spectra of a series of twisted bilayer domains show enhancement in G band under the excitation of 363.8 nm laser	104
Figure 5.33 Enlarged views of Figure 5.26 and Figure 5.27, respectively, for the 13-degree bilayer domain with G resonance around 532 nm	105
Figure 5.34 Observed phonon frequencies as a function of rotation angle	105
Figure 5.35 Schematic drawings of tBLG superlattice with rotation angle of 13.2° in real space (a) and in reciprocal space (b). (c) Calculated (solid line) and experimental (open circles) folded phonon frequencies as a function of reciprocal wave vector of superlattice	107
Figure 5.36 Normalized Raman spectra of 0-degree and 13-degree domain in the twinning structure shown in Figure 5.25, under different laser excitation	108
Figure 5.37 Raman spectra of single-layer (in black) and twisted bilayer graphene (in red) with rotation angles of 9, 11, 13 and 16 degrees. Insets are scanning electron microscopy (SEM) images. The excitation laser wavelength is 638 nm. The scale bar is 5 μm	109
Figure 5.38 Normalized 2D band intensity of bilayer versus single-layer graphene as a function of the rotation angle	109
Figure 5.39 Raman spectra of single-layer (in black) and twisted bilayer (in red) graphene. Insets in (b) and (c) are SEM images of these tBLGs with large rotation angles near ~25°	109

.....	110
Figure 5.40 Example of two degenerate 2D Raman pathways involving an interband transition between the inner loops. The excitation laser is tuned below the G resonance of the tBLG	111
Figure 5.41 Schematic of sample; G band and 2D/G image showing CVD and artificial bilayer regions; and Raman spectra from single layer, CVD bilayer, and artificial bilayer. (scale bar 5 μm)	113
Figure 5.42 Optical microscope image (a), Raman mapping (b-c), and point measurements (d) of twisted bilayer domains prepared by artificial stacking	114
Figure 6.1 (a) 3D representation of typical TMDCs structure, with chalcogen atoms (X) in yellow and metal atoms (M) in grey. (b) Schematic drawings of structural polytypes: 2H (hexagonal symmetry), 3R (rhombohedral symmetry) and 1T (tetragonal symmetry)	116
Figure 6.2 Optical (a) and atomic force microscope (AFM) images of exfoliated MoS ₂ flake on SiO ₂ /Si substrate. Optical image of graphene-WS ₂ heterotransistor, scale bar 10 μm	117
Figure 6.3 Schematic of the CVD system applied for MoS ₂ growth in this study	118
Figure 6.4 Optical microscope images of upstream (a) and downstream (b) part of one MoS ₂ sample	119
Figure 6.5 Schematic of the CVD system applied for WS ₂ growth in this study	120
Figure 6.6 Optical microscope image and Raman spectra of typical single-layer and bilayer MoS ₂	

crystals. The laser excitation wavelength is 532 nm	121
Figure 6.7 Raman intensity mappings of (a) E_{2g}^1 and (b) A_{1g} of a typical bilayer MoS_2 grain ..	121
Figure 6.8 SEM images (a-b) and Raman spectra (c) of MoS_2 domains with triangle and hexagon shape	122
Figure 6.9 (a) Schematic of electronic band structures of single-layer and bilayer MoS_2 . (b) Photoluminescence spectra of typical single-layer and bilayer MoS_2 crystals. The laser excitation wavelength is 532 nm	122
Figure 6.10 Typical Raman spectra of single-layer and bulk WS_2 , under 532 nm laser excitation	123
Figure 6.11 SEM (a) and AFM (b) images of WS_2 triangles. (c) Raman mapping of domain in (a), with 532 nm laser excitation. (d) Schematic of thickness distribution across the domain in (b)	123
Figure 7.1 Building van der Waals heterostructures with 2D crystals as Lego blocks	125

LIST OF TABLES

Table 3.1 Properties of graphene obtained from different methods	20
Table 3.2 Properties of graphene obtained from CVD on different metals	23
Table 3.3 Summary of growth parameters and corresponding outcomes of monolayer hexagon-shaped graphene single crystals	40
Table 3.4 Comparison between latest reported results and O ₂ -rich results from this study for large size graphene single crystals growth	42
Table 5.1 Experimental Rules of G band and 2D band	73
Table 5.2 Characteristic Raman peaks for monolayer graphene with 532 nm laser excitation ...	89
Table 5.3 Information of G band and 2D band from Figure 5.20	92
Table 5.4 Information of G band and 2D band from Figure 5.23	95
Table 5.5 Information of G band and 2D band from Figure 5.26	97
Table 5.6 Frequencies of the out-plane optical phonons at the Γ points (cm ⁻¹)	102
Table 5.7 Frequencies of the in-plane optical phonons at the Γ and K points (cm ⁻¹)	103
Table 5.8 Information of G band and 2D band from Figure 5.42	115

Chapter 1 Introduction

When the material size shrinks into nanoscale, the number of atoms or molecules forming the material becomes an influential role to the physicochemical properties and reactivity. In order to simplify the size and dimensional effects, it is preferable to classify the materials according to the number of dimension with expansion freedom (not restricted in nanosize). For instance, nanoparticles and nanodots, of which all dimensions are in the range of a few nanometers, belong to 0D category; and 3D materials usually refer to bulk materials¹⁻³. Figure 1.1 gives straightforward illustrations of dimensionality applying in typical sp^2 carbon allotropes⁴.

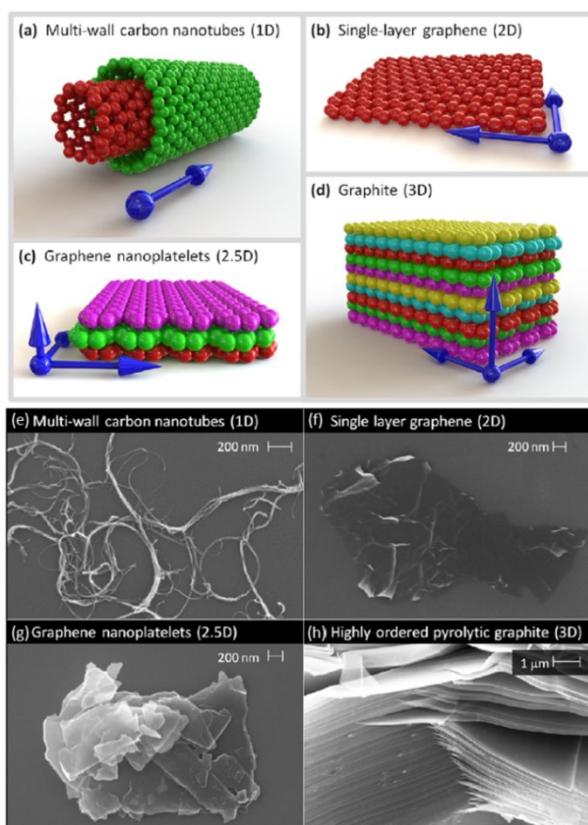


Figure 1.1 Atomic illustrations (a-d) and corresponding secondary electron microscope (SEM) images (e-h) of various graphitic carbon forms, with blue coordinate system arrows indicating degree of dimensionality.

Different from other low-dimensional materials, which have been synthesized and well developed for over decades, the existence of free-standing 2D material have remained conspicuous until graphene was first isolated from graphite via mechanical exfoliation and 2D semimetal behavior was observed in this atomically thin carbon film by Geim and Novoselov's group in 2004⁵⁻⁹. With the progress in synthesis techniques, this paradigm 2D material has rapidly risen to be one of the brightest stars in materials science and condensed-matter physics¹⁰⁻¹⁵. The richness of outstanding electronic, optical, thermal and mechanical properties, such as high carrier mobility (exceeding $10^5 \text{ cm}^2\text{V}^{-1}\text{s}^{-1}$ at room temperature), ultrawideband optical absorption (over visible range), high thermal conductivity ($\sim 5000 \text{ Wm}^{-1}\text{K}^{-1}$), and large Young's modulus ($\sim 1100 \text{ GPa}$), has been revealed in intense studies and spread this "graphene heat" far beyond the science community¹⁶⁻²². These exceptional properties have pushed graphene into applications in a large variety of fields, ranging from high-speed and radio-frequency logic devices, thermally and electrically, conductive reinforced composites, sensors, and photocatalysts, to transparent electrodes for liquid crystal displays and solar cells²³⁻³⁴. Noticeably, Geim and Novoselov were awarded the Nobel Prize in Physics in 2010 not only due to their groundbreaking experiments on graphene, but also because of the huge impacts this new class of materials has brought in fundamental research, transformative technologies, and even mass-production industries. With great ambition, graphene is expected to grow into the new silicon in future electronics and photonics^{25, 35}.

To actualize this aspiration, it is essential to prepare large-scale, high quality graphene samples with designable properties. Extensively studied polycrystalline graphene films appear not

adequate, due to the grain boundary scattering effects. Large size graphene single crystals are demanded here. Following the empirical rules, growth recipes of large size hexogen graphene single crystals are proposed and demonstrated with an atmospheric pressure chemical vapor deposition (CVD) system in this dissertation (Chapter 3). Over millimeter size monolayer and micrometer size bilayer domains have been achieved. Further, the feasibility of manipulating these monolayer crystals as building blocks to create complex structures, twisted bilayer graphene (tBLGs), is verified in Chapter 4. Beyond sophisticated energy spectrum measurements, Raman spectroscopy is employed to characterize the samples synthesized in this study, considering its applicability in both laboratory and mass production (Chapter 5). With this fast and non-destructive tool, some characteristic features, revealing structural and electronic properties of monolayer graphene crystals and twisted bilayer graphene domains, have been witnessed and investigated, which can serve as stepping stones for further studies.

In fact, graphene is only the very tip of the iceberg of 2D materials family. But as Geim pointed out in 2007, all experimental and theoretical efforts were focused on graphene, somehow ignoring the existence of other 2D crystals at that time¹⁴. This most likely resulted from the immaturity of isolation and synthesis techniques^{1,36}. After ten year of intense study, it seems most of the ‘low-hanging graphene fruits’ have already been harvested, researchers have now started paying more attention to other 2D crystals, such as isolated monolayers and few-layer crystals of hexagonal boron nitride (hBN), molybdenum disulphide, other dichalcogenides and layered oxides^{1,3,36-39}. Among them, 2D transition metal dichalcogenides need to be highlighted, since 3D TMDCs have already displayed a wide range of important properties such as semiconductivity,

half-metallic magnetism, superconductivity, or charge density wave, as well as having applications in various areas including lubrication, catalysis, photovoltaics, supercapacitors, and rechargeable battery systems³⁸. Therefore, 2D TMDCs crystals, MoS₂ and WS₂, are also studied in this dissertation (Chapter 6). The promising potentials of integrating graphene and these 2D crystals to form heterostructures with predefined properties are discussed as outlook in Chapter 7.

Chapter 2 Basic Properties of Graphene

Graphene, this simple form of two-dimensional sp^2 carbon, has attracted enormous attention given its extraordinary electronic, optical, thermal and mechanical properties, as listed in Chapter 1. Graphene can be described as the basic building block of all graphitic form. Fullerenes (0D) and carbon nanotubes (1D) can be thought as a graphene sheet wrapped up or rolled into a spherical and cylindrical shape, respectively, and graphite (3D) is made out of stacks of graphene layers (Figure 2.1)¹⁴. Restrictions of size in one or more dimensions can effectively change some properties of materials, but why graphene also shows distinctive properties from other low-dimensional allotropes? To interpret and eventually make use of these external characteristics, an overview picture from fundamental aspects, the crystalline and electronic band structure of graphene and its descendants, will be developed in this chapter.

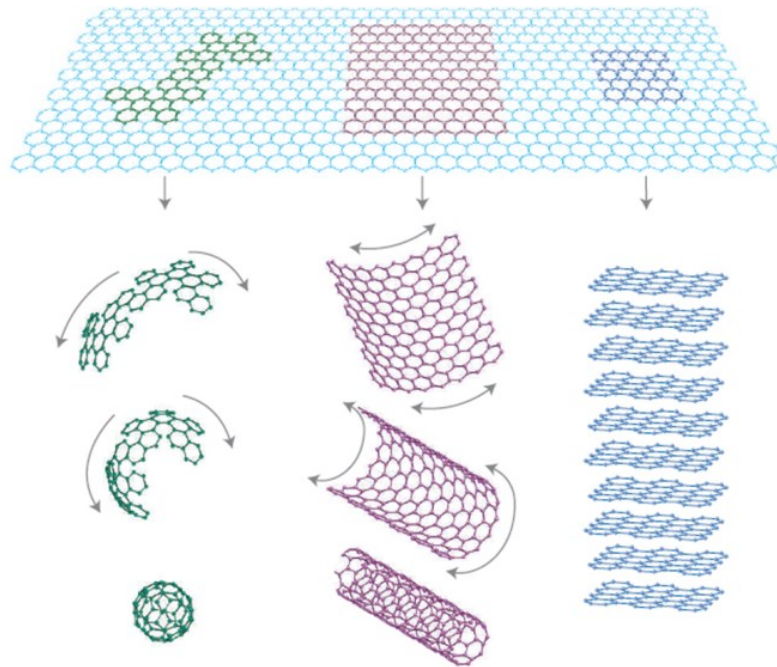


Figure 2.1 Illustration of building carbon materials of all other dimensionalities from graphene.

2.1 Monolayer Graphene

In monolayer graphene, each unit cell contains two carbon atoms, labelled A and B, with a distance a_{c-c} of 0.142 nm, as shown in Figure 2.2 (a)^{14, 40}. Two interpenetrating triangular sublattices of A and B constitute a hexagon lattice. Noticeably, the positions of A and B atoms are not equivalent, but the unit cell is invariant with a 120° rotation around any atom. Corresponding reciprocal lattice is shown in Figure 2.2 (b), in which the shaded hexagon area indicates the first Brillouin zone. This atomic honeycomb structure can be imaged by advanced microscopy techniques, transmission electron microscope (TEM) and scanning tunneling microscope (STM) for instances (Figure 2.2 (c))⁴¹⁻⁴⁶.

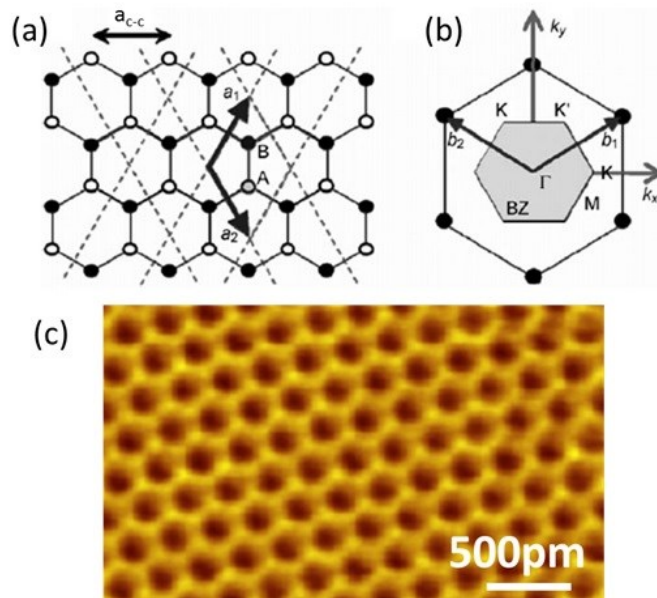


Figure 2.2 Schematic drawings of graphene cells in real space (a) and in phase (reciprocal) space (b). (c) High resolution STM image of graphene on graphite substrate.

Unique 2D honeycomb geometry leads to the sp^2 hybridization between s orbital and two in-plan p orbitals on each carbon atom forms the strong σ -bond between carbon atoms (Figure 2.3

(a-b))⁴⁷. And the remaining out-plane p orbital hybridized to form π (valence) and π^* (conduction) bands (Figure 2.3 (c))⁴⁸. The most remarkable feature of as-formed band structure is that valence and conduction bands meet at the K and K' points, so-called Dirac or neutrality points, in the Brillouin zone forming conical valleys. Due to this gapless band structure, the intrinsic graphene is usually called a semimetal or zero gap semiconductor. In zoom-in view of Figure 2.3 (c), a linear energy-momentum dispersion relation is noted in the vicinity of the K and K' points and can be described by the Dirac equation,

$$E = \hbar v_F \sqrt{k_x^2 + k_y^2}, \quad (2.1)$$

where v_F is the Fermi velocity of $\sim 10^6$ m/s. It suggests carries behave as massless Dirac fermions, mimicking relativistic particles with zero mass and a 300 times reduced effective speed of light. This peculiar band structure can be credited for most electronic and photonic properties, but which will be degenerate to a more common one when more than three layers of graphene are stacked^{14, 48}.

It's worth noting that despite graphene possess hexagonal unit cell, it is not thermodynamically destined to form crystals with hexagon, or even ordered shape. But the graphene domains with hexagonal shape are particularly attractive, since they can unambiguously reveal their single crystal nature without a need for more elaborate analysis. A significant quantity of efforts has been contributed to fabricating hexagon graphene single crystals⁴⁹⁻⁵⁴, including this dissertation (Chapter 3). One more thing we need to know about intrinsic monolayer graphene is that its distinctive band structure is not always favorable for applications, in circumstances where band gap is requisite. This is where bilayer graphene (BLG) could play the lead⁵⁵⁻⁵⁷.

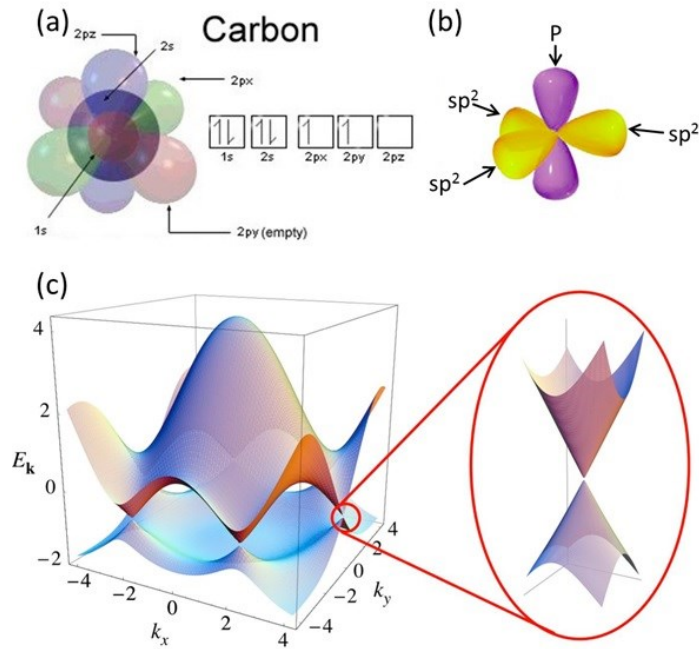


Figure 2.3 3D representation of orbital diagram of carbon atom (a), sp² hybridization (b), and electronic band structure of graphene (c). The region near the Fermi level in one K point has been enlarged in the right panel.

2.2 Bernal Stacked Bilayer Graphene

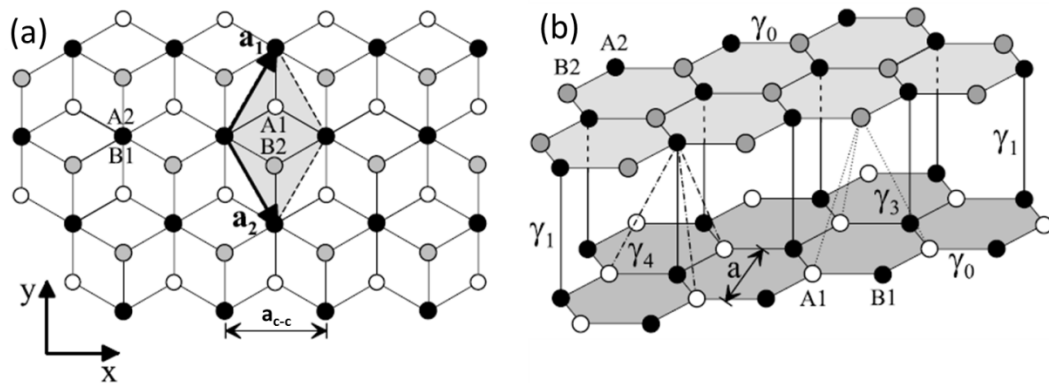


Figure 2.4 Schematic drawings of Bernal stacked graphene cells in real space: (a) top view, (b) side view with certain angle. The shaded rhombus in (a) indicates the conventional unit cell.

Bernal stacking, also known as AB stacking, is the most common arrangement in graphite, in which the vacant centers of the hexagons on one layer have carbon atoms on hexagonal corner

sites on the two adjacent graphene layers, as illustrated in Figure 2.4 (a)^{40, 58}. The unit cell consists of four carbon atoms A1, A2, B1, and B2 on the two layer planes, with in-plane and c-axis lattice constants are a of 0.246 nm and c of 0.335 nm.

Although the intrinsic AB-stacked bilayer is still gapless semimetals, as its monolayer parent, its energy-momentum dispersion relation is no longer linear, but quadratic. A controllable gap can be opened with doping or applying an external electric field on BLG (Figure 2.5)⁵⁵, a fact that makes it promising in electronic and photonic applications, as mentioned above.

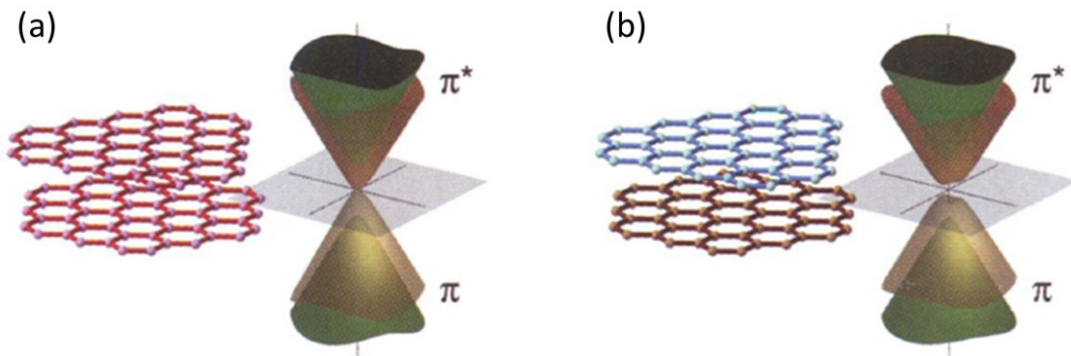


Figure 2.5 3D representation of intrinsic AB-stacked BLG without band gap (a), and opening of band gap by changing the doping level through potassium adsorption (b).

2.3 Twisted Bilayer Graphene- Graphene Superlattices

Bernal stacked graphene is the most common case in graphene samples prepared by exfoliation from bulk graphite, however bilayer graphene stacked with certain rotation angles, referred as twisted bilayer graphene (tBLG), have been widely observed in the samples synthesized by silicon sublimation of SiC, and chemical vapor deposition methods. The most distinct structural feature of tBLGs is the formation of superlattice due to the misalignment between two layers, which can be evidenced as Moiré patterns in STM or TEM images (Figure

2.6)^{43, 59}. Unlike its monolayer parent and AB-stacked counterpart, which have strictly periodic structures, tBLG has a less symmetric lattice, of which period varies with the relative rotation angle. As presented in Figure 2.6, the superlattice expands as the rotation angle decreases. At a rotation angle of $\sim 2.1^\circ$, the unit cell of superlattice is composed of 2884 atoms with a lattice constant as large as 6.6 nm (remember the lattice constant of monolayer and AB-stacked bilayer is 0.246 nm).

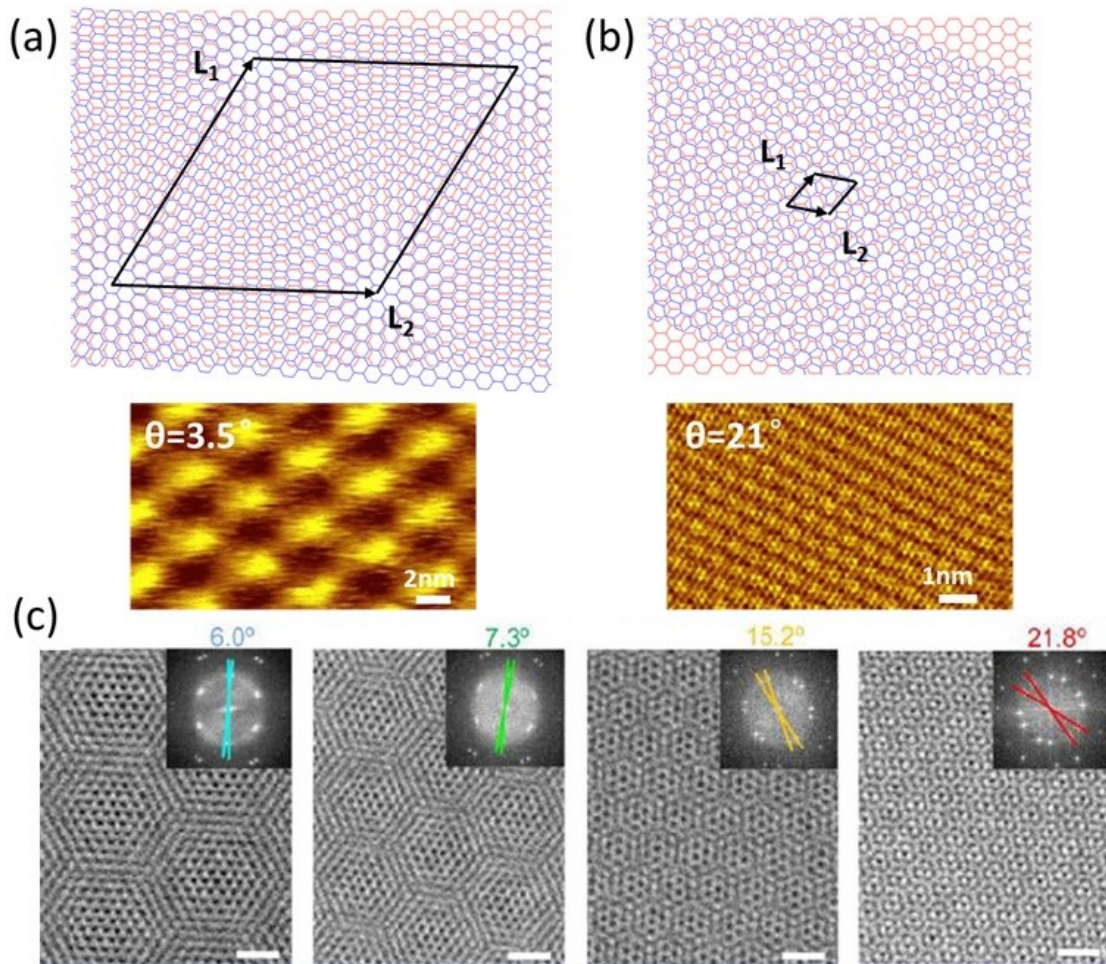


Figure 2.6 Schematic drawings and corresponding STM images of tBLG superlattice with rotation angle of 3.5° (a) and 21° (b). (c) TEM images and diffraction patterns of tBLG with rotation angle of 6.0° , 7.3° , 15.2° , 21.8° (from left to right).

The gigantic and complicated structure makes it difficult to simulate the energy band diagram for tBLG. Although numerous calculation works based on ab initio approximation or continuum mode have been reported, the results seem hypothetical and controvertible. But it is unchallengeable that the band structure of tBLG critically depends upon the twisted angle, as revealed by the angle dependent van Hove singularities (VHS) and reduction of Fermi velocity observed by scanning tunneling microscopy and Landau-level spectroscopy^{43, 60}.

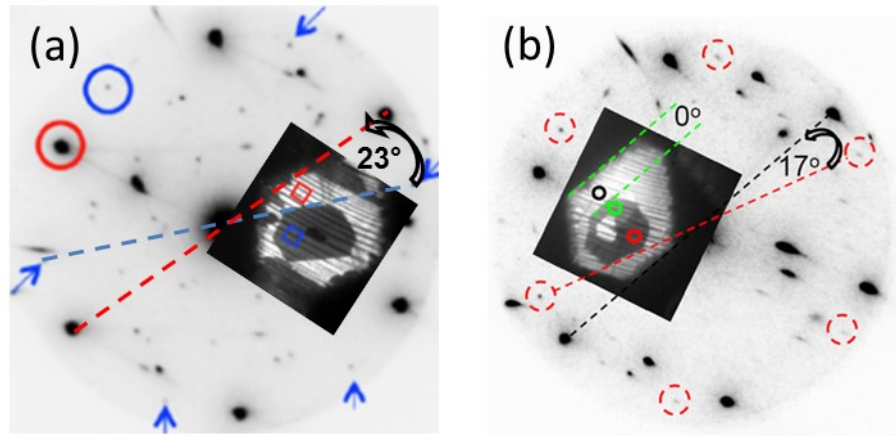


Figure 2.7 Low energy electron microscope images and corresponding diffraction patterns of a hexagon tBLG crystal with rotation angle of 23° (a) and a twinning structure of AB-stacked (0°) and tBLG with rotation angle of 17° (b).

Apart from those sophisticated measurements, Raman spectroscopy has exposed unexpected potentials in imaging the rotation angle and probing the electronic band structure of tBLGs⁶¹⁻⁶⁵, which will be elaborated in Chapter 5. More interesting is that the rotation angle can be simply estimated by the edge misalignment, for tBLG samples with both constituent layers as hexagonal single crystals (Figure 2.7)⁶⁶. Relying on this rule of thumb, the rotation angles of tBLGs investigated in this dissertation are determined with secondary electron microscope or even optical microscope, instead of high-end STM or TEM.

Chapter 3 Synthesis of Hexagon Graphene Crystals by Designed Chemical Vapor

Deposition Process

Since researchers, Novoselov and Geim, from University of Manchester successfully isolated graphene flakes from bulk graphite using Scotch tape in 2004⁷, enormous efforts have been contributed to developing methods for graphene synthesis (Figure 3.1)^{14, 20, 22, 67-70}. After ten-year intense studies, many breakthroughs have been witnessed in this field (Figure 3.2)⁷⁰: subcentimeter graphene single crystallites have been reported by multiple research groups⁷¹⁻⁷⁷; over 30 inch sized graphene films can be produced by industry based roll-to-roll techniques⁷⁸; high-quality graphene and related materials have been commercialized and even can be purchased online⁷⁹.

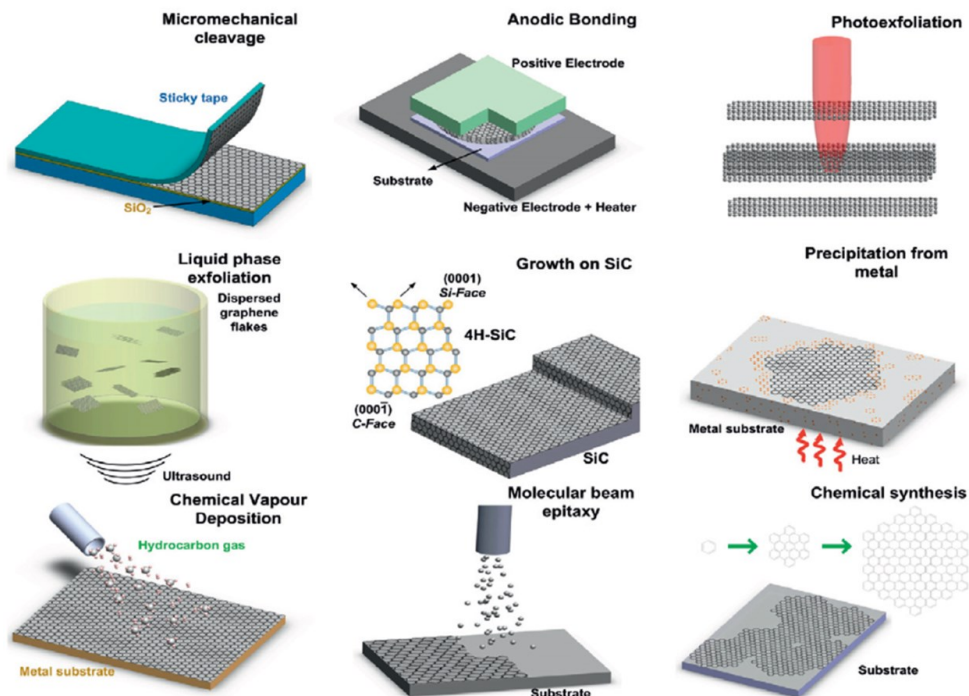


Figure 3.1 Schematic illustration of the main graphene production techniques developed in the past ten years.

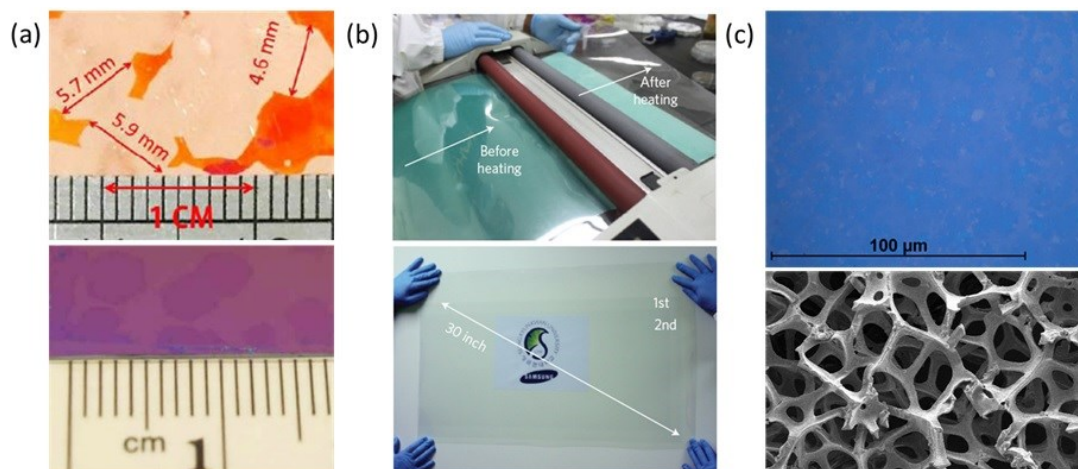


Figure 3.2 (a) Subcentimeter single-crystal graphene grains on oxidized copper (up) and on a SiO₂/Si wafer (down). (b) Roll-to-roll transfer of 30 in. graphene films. (c) Multilayer graphene film (up) and 3D graphene form (down) supplied by Graphene Supermarket.

This chapter starts with a brief review of the progress in graphene synthesis. Several well-developed methods, including mechanical exfoliation, liquid phase exfoliation (LPE), thermal decomposition of SiC, and chemical vapor deposition (CVD) on metals, are introduced. A comparison is drawn among these methods to elucidate why CVD method is employed in this study. And then, mechanisms and experimental details of CVD synthesis of graphene are described. In aim to create hexagon-shaped graphene single crystals, some key parameters, such as the type of substrate, the pretreatment of substrate, and the ratio between hydrocarbon source and carrier gas, are evaluated and designed protocols are proposed.

3.1 Synthesis Methods of Graphene

3.1.1 Mechanical Exfoliation

Graphene was first exfoliated mechanically from highly oriented pyrolytic graphite (HOPG), by repeatedly sticking and peeling with an adhesive tape (Scotch tape)^{7, 80, 81}. Figure 3.3

shows a typical optical microscopy image of as-prepared graphene flake transferred on a silicon wafer covered with 300 nm oxidized layer, which is critical to visualize graphene by forming Fabry-Perrot cavity^{80, 81}. The number of graphene layers can be roughly estimated according to the optical contrast.

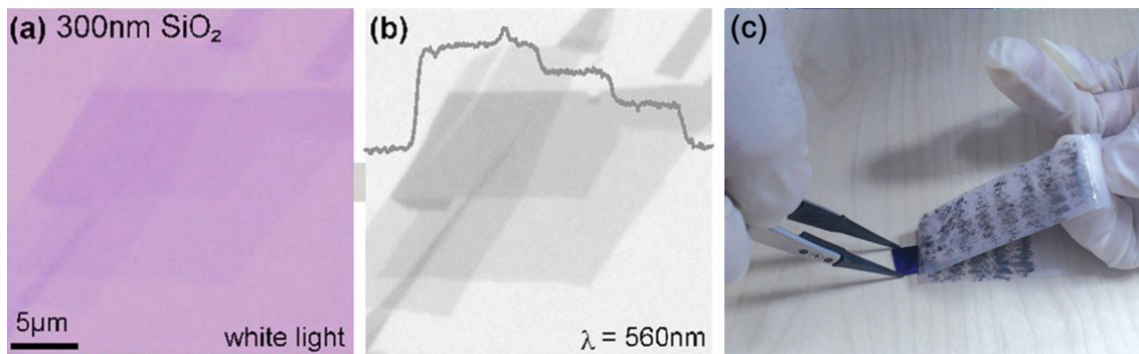


Figure 3.3 (a) Graphene on 300 nm SiO₂ imaged with white light. (b) Same sample imaged with monochromatic light, the trace displays steplike changes in the contrast for 1, 2, and 3 layers. (c) Transfer of peeled graphene flakes from tape to SiO₂/Si substrate.

This simple and low-budget technique surprisingly can offer graphene samples with so far the best crystalline structure and electronic quality, and has been extensively credited for exploring the basic properties of graphene in initial studies. Unfortunately, low yield is one of the drawbacks of this approach that cannot be overlooked. Those graphene flakes, peeled by a tape and pressed onto a substrate, are usually limited in micrometer scale with irregular shape, as shown above. Plus, they are extremely rare and hidden in a “haystack” of thousands of thick graphite flakes⁶⁹. Although isolating graphene from graphite is not challenging, searching and identification is really a time-consuming work. Apparently, mechanical exfoliation approach is not favorable for large-scale application.

3.1.2 Liquid Phase Exfoliation

Different from mechanical exfoliation, exfoliation of graphite in liquid phase has exhibited great capability of producing large quantities of graphene flakes. This process typically involves dispersion of graphite in a solvent which favors reducing the van der Waals attractions between adjacent graphene layers (Figure 3.4 (a))⁸²⁻⁸⁵. With the aid of sonication and surfactant, graphite can split into individual platelets, and further into few-layer and monolayer graphene flakes. After purification and centrifugation, the precipitate containing thousands of flakes can be gathered and deposited onto arbitrary substrate forming a dense graphene film.

The key of LPE is to find a solvent which has an appropriate surface tension to minimize the interfacial tension and easy to be balanced. In an alternative method, oxidized graphite pellets serve as the starting materials, which can be easier ultrasonically exfoliated in an aqueous solution (Figure 3.4 (b))⁸⁶⁻⁹⁰. An additional reduction step is performed in situ during the deposition of thin film.

These liquid phase approaches are extremely versatile and compatible with most biochemical processes to create functionalized graphene-based materials (Figure 3.4 (c))^{85, 91}. However, as-prepared graphene films always consist of overlapping flakes. Technically, large scale of single-layer graphene sheets via liquid phase exfoliation is still unachievable⁸⁵. Besides, intensive sonication and harsh chemicals applied during the exfoliation not only delaminate graphite pellets, but also break their highly ordered crystal structures, resulting in poor electronic properties⁶⁹.

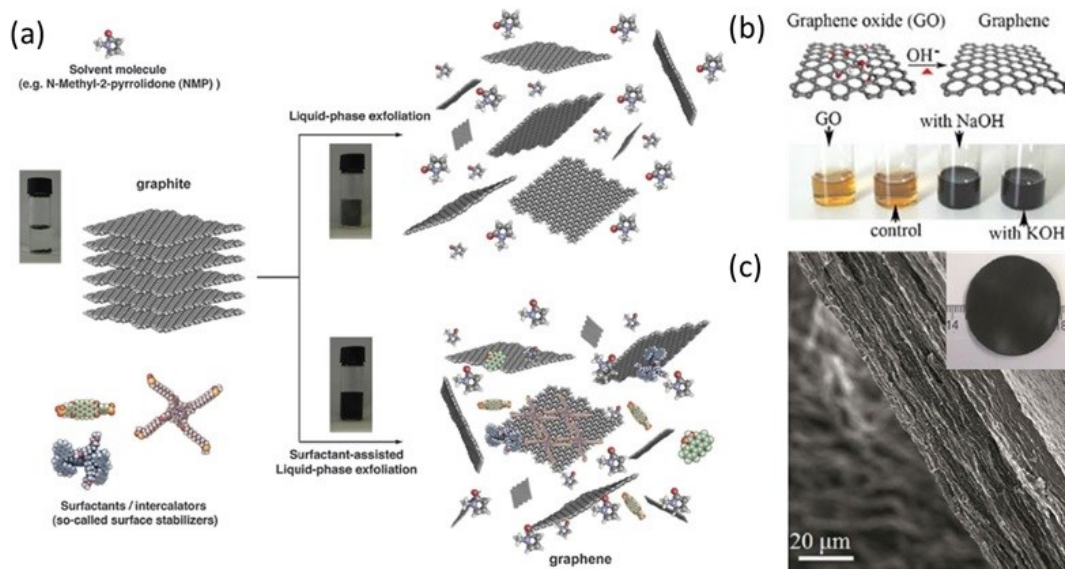


Figure 3.4 (a) Illustration of LPE process. (b) Illustration of chemical reduction of graphite oxide. (c) Biodegradable nanocomposites of amyloid fibrils and graphene.

3.1.3 Thermal Decomposition of SiC

Like most nanomaterials, there are two distinct strategies can be undertaken to synthesize graphene, the top-down and the bottom-up. The aforementioned exfoliation methods clearly belong to the former. And the latter establishes 2D carbon networks with suitably designed molecular building blocks via chemical reactions, hence, is expected to provide more precise, molecule-to-molecule, control in thickness, uniformity, and even crystal structures.

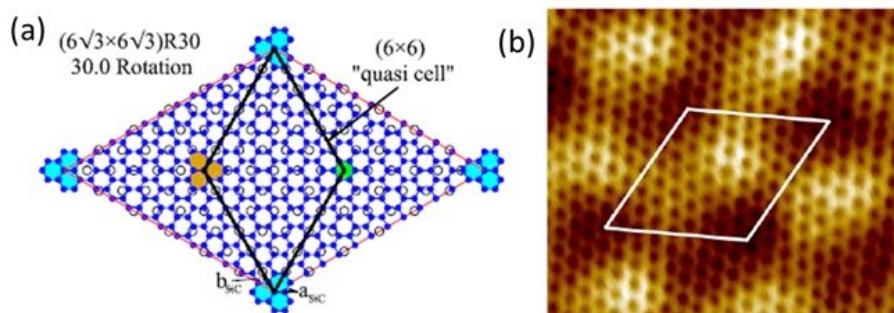


Figure 3.5 (a) Schematic drawing of graphene-SiC $(6\sqrt{3}\times 6\sqrt{3})R30$ unit cells. (b) STM images of hexagonal graphene lattice grown on Si-face with a (6×6) unit cell.

Thanks to the nature of hexagonal crystal, SiC has been considered as an ideal template for epitaxial growth of graphene and the studies about graphitization of SiC can be traced back to early 1960s^{92, 93}. Under high annealing temperature, the top layers of SiC crystals undergo thermal decomposition, Si atoms desorb and the carbon atoms remaining on the surface rearrange and re-bond to form thin epitaxial graphene layers⁶⁹. Although the thermal decomposition process can take place on either silicon or carbon faces, the subsequent morphology and electronic properties of epitaxial graphene depends highly on which of the two polar faces they are grown (Figure 3.5)⁹⁴. This strong graphene-substrate relation provides a pathway towards uniform coverage and structural coherence at wafer-scale⁹⁵. In addition, graphene grown on semi-insulating SiC can be used in situ without transfer to another insulating substrate for some electronic applications.

The two major disadvantages of this method are the rigorous growth condition, requiring high temperature and ultrahigh vacuum, and the expense of SiC wafers. Also it is not compatible with silicon based technology, and the transfer of graphene from SiC onto other substrate has rarely been reported⁹⁶.

3.1.4 Chemical Vapor Deposition on Metals

Compared with thermal decomposition of SiC, CVD is a more affordable bottom-up approach, which has been proved capable to create high-quality, large-size, and transferrable graphene for not only laboratory research, but also industrial manufacture (Figure 3.6 (a))^{70-77, 97, 98}. The first evidence of CVD grown “single layer graphite” on metals was found on Pt⁹⁹. A lot of work has been devoted to the study of the formation of single or few layer graphene on a variety of catalytic metals, such as Ru^{11, 100}, Ir^{101, 102}, Co¹⁰³, Ni^{12, 13, 103}, and Cu^{103, 104}. Depending on the

solubility of C in these metals, the growth can be a surface absorption process or segregation of active C-containing gases. The proposed mechanisms will be further discussed in this chapter.

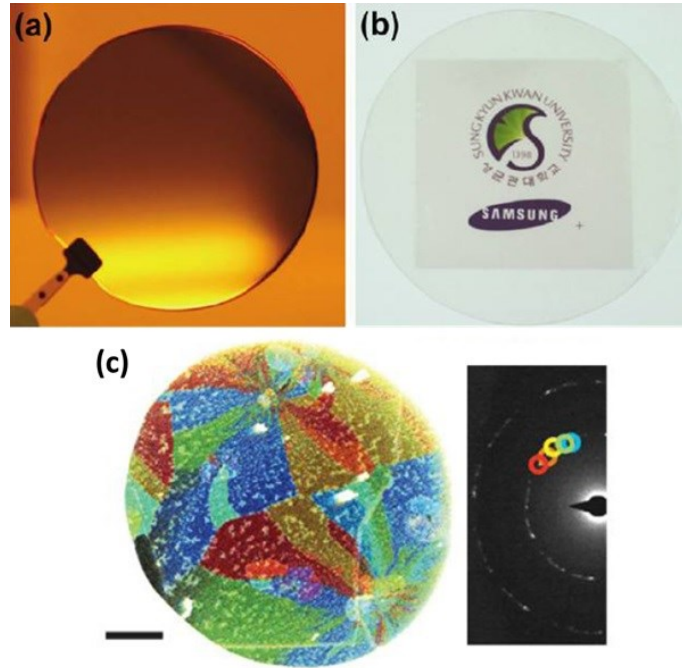


Figure 3.6 (a) CVD grown graphene film on 3 in. 300 nm thick Ni on a SiO₂/Si substrate. (b) A transferred wafer-scale graphene film on a PET substrate. (c) Dark-field TEM image and corresponding diffraction pattern of CVD grown graphene film, scale bar 500nm.

Although graphene can grow epitaxially on most metals, polycrystalline nature of metal substrates yields polycrystalline structure of graphene, while in 2D form^{69, 98, 105-107}. Within the same layer of graphene, there are single crystal domains of graphene rotated relative to neighboring domains and stitched together with defective domain boundaries (Figure 3.5 (b))^{108, 109}. These grain boundaries in graphene films grown by CVD method are responsible for a relatively lower electron mobility than their counterparts obtained via mechanical exfoliation or epitaxial growth on SiC^{69, 98}. As mentioned at the beginning of this chapter, huge progresses have been recently achieved in synthesizing large graphene single crystals and eliminating the grain

boundary effects, by engineering the CVD process. Following the lead of these studies, several key factors will be evaluated and feasible protocols based on our own CVD system will be developed in subsequent sections.

3.1.5 Comparison of Different Synthesis Methods

The following chart cited from Novoselov’s famous review “A roadmap for graphene” gives a vivid and straightforward impression of sample quality and cost of different synthesis methods (Figure 3.7)⁶⁹. And a more quantitative summary in samples quality and controllability is provided in Table 3.1.

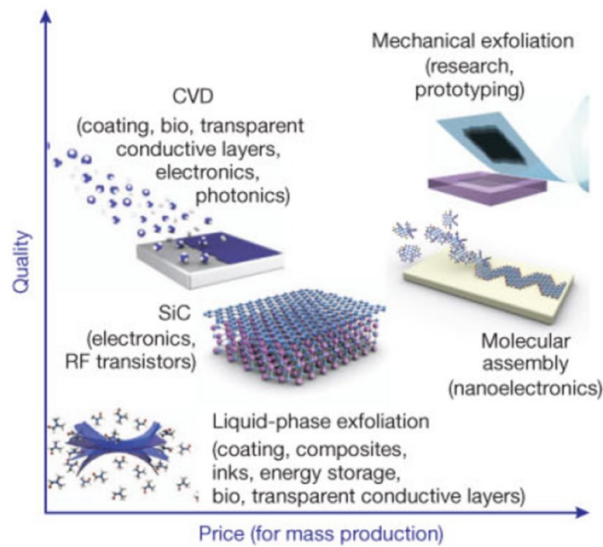


Figure 3.7 Different synthesis methods allow a wide choice in terms of size, quality, and price for any particular application.

One of the objectives of this study is to synthesis large size graphene single crystals with hexagonal shape, which can act as perfect building materials for future electronic and photonic applications. The superiority of CVD process, in the aspects of controlling the thickness, crystallite size, and even crystalline orientation, is obvious.

Table 3.1 Properties of graphene obtained from different methods.

Method	Crystallite size	Crystallite orientation	Control of thickness	Sample size	Charge carrier mobility (at ambient temperature) ($\text{cm}^2\text{V}^{-1}\text{S}^{-1}$)
Mechanical exfoliation	> 10 mm	Random	Little control (1 layer ~ bulk)	> 1mm	10^5
Liquid phase exfoliation	Heterogeneous (1~ 100 μm)	Random	Moderate (1~ few layers)	Infinite as a layer of overlapping flakes	10
SiC	~ 100 μm	Epitaxial	Precise	Limited to substrate size	10^4
CVD	> 5 mm	Random (Could be controllable)	Precise	> 10^3 mm	10^4

3.2 Chemical Vapor Deposition of Graphene

3.2.1 Overview of Chemical Vapor Deposition

Chemical vapor deposition is popularly used to produce high-purity, high-performance solid materials, especially to produce thin films in semiconductor industry. In a typical CVD process, the substrate is exposed to one or more volatile precursors, which react and/or decompose on the substrate surface to produce the desired deposit. Frequently, volatile by-products are also produced, which can be removed by gas flow through the reaction chamber. For evaluation and engineering, a thin film deposition can be generally divided into following stages: incubation, nucleation, growth of individual crystallites, faceting and coalescence of individual crystallites, and formation and growth of continuous film.

3.2.2 Chemical Vapor Deposition System

Depending upon the specific usages, a variety of CVD systems have been invented. Classified by operating pressure, there are atmospheric pressure CVD (APCVD), low-pressure

CVD (LPCVD), and ultrahigh vacuum CVD (UHVCVD) systems. Reduced pressures tend to suppress unwanted gas-phase reactions and improve film uniformity, but complex the affiliated vacuum systems. And beyond gas phase precursors, non-volatile precursors can be introduced in form of a liquid/gas aerosol in aerosol assisted CVD (AACVD), or can be directly injected in liquid phase (DLICVD). Microwave plasma (MPCVD) can be also utilized to enhance chemical reaction rate of the precursors, consequently lowering the reaction temperature^{110, 111}.

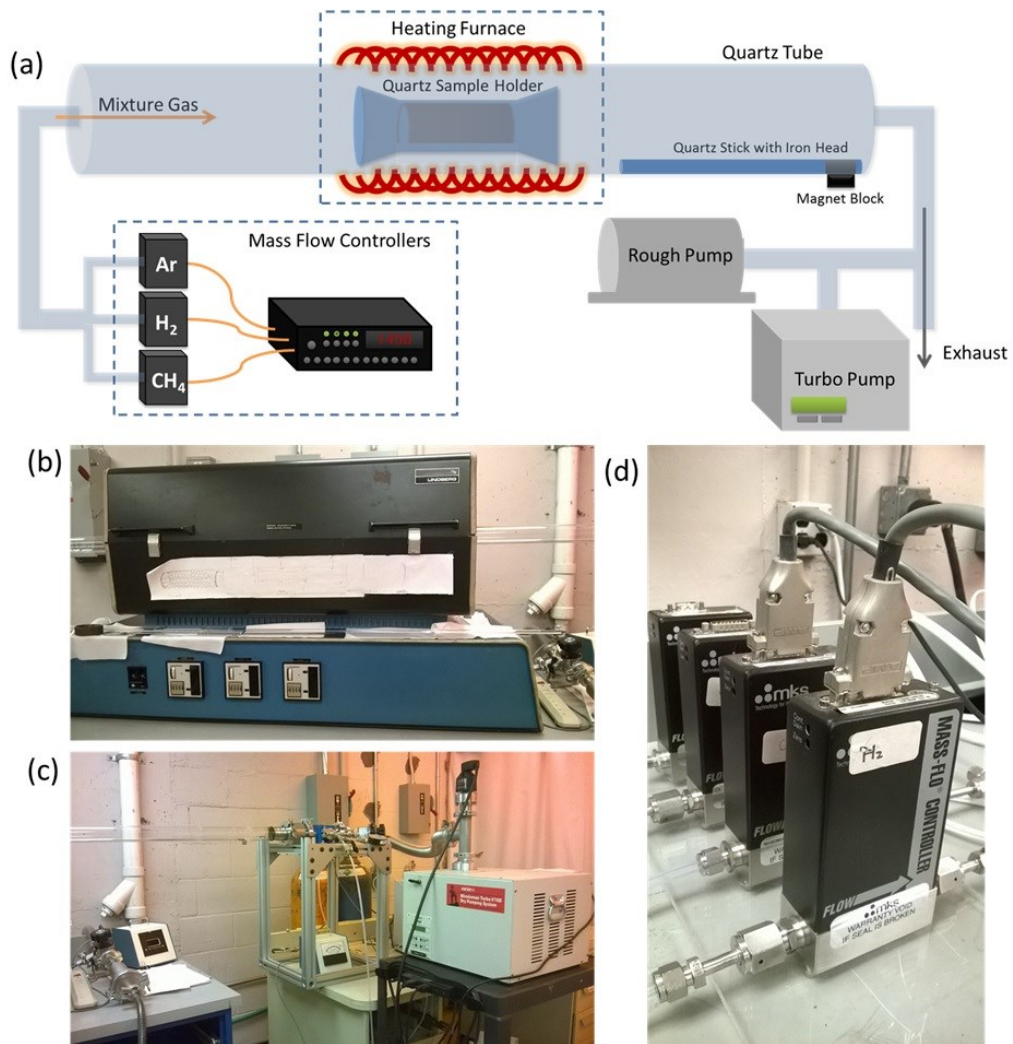


Figure 3.8 (a) Schematic of the CVD system applied for graphene growth in this study. (b-d) Photos of main components, heating furnace, mechanical pump and turbo pump, mass flow controller, respectively.

In this study, a classical APCVD system is applied for CVD growth (Figure 3.8), of which consists a 2-inch diameter, 2-meter long quartz tube as the reaction chamber and a heating furnace (Lindberg Furnace) with ~30 cm uniform temperature zone, as shown in Figure 3.8 (b). A basic set of rough pump and turbo pump is mounted to (Varian, Minuteman Turbo-V70D) the quartz tube and a base pressure of $\sim 10^{-5}$ Torr can be achieved (Figure 3.8 (c)). Mass flow controllers equipped with a 4-channel readout (MKS) can realize precisely regulating the flow rate of each precursor and carrier gas species to engineer the deposition process (Figure 3.8 (d)).

3.2.3 Experiment Details of Chemical Vapor Deposition of Graphene

Based on above system, the graphene growth procedure can be described as follows. Metal substrates, sitting inside a quartz sample holder, are loaded into the quartz tube and placed in the uniform-temperature zone of the furnace. The quartz tube is evacuated thoroughly and then quickly filled back to ambient pressure with massive Ar gas flow. Subsequently, the tube furnace is slowly heated up to 1030 °C and metal substrates are annealed under pure Ar or slight reduction environment, during this heating and stabilizing process. Afterwards, the precursor gases, CH₄ and H₂, are mixed with designed ratio and introduced into the tube by carrier gas Ar to initialize the growth. The growth period varies from 2 h to 12 h, depending on the growth conditions. Growth is terminated by cutting off CH₄ supply. Samples are fast-cooled down to room temperature, typical within half of an hour, by pushing the sample holder out of the heating zone utilizing magnetic force, but still under the protection of Ar and H₂ flow.

CVD is a complex kinematic process, with multiple phases and dozens of manipulatable parameters. To design and optimize this process, some key factors, such as the type of substrates,

the annealing condition, the CH₄/H₂/Ar ratio, will be discussed and deeply investigated in this study.

3.3 Key Factors in Chemical Vapor Deposition of Graphene

3.3.1 Type of Metal Substrates and Growth Kinetics

Table 3.2 Properties of graphene obtained from CVD on different metals.

Transition metals	Growth mechanism	Carbon solubility at ~1000° C	Active crystal facet	Crystal size	Crystallite orientation	Control of thickness
Pt	Still in debate	$\sim 3.1 \times 10^{-4}$ – 0.0043 at. %	Pt(111) (the best performance), Pt(110), Pt(100), Pt(311)	mm	Polycrystalline with various orientation	Moderate (Difficult for few layer)
Ru	Bulk-mediated growth, carpet growth mode	0.34 at. %	Ru(0001)	Limited to substrate crystal size	Monocrystalline domain with perfect rotation alignment	Precise
Ir	Bulk-mediated growth, carpet growth mode	0.041 at. %	Ir(111)	Limited to substrate crystal size	Polycrystalline with various orientation	Moderate (Monolayer with bilayer islands)
Co	Bulk-mediated growth	~0.9 at. %	All facets are active, Co(0001) with the best performance	μm	Polycrystalline with various orientation	Moderate (Feasible on epitaxial Co(0001) on sapphire)
Ni	Bulk-mediated growth	~0.6-0.9 at. %	All facets are active, Ni(111) with the best performance	μm	Polycrystalline with various orientation	Little control (non-uniform)
Cu	Surface-mediated growth	$\sim 7.4 \times 10^{-4}$ – 0.008 at. %	All facets are active, Cu(100) and Cu(111) with the best performance	> 5 mm	Polycrystalline with favorable orientation on Cu(111)	Precise

As mentioned in Section 3.1, CVD growth of graphene has been fulfilled on various transition metal substrates, but with huge distinction in crystal size, crystallite orientation, and thickness (Table 3.2)^{11, 99-105, 112}. For example, monolayer graphene with perfect aligned monocrystalline can be easily obtained on a Ru(0001) crystal surface, and uniform monolayer can be also grown on a polycrystalline Cu surface, but it is difficult to achieve large area of monolayer graphene with absence of small thicker islands on Ni surface, regardless of whether single-crystal or polycrystalline Ni is used^{105, 112}.

And it should be emphasized that the CVD synthesis of graphene is a heterogeneous, catalytic, chemical reaction, so the metal performs the two different roles of substrate and catalyst here. In a typical catalytic process, the catalytic activity of metal substrate should be gradually reduced as the film expands and eventually the reaction should be terminated when a continuous film formed. This “self-limiting” effect is expected to give preferentiality to monolayer graphene formation, but has only been observed in Cu to date (and also depends on the process conditions)¹¹².

In order to visualize the kinetic behavior of graphene growth, a carbon isotope-labeling technique in conjunction with Raman spectroscopic mapping has been performed on Ni and Cu. ¹²CH₄ and ¹³CH₄, as precursor gases, were supplied sequentially during the deposition^{13, 113}. In the Raman mapping, no distinguishable separation of isotopes was found on Ni films, even after several sets of feeding time sequences of C isotopes. Contrarily, the spatial distribution of ¹²C and ¹³C following the precursor time sequence could be clearly imaged in the mapping of graphene samples on Cu (Figure 3.9 (a-b)) and the growth followed a linear growth rate^{13, 112}.

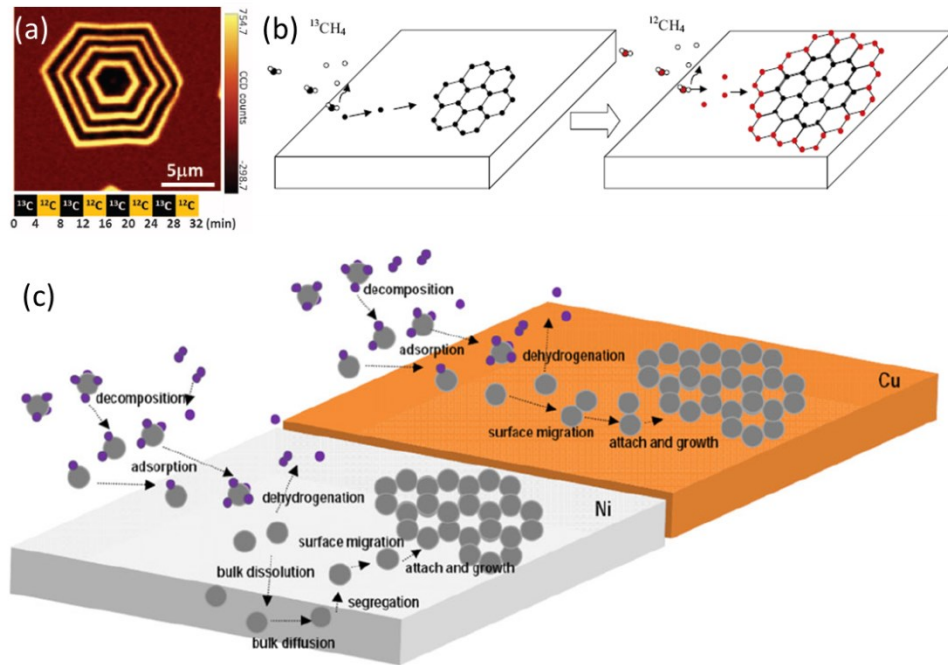


Figure 3.9 (a-b) Raman mapping and schematic of a graphene domain grown on Cu with isotopic carbon labels. (c) Growth kinetics in CVD graphene on Ni and Cu.

This distinction in the ^{12}C and ^{13}C distribution strongly suggests the different kinetic behavior of the CVD growth of graphene on Ni and Cu. Surface roughness and crystal structures of metals certainly influence the arrangement of C atoms during the deposition, while carbon solubility in the metals play a more decisive role here.

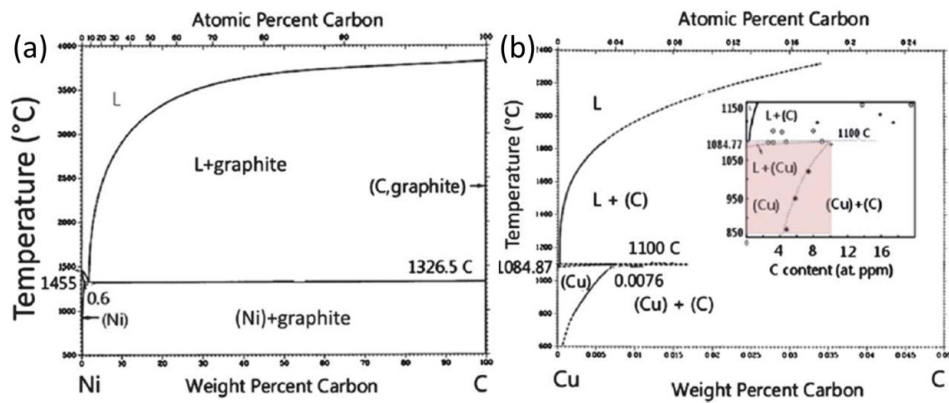


Figure 3.10 Binary phase diagrams of transition metals and carbon: (a) Ni-C, (b) Cu-C.

For illustration, there are two steps need to be highlighted: the dilution or incorporation of carbon into the metal, which is better known as dissolution, and the formation of a graphene through rapid cooling, also known as segregation. For Ni and Cu, they share similar procedure in the decomposition of precursors, absorption and dehydrogenation of active C fragments. But due to a large solubility of C in Ni (Figure 3.10 (a))¹¹⁴, active carbon adatoms can be easily diffuse into bulk Ni, revealing a bulk dissolution (bulk mediated) behavior. When the concentration of carbon adatoms in the bulk metal has achieved the threshold for nucleation or during the cooling process, during which the carbon solubility in the metal decreases, the excess carbon adatoms segregate and diffuse back to the Ni surface, and graphene formation occurs (Figure 3.9 (c))¹¹². Noticeably, this segregation process does not stop until the concentration of carbon in the bulk metal has decreased to equilibrium, even though the supply of hydrocarbon has been switched off. This explains the uniformity of the ¹²C and ¹³C distribution across the Ni surface in the isotopic labelling tests. Since the chemical reaction not only involves heterogeneous catalysis, it is difficult to control the thickness of graphene formed through segregation and even precipitation process.

Different from most transition metals, Cu has a relatively low C solubility (Figure 3.10 (b)), and also a low diffusion barrier, thereby active carbon adatoms incline to stay on the Cu surface, migrate to nucleation sites, and facilitate monolayer graphene growth (Figure 3.9 (c)). The distinguishable growth front of isotopic carbon supports this surface-mediated mechanism. It is worthy of mention that, the underlayer growth of bilayer and few layer flakes have also been discovered on graphene samples on Cu⁶⁶. To dispel doubts, these multilayer areas could origin

from thick nucleation centers or the supersaturated carbon diffusing to the substrate/film interface. And the growth of these flakes has a considerably slower rate than the overlaying layer and will be terminated once the full coverage of monolayer graphene achieves^{66, 111, 112}.

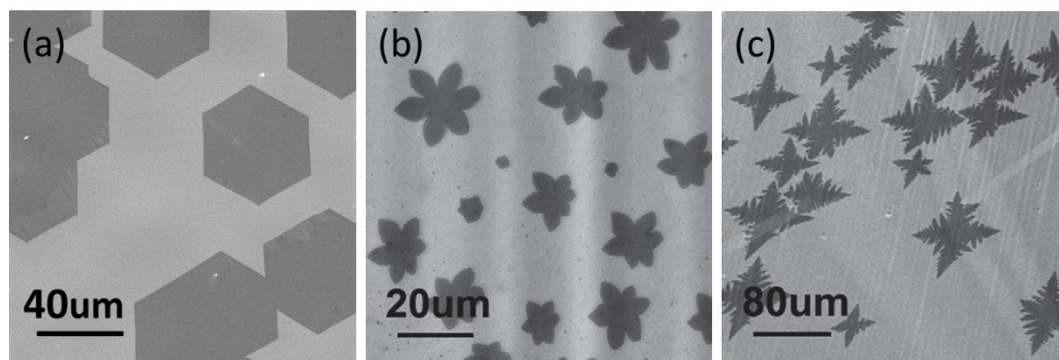


Figure 3.11 SEM images for graphene islands with (a) hexagonal shape, (b) six-lobed flower shape, and (c) dendrite shape.

Also important, the graphene islands grown on Cu tend to have an ordered shape, such as a hexagonal shape with 120° corners (Figure 3.11 (a)), a flower-like shape with four or six lobes (Figure 3.11 (b)), or a dendrite shape (Figure 3.11 (c))¹¹⁵. The hexagonal shape of graphene islands formed by the zigzag edge seems preferred in graphene grown on polycrystalline Cu at ambient pressure with a low-carbon-source ratio^{111, 112, 115, 116}. In consideration of the self-limiting growth mechanism, the preference to growing in hexagonal shape, and the ability of transfer to arbitrary substrates, Cu foils (Alfa, 25 μm in thickness, 99.8% in purity) are chosen in this study.

3.3.2 Pretreatment of Cu Foils

It has been well demonstrated that surface conditions of the catalytic Cu substrate, not only the crystal structures, but also the topographies, are crucial in determining the quality of graphene samples^{111, 112, 114, 117}. As-received Cu foils have polycrystalline structures and are covered with a

native oxidized layer and a large amount of imperfections, such as steps, folds, and impurities, are non-ignorable.

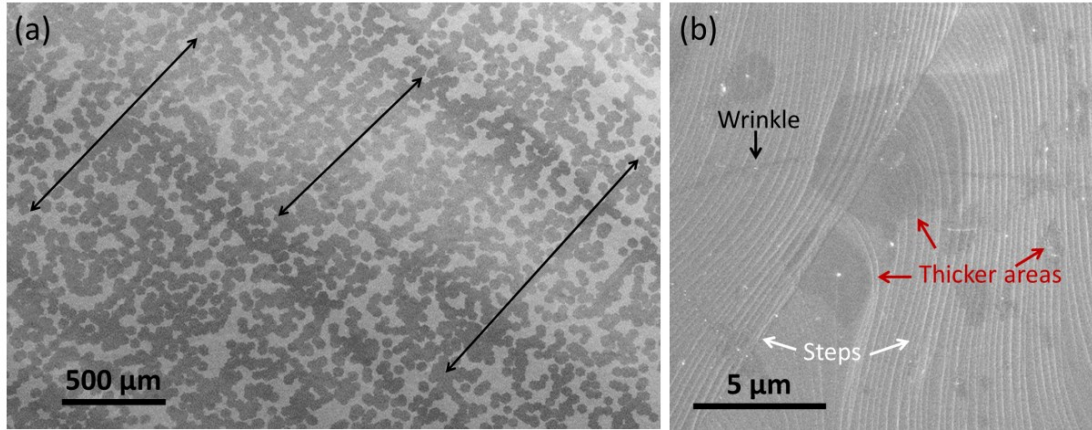


Figure 3.12 Overview (a) and close-up (b) SEM images of graphene islands grown on Cu foil using our APCVD system.

The influence of imperfections is fairly clear that active carbon adatoms prefer to nucleating at these imperfect sites, which are more energetically active compared to smooth Cu surface, at the first phase of growth^{114, 118, 119}. Because the commercial Cu foils applied in this study are produced through a rolling process, quasi-parallel-line textures can be found on the surface, resulting in a dense packing of graphene islands along these lines (black arrows in Figure 3.12 (a)). Moreover, thicker graphene blocks are always found around point defects, like Cu oxides particles, as shown in Figure 3.12 (b). To eliminate these surface imperfections is beneficial to controlling the nucleation density and suppress the multilayer formation. Other than surface defects of Cu foils, there are two widely observed features, steps and wrinkles, are also labeled out in Figure 3.12 (b). Distinguished from aforementioned textures, steps are microstructure of Cu foils, which are unexpectedly handy to visualize atomically flat graphene

films under SEM. Strictly speaking, wrinkles are defects on graphene film, which are unavoidably formed during the cooling process. The large and negative thermal expansion coefficient of graphene results in significant shrinkage of Cu upon cooling, which induces mechanical stress on graphene. This stress is released via the formation of wrinkles.

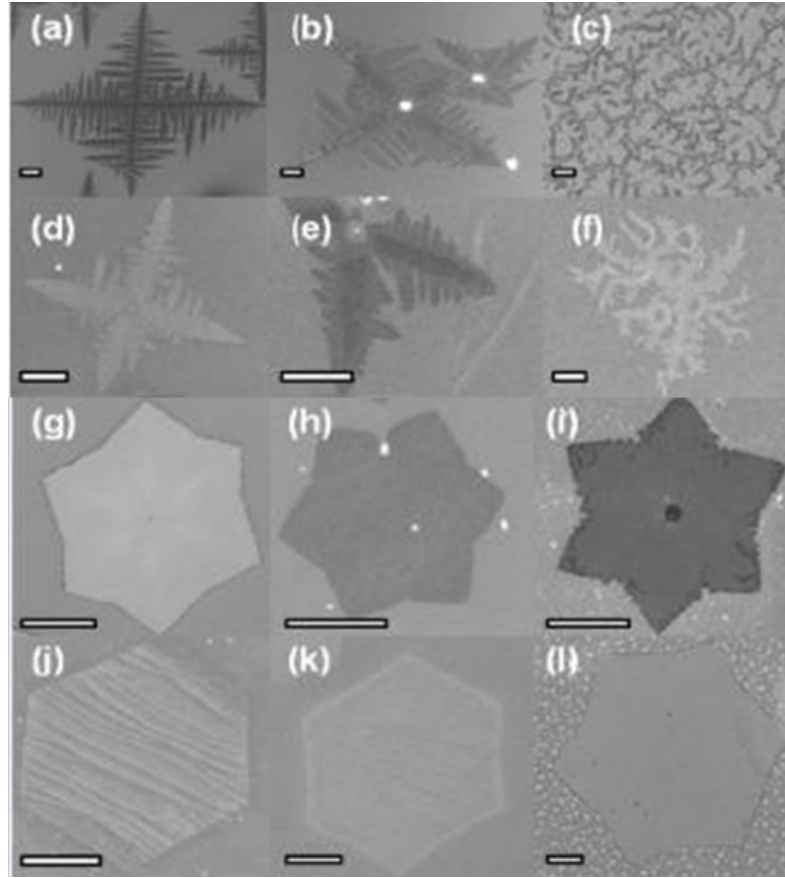


Figure 3.13 Morphology of graphene islands grown on Cu(100) (left), Cu(110) (middle), and Cu(111) (right) with different CH_4/H_2 ratio by LPCVD (a-f), and APCVD (g-l). Scale bars are $5\ \mu\text{m}$ except for 5d and 5j, which are $1\ \mu\text{m}$.

Previously mentioned, Graphene can be nucleated on nearly all facets of Cu, and the performance on single crystal films with three low indexed facets, (100), (110), and (111) has been intensely evaluated, but with quite controversial observations^{111, 112, 116, 120-122}. Some suggest

that a high binding energy of graphene on Cu(111) can ensure the graphene is in the most energetically stable state and prevent other orientations and grain defects. Others claim graphene forms equally on Cu surfaces with any crystal lattice. According to the previous studies carried in our group, graphene grains grown even within a single Cu grain could have varied orientations and individual graphene could expand over the grain boundaries of Cu with minimal structural disruption, implying a weak influence of Cu crystal lattice^{118, 122}. Some latest study indicate the interaction between graphene and Cu substrate should be specified upon the growth process: in LPCVD, the graphene island orientation and morphology are highly dependent on the underlying copper lattice; whereas, in APCVD, multiple preferred orientations coexist, while the ratio between precursor CH₄ and H₂ dominate the morphology (Figure 3.13)¹¹⁶.

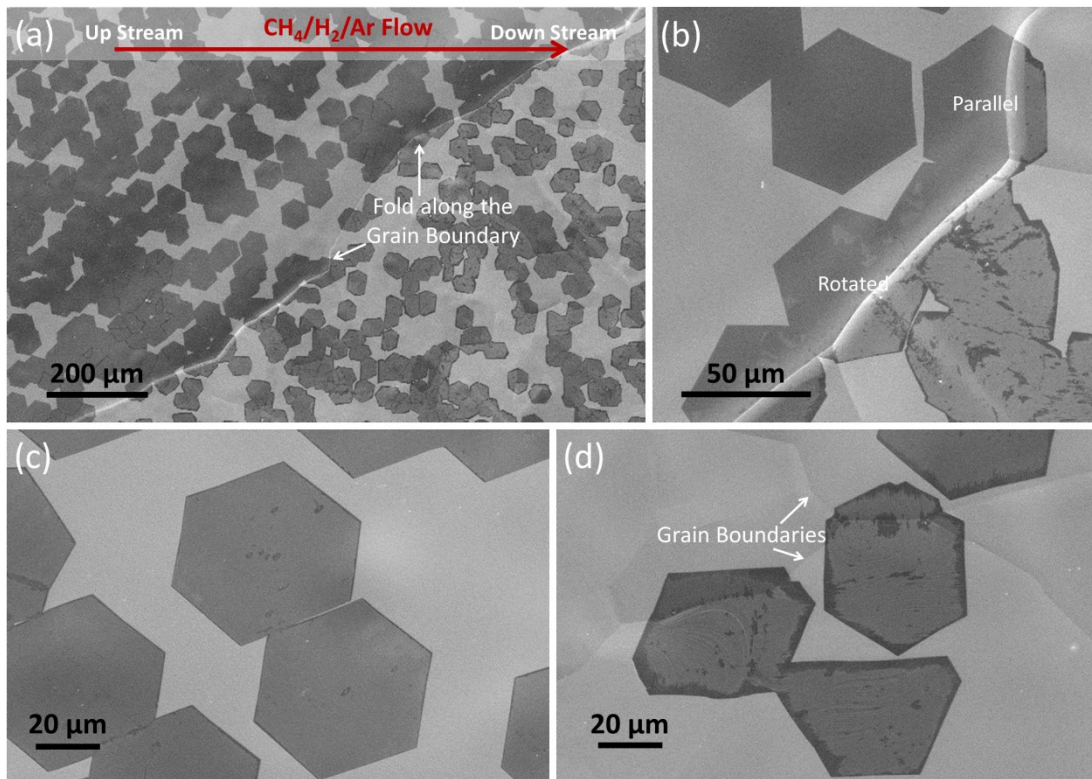


Figure 3.14 SEM images of graphene grown on a Cu foil with different surface morphology.

In spite of the controversial parts, there are still some common grounds have been reached, such as that flat Cu surface with large-size domains is in favor of growth of large graphene single crystals, which has been well demonstrated in my experiment^{52, 98, 123, 124}. Figure 3.14 presents one piece of Cu foil consisting of two regions with divergent morphologies. Resulting from the structural mismatch, a deep fold arose along the boundary between these two regions even under the force applied to pull the foil out of the quartz sample holder. An over centimeter size of flat Cu surface without noticeable contrast is found on the upper left side; while the lower right is covered with patchwork-like domains, referring to a polycrystalline nature. Correspondingly, graphene islands formed on the upper left side possess sharp edges and nearly perfect hexagonal shape (Figure 3.14 (c)); while the ones on the other side show less regularity in shape, less uniformity in thickness, and also a slightly slower growth rate (Figure 3.14 (d)). Graphene islands span over the Cu grain boundaries frequently occur here, but seemingly with equivalent chance to maintain a similar orientation or to rotate certain angle and construct a twinning structure (Figure 3.14 (b)). It is understandable that graphene preferably grows into asymmetric or undefined shape when it expands over multiple Cu domains, considering the heterogeneous diffusion ability of carbon adatoms^{114, 125}.

Pretreatment of Cu foil is requisite. High-temperature annealing prior to deposition is chosen in this work, over mechanical and electrochemical polishing, because annealing process can not only flatten the Cu surface, but also relieve internal stresses, refine the microstructures, and even recrystallize Cu into larger grains. The annealing is routinely fulfilled at a temperature just below the melting point of Cu (1085 °C), displayed as 1030 °C in our uncalibrated heating

furnace. The variant morphology in as-treated Cu foils, shown above, mainly attributes to the nonuniform temperature distribution inside the furnace. Generally, a reductive, hydrogen-rich (H_2 -rich), environment, is provided during annealing to remove the native oxidized layer and recover the catalytic capability of Cu. Alternatively, if the annealing is implemented without H_2 or with intentionally supplying O_2 (O_2 -rich), the passivated Cu surface could be constructive to reduce the nucleation density (Figure 3.15). This is the strategy taken in this study to gain over millimeter-size graphene single crystals.

The comparison experiments were executed with strictly same growth condition but different annealing condition, H_2 -rich (a) and O_2 -rich (b), respectively. As predicted, the nucleation has been suppressed dramatically; hence, more active carbon source can contribute to enlarging one single domain.

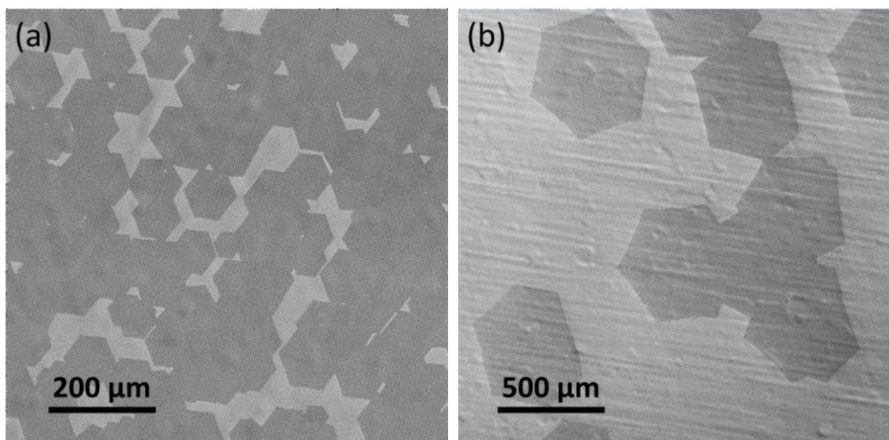


Figure 3.15 Typical SEM images of graphene samples produced with a H_2 -rich (a) and O_2 -rich (b) annealing process, respectively.

Also worth to mention, the Cu foil is preferred to wrapping into a cylindrical roll in order to suppress the evaporative loss of Cu during high temperature annealing and growth. As shown in

latest report and our study, the smooth inner surface facilitated a much lower nucleation density and much larger graphene domains.

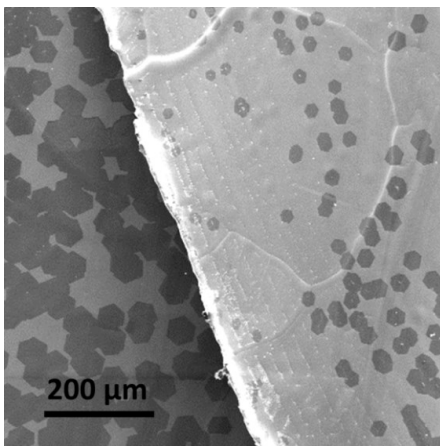


Figure 3.16 SEM images of the inner (left) and outer (right) surfaces of Cu cylindrical foil after synthesis.

3.3.3 Methane and Hydrogen Concentration

Hydrocarbon-based reactants, the most mentioned being methane (CH_4), are commonly used as C source. Hydrogen gas (H_2) is also supplied through the whole growth process, playing a reductive background; however, its impact on graphene growth has been suggested far beyond that.

In most reported CVD growth of graphene on Cu, H_2 appears to serve a complex role: an activator of the surface bound carbon that is necessary for monolayer growth and an etching reagent that controls the size and morphology of the graphene domains^{111, 112, 126}. It is known that the decomposition of CH_4 requires a very high temperature ($> 1200\text{ }^\circ\text{C}$), which is nearly unachievable in thermal CVD systems, because of the strong C-H bonds ($440\text{ kJ}\cdot\text{mol}^{-1}$). The use of catalytic transition metals, which have empty d-shell atomic structures and are ready to function as

electron acceptors, facilitates the chemisorption and dehydrogenation reactions. However, even with the aid of Cu, in this context, it is not thermodynamically favorable for CH_4 to decompose into active carbon species, that is, $(\text{CH}_3)_s$, $(\text{CH}_2)_s$, $(\text{CH})_s$, or C_s , subsequently. Feeding excessive CH_4 might counteract this thermodynamic barrier effect, but undesirable formation of thicker layer seems to be an unavoidable aftereffect.

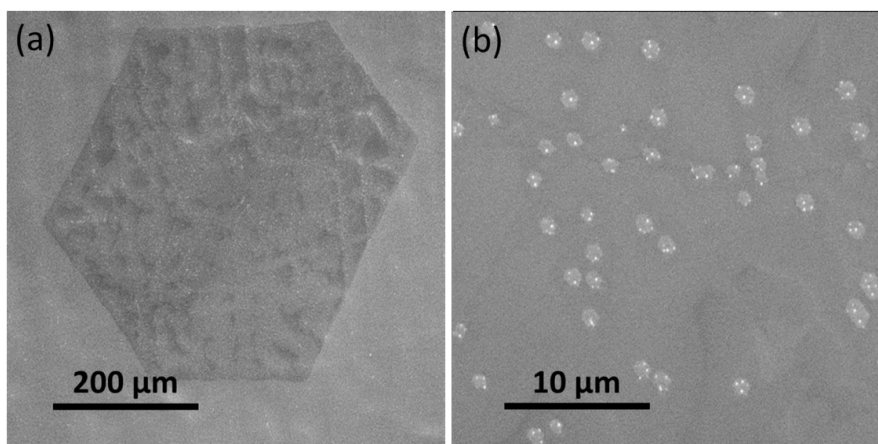


Figure 3.17 SEM images of a graphene sample suffering H_2 etching during a slow cooling process.

Experimentally, the catalytic role of hydrogen has been witnessed in activating carbon. Since Cu has a large hydrogen solubility, molecular hydrogen more readily dissociates on Cu and forms active hydrogen atoms. One hypothesis suggests that these hydrogen atoms can promote activation of physisorbed CH_4 , and lead to formation of surface active carbon species, which contribute to the graphene growth, step by step. It is noticeable also due to the high solubility, an abundant flow of H_2 is demanded to enable the active hydrogen atoms desorption from Cu surface. Therefore, a surface and/or subsurface partially covered with atomic hydrogen could be the starting point of growth.

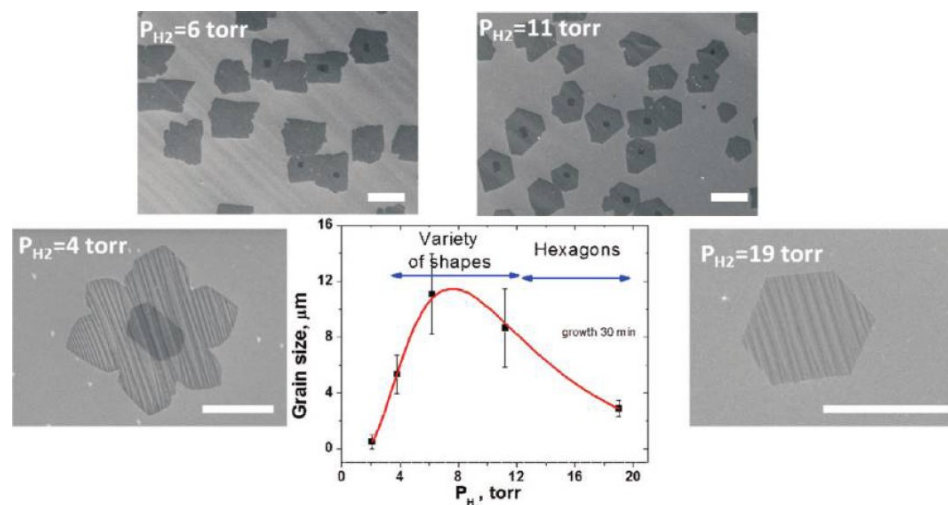


Figure 3.18 The average size of graphene grains grown for 30 min at 1000 °C on Cu foil using 30 ppm methane in Ar mixture at 1 atm, as a function of partial pressure of hydrogen. Scales bars are 10 μm (top two images) and 3 μm (bottom two images).

On the other hand, the capability of hydrogen in etching carbonaceous materials cannot be overlooked, especially under a high concentration of H_2 flow. The etching effect could be notable if a relatively slow cooling process is performed after deposition, during which CH_4 supply has been cut off, but H_2 and Ar are keeping flow. As shown in Figure 3.17, trillions of micrometer-sized holes with quasi-hexagonal shape were cut in the graphene film, which was left in the heating zone for additional 5 minutes after the growth terminated. Interestingly, these holes always appear with one or several bright spots, suspected as CuO_x particles, in the center. Similar observation has been reported and the roles of activation centers have been claimed for these particles, based on the note that no etching occurs without them. Another noteworthy point is the H_2 etching has certain selectivity and results in a hexagon with zigzag termination. Definitely, this tailoring behavior is applicable during the growth process under high H_2 condition, which is essential to this study.

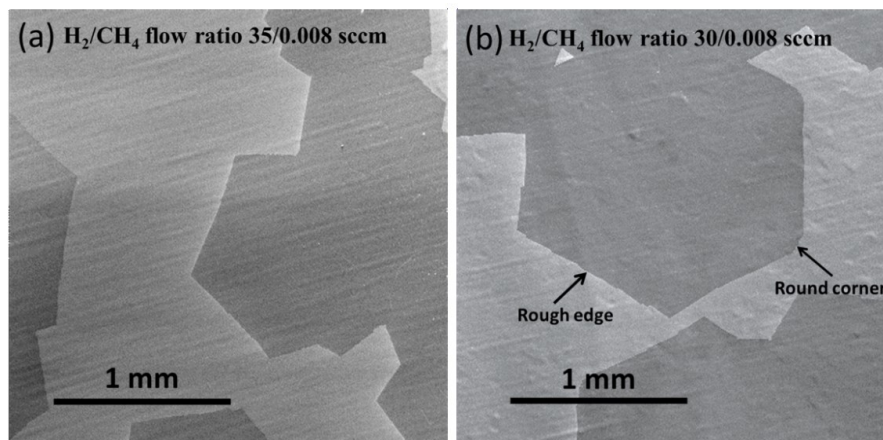


Figure 3.19 SEM images of graphene samples grown with fixed CH_4 flow rate (0.008 sccm) but varied H_2 flow rate (35 sccm (a), 30 sccm (b), respectively).

In consideration of the dual parts hydrogen plays, there is a competition between formation of active surface bound carbon species committing graphene growth and tailoring the grains shape and dimension by etching away the “weak” carbon-carbon bonds. As indicated in ref. 3-37 (Figure 3.18), no graphene growth was observed at low partial hydrogen pressures ($\text{PH}_2 < 2$ Torr, that is, $\text{PH}_2/\text{PCH}_4 < 20$); at intermediate hydrogen partial pressures ($\text{PH}_2 = 11$ Torr, that is, $\text{PH}_2/\text{PCH}_4 = 200/400$), graphene grains show a variety of shapes without any recognized preference toward either zigzag or armchair termination; and at higher hydrogen pressures ($\text{PH}_2 \approx 19$ Torr, that is, $\text{PH}_2/\text{PCH}_4 > 400$) result in distinct hexagonal shape of grains and saturation of their size due to etching of the graphene by hydrogen. Thereupon, not the concentration of precursor gas CH_4 alone, but the ratio between CH_4 and H_2 affects the graphene nucleation, the growth rate, and the termination size of grains.

Figure 3.19 exhibits large-size monolayer graphene single crystals harvested from two deposition experiments with identical CH_4 flow rate, but varied H_2 flow rate. After the same

period of growth, the one with higher CH₄ ratio (b) slightly exceeded in dimension, but sacrificed the well-sculptured appearance.

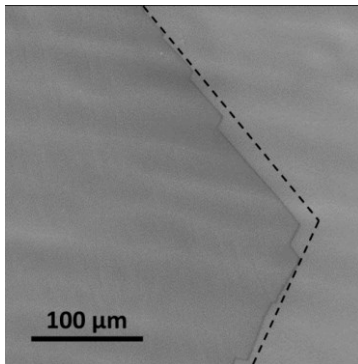


Figure 3.20 A zoomed in view of graphene sample in Figure 3.19 (a).

Even the ratio of 35/0.008 sccm (PH₂/PCH₄ ≈ 440) is barely adequate to maintain a perfect shape; unsmooth edges are noticed under a zoom-in view (Figure 3.20). Nonetheless, rough or even dendrite edges are quite common for huge graphene hexagons⁵⁴, as the trade-off of fast growth, which have been suggested harmless to their single crystal quality^{127, 128}.

3.3.4 Duration of Growth

The last factor is the duration of growth. Longer growth duration is beneficial to enlarging the size of graphene islands, but only to certain extent. It is well-known that the growth rate declines as growth time prolongs¹¹⁸. And in this H₂-assistant process, the competition between growth and etching presumably leads to a limitation of grain size. More important, some studies show that if the growth duration is longer, the six corners of the hexagonal graphene islands will protrude to become star-like shape or even six-petalled flower-like shapes, following the active species concentration gradient¹²⁷⁻¹²⁹. Taking these into consideration, a modest time, not exceeding 12 hours, is applied in our growth.

3.3.5 Rules of Thumb

The reaction mechanism of H₂-assistant graphene growth on Cu is still under investigation, and critical questions, such as how the crystalline structures of Cu influence the orientation of as-grown graphene, whether H₂ dissociative chemisorption is competing with the dehydrogenation of hydrocarbon by occupying the surface active sites, when the precursor dehydrogenation is completed, which form of hydrocarbon radicals CH₄ is decomposed into, remain open. Nevertheless, the process could be considered as outcome of a competition between growth of graphene with active carbon source dehydrogenated from methane and edge etching by hydrogen. And fortunately, there are several rules of thumb could be followed to design the parameters in our experiment: (1) prior to the deposition, annealing at high temperature, close to the melting point of Cu, is favorable for reducing the nucleation density; (2) oxidizing Cu surface can efficiently passivate graphene nucleation sites; (3) hydrogen plays supportive role, potential cocatalyst, in dehydrogenation reactions of methane and aids the graphene formation; (4) meanwhile, hydrogen is energetic in reaction with as-formed graphene domains and inclines to trim them into hexagon shape with zig-zag edge; (5) (with fixed H₂ flow rate) a high CH₄ flow rate leads to a short nucleation time, high growth rate, but large deviations from equiangular hexagon shape and non-uniformity in thickness; (6) on the other hand, (with fixed CH₄ flow rate) a high H₂ flow rate restricts the growth rate, the ultimate size of graphene grains, but supports the evolution of graphene into well-defined shape; (7) for long-duration growth, domain lean to have a star-like shape rather than a perfect hexagon, which points to a diffusion limited growth regime.

3.4 Synthesis of Hexagon-Shaped Graphene Crystals

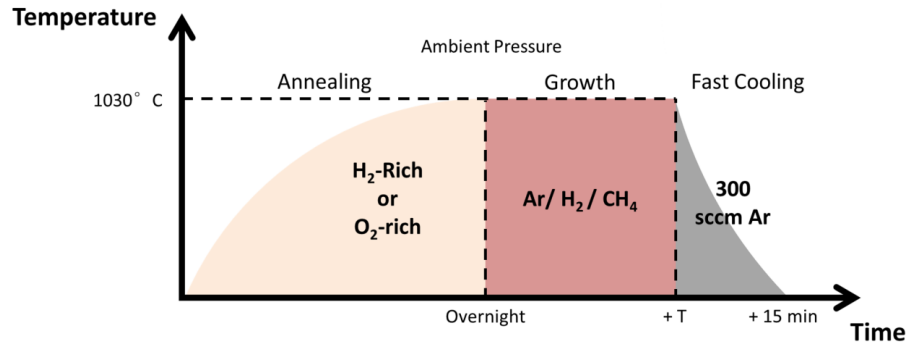


Figure 3.21 Growth recipes for monolayer hexagon-shaped graphene single crystals (not in scale).

Based on the literature study and preliminary experimental results, two protocols are developed for monolayer hexagon-shaped graphene single crystals growth, H₂-rich and O₂-rich, regarding whether supplying H₂ in the annealing process or not. Overall, an overnight annealing, typical over 15 h, is executed at as-set temperature of 1030 °C (actual temperature is expected higher than this value, since Cu foil gets melt and attached to quartz sample holder from time to time), to soften and flatten the Cu foil and enable the recrystallization and reconstruction of Cu surface. Several combinations of gas flow and duration are carried out for the growth step and detail parameters are summarized in Table 3.3. The whole process ends with a fast cooling, during which the sample holder is pushed out of the heating zone by magnetic force and cooled down to the room temperature within 15 min. The morphology of as-grown samples is studied with SEM and some quantitative results are calculated based on the SEM images from more than one sample for each growth condition and also collected in Table 3.3. There is one point need to clarify that a dilute CH₄ gas, 500 ppm in Ar, is employed in the growth and the actual CH₄ flow rate is converted and still displayed in unit of ppm.

Table 3.3 Summary of growth parameters and corresponding outcomes of monolayer hexagon-shaped graphene single crystals.

Annealing	300 sccm Ar/30sccm H ₂		300 sccm Ar		
Sample name	H ₂ -Rich No. 1	H ₂ -Rich No. 2	O ₂ -Rich No. 1	O ₂ -Rich No. 2	O ₂ -Rich No. 3
Ar/H ₂ /dilute CH ₄ flow ratio (sccm)	1454/30/16 (CH ₄ 5 ppm)	1454/30/13 (CH ₄ 4 ppm)	1454/30/16 (CH ₄ 5 ppm)	1454/30/16 (CH ₄ 5 ppm)	1949/35/16 (CH ₄ 4 ppm)
Growth period	2 h	2 h	2 h	12 h	12 h
Morphology	Hexagon, shape edge, merged	Hexagon, shape edge, isolated	Hexagon, rough edge, isolated	Hexagon, rough edge, isolated	Hexagon, rough edge, isolated
Nucleation density	Hard to determine	$< 5 \times 10^4 \text{ cm}^{-2}$	$< 175 \text{ cm}^{-2}$	Hard to determine	Hard to determine
Typical grain size (in diagonal direction)	$\sim 70 \mu\text{m}$	$\sim 45 \mu\text{m}$	$\sim 500 \mu\text{m}$	$> 1.5 \text{ mm}$	$> 1.5 \text{ mm}$

SEM images in Figure 3.22 are taken under suitable magnifications to give an overview of the samples. As expected, H₂-rich samples present nearly perfect hexagonal geometry; while, O₂-rich samples show certain deviation from symmetric structure, but still keep hexagonal shape with well-defined edges. As the outcome of aforementioned passivating effect, the nucleation density of O₂-rich samples is considerably low, especially for sample O₂-rich No.2 & 3, which are not showing here, because there are only one or few domains in a field of view. Contrastingly, H₂-rich samples possess a higher nucleation density and neighboring domains even merge into each other to form larger monolayer islands, as shown in Figure 3.22 (a). In this case, it is hard to determine the crystalline orientation of individual domain; thereby, this sample won't be used in the following Raman spectroscopy study (Chapter 5). Sample H₂-rich No.2 shows a moderate density with a value less than $5 \times 10^4 \text{ cm}^{-2}$, which agrees well with former study in our system. As

discussed in session 3.3.2, the nucleation is preferable along the textures of Cu foil and lead to a self-alignment behavior of graphene domains evidenced in Figure 3.22 (b), which endows some degree controllability in the artificial stacking experiment (Chapter 4).

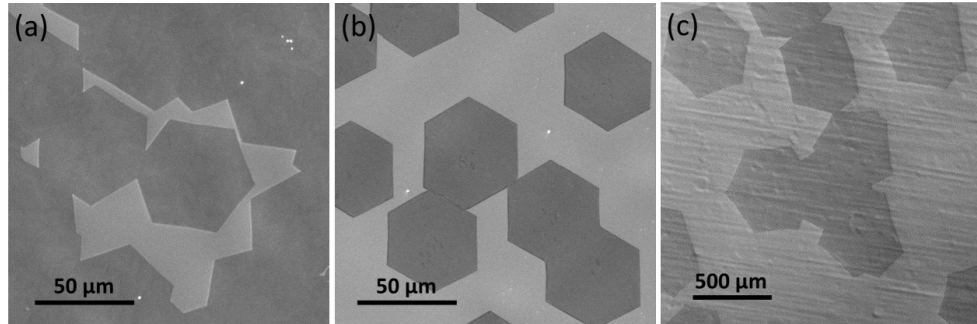


Figure 3.22 SEM images of as-grown samples under different conditions: (a) H₂-rich No. 1, (b) H₂-rich No. 2, (c) O₂-rich No. 1, with modest magnifications.

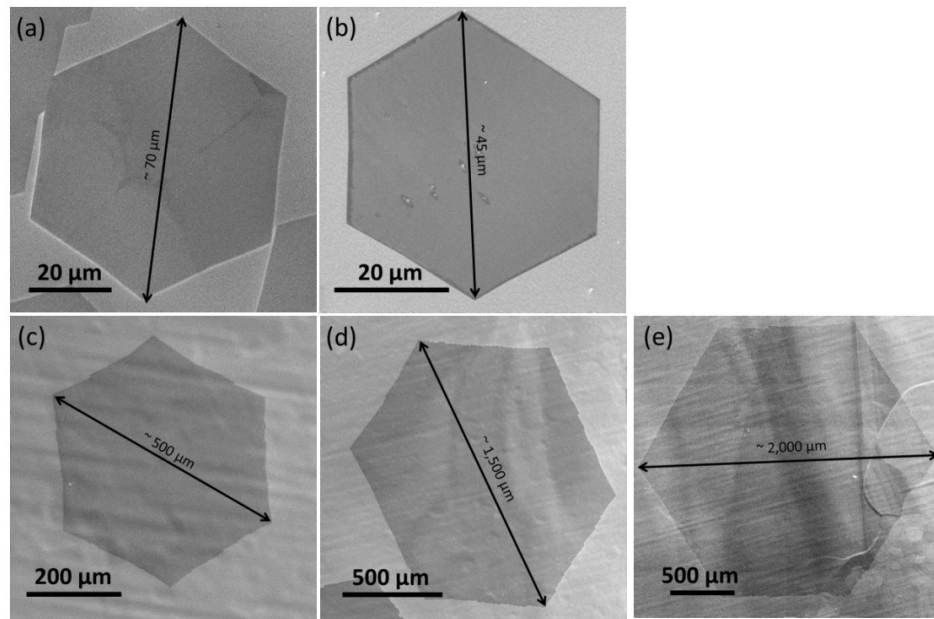


Figure 3.23 Zoom-in SEM images of as-grown samples under different conditions: (a) H₂-rich No. 1, (b) H₂-rich No. 2, (c) O₂-rich No. 1, (d) O₂-rich No. 2, (e) O₂-rich No. 3.

A series of close-up images are provided in Figure 3.23. Noticeably, the size of domain increases by ~ 10 times, just by turning off H₂ flow during annealing. Among other sophisticated methods, such as controlled pressure growth and resolidification of Cu foil, this effortless

approach has been proven capable and productive to synthesize millimeter size monolayer graphene hexagons (Figure 3.23 (d & e)).

Table 3.4 Comparison between latest reported results and O₂-rich results from this study for large size graphene single crystals growth.

Reference	3-11	3-12	3-13	3-14	3-16	This Study
Cu substrate	25 μm Cu foil (99.8% purity, Alfa Aesar)	25 μm Cu foil (99.8% purity, Alfa Aesar)	25 μm Cu foils (99.999%, Alfa-Aesar) attached on 50 μm tungsten foils (99.95%, Alfa-Aesar)	25 μm Cu foil (99.8% purity, Alfa Aesar)	25 μm Cu foil (99.8% purity, Alfa Aesar)	25 μm Cu foil (99.8% purity, Alfa Aesar)
Pretreatment	Electrochemical polish and annealing at 1077 ° C with 500 sccm H ₂ flow under 1500 Torr (~2 atm) for 7 h	Washing in HCl/H ₂ O (1:10) and annealing at 1070 ° C with 300 sccm pure Ar for 30 min	Washing in dilute nitric acid and annealing at 1100 ° C (above Cu melting point) with Ar/H ₂ ratio of 940/ 60 sccm for 30 min	Mechanical and chemical polish and annealing at 1050 ° C with Ar/H ₂ ratio of 320/21 sccm (No H ₂ flow during ramping) for 30min	Electrochemical polish and annealing at 1035 ° C with 2 sccm H ₂ flow for 15 min	As-received and annealing at 1030 ° C with 300 sccm Ar flow for overnight (more than 12 h)
Growth pressure (Torr)	~ 108 Torr	0.75 ~ 3.75 Torr	760 Torr	760 Torr	Low pressure	760 Torr
Ar/H₂/CH₄ flow ratio (sccm)	0/70/0.15	Total flow of 350 sccm with varied H ₂ /CH ₄ ratio from 100/150 to 150/50 (500 ppm dilute CH ₄ in Ar)	Total flow of 1000 sccm, 854/100/46 (0.1% dilute CH ₄ in Ar)	320/21/15 (500 ppm dilute CH ₄ in Ar)	0/10/0.1	Total flow of 1500 sccm, 1454/30/16; Total flow of 2000 sccm, 1949/35/16 (500 ppm dilute CH ₄ in Ar)
Growth temperature	1077 ° C	1070 ° C	1075 ° C	1050 ° C	1035 ° C	1030 ° C
Growth period	125 min	2 h to 48 h	300 min	Tens of hours	6 h	2 h to 12 h
Morphology	Monolayer, hexagonal shape, as large as 2.3 mm in diagonal direction	Monolayer, hexagonal shape, as large as 5 mm in diagonal direction; Bilayer (with continuous 1 st layer), hexagonal shape, as large as 300 μm	Monolayer, hexagonal shape, as large as 1 mm in diagonal direction	Monolayer, hexagonal shape, as large as 5 mm (merged)	Monolayer, near hexagonal shape with dendrite edges, as large as ~ 2 mm in diagonal direction	Monolayer, hexagonal shape, over 1.5 mm in diagonal direction

To be clarified, synthesis of high-quality hexagon graphene single crystals is a major topic of this thesis, but not the only one. From this point of view, the study doesn't origin from theoretical or simulation works; instead, it follows the empirical rules, proposes feasible growth recipes, and testifies them. Although a further optimization of parameters and a deeper understand of growth mechanism are demanded, which are actually being carried out by collaborators, the quality of samples achieved here is comparable with most state-of-art results in literature, as shown in Table 3.4, and is believed competent in both fundamental studies and applications tasks.

Beyond monolayer hexagon graphene single crystals, twisted bilayer domains are a catalog of bilayer graphene structures staking with various orientations, which are expected more promising for electronic and photonic applications. There are two types of bilayer samples applied for Raman spectroscopy study (chapter 5), CVD grown and artificial stacked. Growth recipe for the former can be described as Figure 3.22 schematically, and stacking protocol for the later will be explored in chapter 4. Since the credit of synthesizing these bilayer samples by CVD methods belongs to one of the collaborators, the experimental details won't be elaborated here¹¹⁸.

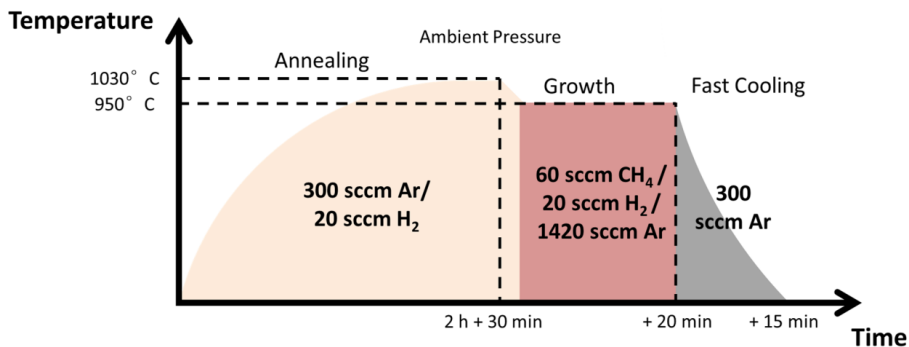


Figure 3.22 Growth recipe for bilayer hexagon graphene samples by CVD (not in scale).

Chapter 4 Transfer and Artificial Stacking of Graphene Crystals

Transferring graphene samples, synthesized by chemical vapor deposition, from catalytic metal to target substrate is crucial for most applications in electronics and photonics, where an insulator substrate is more desirable^{130, 131}. In fact, transfer is necessary even for fundamental characterization. Due to the difference in conductivity, graphene can be visualized on Cu foil under secondary electron microscope (SEM); but lack of optical contrast, it is impractical to be identified under optical microscope. Although, recent work demonstrates the possibility of imaging graphene directly on oxidized Cu foil after growth¹³², the Cu foil with only 25 μm in thickness, commonly used in growth, is easy to deform and also not friendly to optical measurements. After reviewing developed transfer methods, polymethyl-methacrylate (PMMA) assistant wet transfer is adapted. Following a wide-spread protocol, how to transfer as-grown graphene samples onto insulator surface (SiO_2/Si) and optical window (CaF_2) is demonstrated in this chapter. Moreover, an approach to create large area of twisted bilayer graphene sample is proposed and verified.

4.1 Transfer Methods

Along with the development of synthesis process, a variety of transfer methods have been invented. But only those are compatible with CVD synthesis will be discussed here. As mentioned above, the catalytic metal substrate, Cu in our case, which graphene is synthesized on is typically unwanted for further characterization and applications, so the removal of metal is a logical step after the CVD growth.

4.1.1 Removal of Catalytic Metal Substrates

One of the most straightforward approaches to remove active metals, like Ni and Cu, is dissolving them into oxidant solution (Figure 4.1 (a))¹³³. Numerous chemicals are capable to fulfill this task, such as HCl, HNO₃, FeCl₃, Fe(NO₃)₃ and (NH₄)₂SO₈¹¹⁴. FeCl₃ and Fe(NO₃)₃ are widely adapted, because they are less toxic, and more gently and effectively etch the copper without forming gaseous products or precipitates. In contrast, reactions during etching with acid lead to the emergence of H₂ bubbles or corrosive vapors which cause cracking in the graphene film and also degrade the carbon sp² network.

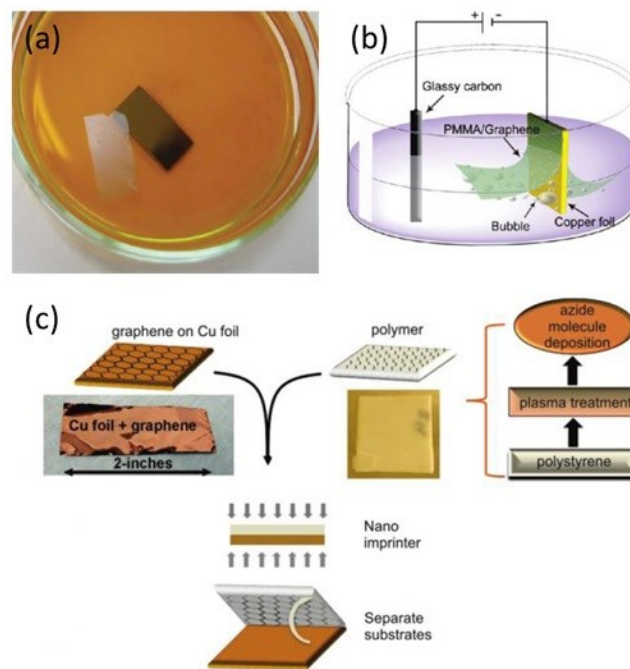


Figure 4.1 Removal of catalytic metal substrate by chemical etching (a), electrochemical reaction (b), and mechanical exfoliation (c).

Electrochemical approach also can separate graphene and the metal substrate but through delamination, in which the metal substrate is recyclable (Figure (4.1 (b))¹³⁴. However, the

side-effect from gaseous products is unavoidable in these electrochemical reactions and results in a relatively poor quality.

Mechanical exfoliation can provide another etching-free approach for CVD grown samples on Cu (Figure 4.1 (c))^{135, 136}. Since the interaction between graphene and Cu is just van de Waals force, even it is stronger than the one between graphene and Si wafer¹³⁷, Cu foil can be peeled off from the back, once a tighter bond between graphene and the target substrate is presented. Therefore, a “glue”, for example epoxy or N-ethylamino-4-azidotetrafluorobenzoate (TFPA-NH₂) linker molecules, which can establish covalent carbene bonds with graphene, is crucial to accomplish this clean transfer. On the other hand, the strong link raises an issue in removing these glue substances and obtaining a clean graphene/substrate interface, unless the objective usage is immune to the substrate cleanliness.

Considering the practicability and cost, a regular chemical etching process with Fe(NO₃)₃ solution is applied in this study. Although directly transferring graphene without any supporting layers has been demonstrated in some early studies, the atomic thin graphene is too vulnerable and prone to ripping and tearing during etching and transfer process. In aim to improve the reliability and reproducibility of transfer, a number of strategies have been implemented, among which three well-studied ones will be elaborated in the following subsections.

4.1.2 Polydimethylsiloxane (PDMS) Assistant Transfer

PDMS is a type of elastomeric polymer, which can be casted onto graphene surface in liquid phase or can conformally contact with graphene in a form of cured block, called stamp (Figure 4.2 (a))¹³⁸. The PDMS stamp is typically solid enough to stand freely and provide

sufficient mechanic support to graphene, but is still flexible to buffer the surface tension. After etching away the Cu foil, the whole PDMS/graphene block can be pulled out of the solution and stamped onto target substrate. Due to a low surface free energy, PDMS stamp hold a comparably weak adhesion force with graphene. This allows them easily released, as long as the target substrate offers a stronger contact with graphene. The stamping process owns a “built-in” site-specific capability, but also a substrate selectivity¹³⁹, which limits its applicability to hard, flat and hydrophilic surfaces, and often results in fragmentation of the fragile graphene sheet. Recently, a PDMS based method has been proposed to transfer graphene onto soft surfaces, but with additional assistant from a sacrificial layer, which still needs to be chosen carefully¹⁴⁰. Besides, the PDMS assistant transfer always suffers an excruciatingly slow etching process, taking more than tens of hours.

4.1.3 Polymethyl-methacrylate (PMMA) Assistant Transfer

Compared with PDMS, which maintains weak van der Waals forces with graphene, PMMA coating can form strong covalent bonds with graphene. Regularly, a thin layer of PMMA, hundreds of nanometer in thickness, is spinning coated onto graphene grown on Cu foil (Figure 4.2 (b))¹⁴¹⁻¹⁴⁴. After the etching process, the PMMA/graphene membrane can float on the solution surface and is ready to be scooped by the target substrate. Then the PMMA supporting layer can be removed by organic solvent, usually acetone. Apparently, the PMMA assistant approach is less critical on substrate, it has been performed on flexible surfaces, like Polyethylene terephthalate (PET)¹⁴³, and even porous surfaces, like carbon transmission electron microscope grids¹⁴⁴. But the scooping process comparatively lacks of control in landing graphene onto specified positions. A

more serious issue is the PMMA residues, which cannot be completely washed away by acetone, could undermine the electronic properties of as-transferred graphene samples. Post-treatment or alternative solvent is required to overwhelm this issue, and which will be deliberated in Section 4.2.

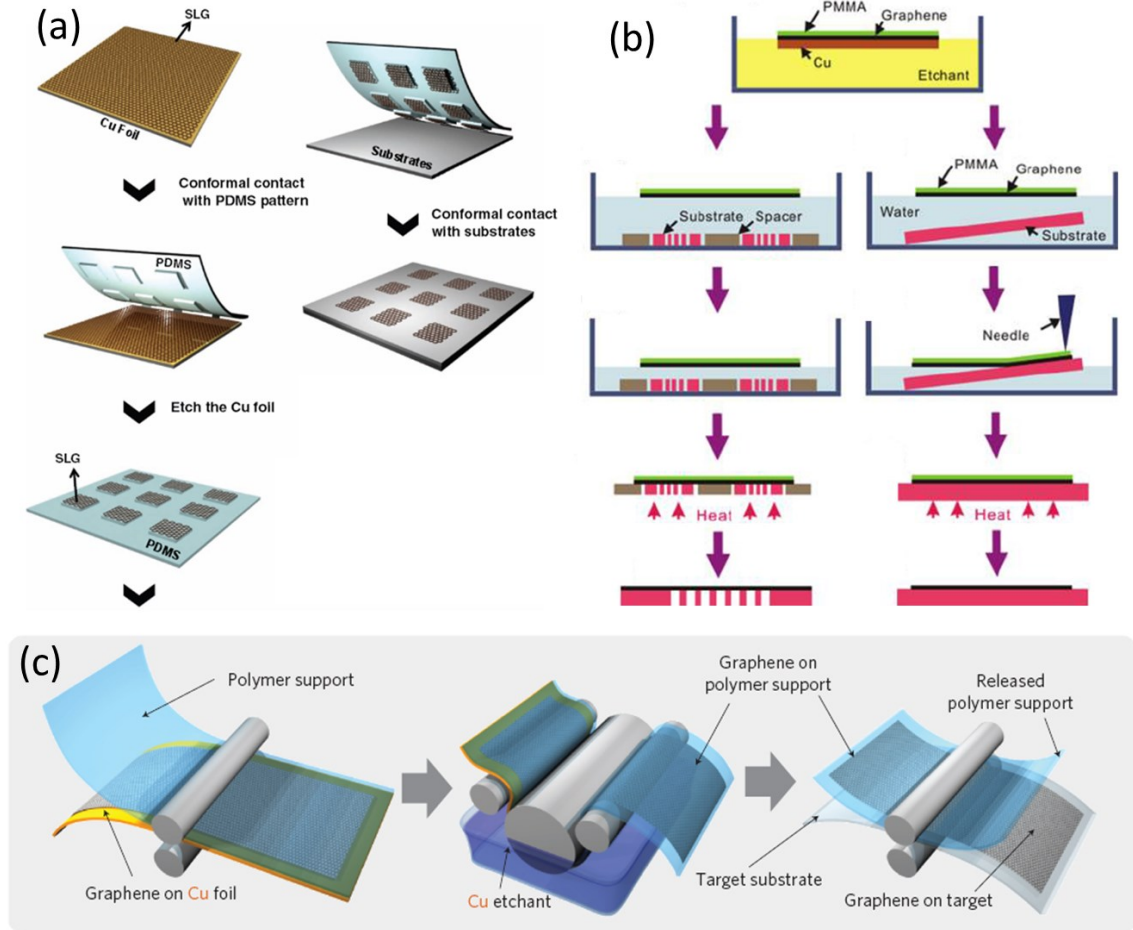


Figure 4.2 (a) Transfer process with a pre-patterned PDMS stamp. (b) PMMA assistant transfer process applied on perforated substrates and flat substrates. (c) Thermal release tape based roll-to-roll technique to realize transferring of 30-inch size of graphene.

4.1.4 Thermal Release Tape Assistant Large-Scale Transfer

With the experience acquired from transferring graphene grown on SiC, thermal release tape can play alternative of aforementioned polymers¹⁴⁵. Thanks to the unique thermal releasing

property, the tape is firstly pressed onto graphene covered Cu foil and attaches to it by adhesive force. Similar as PDMS assistant approach, after removal of Cu, the tape/graphene can be placed on the target substrate and the tape can be simply detached with a modest heating temperature around 120 °C. However, thermal release tape is not merely an alternative to polymers. The true merit of thermal release tape lies in its application for roll-to-roll transfer of graphene, which can achieve large scale graphene film with 30 inch diagonal dimension (Figure 4.2 (c))¹⁴⁶. The downside is in the roll-to-roll or later developed hot pressing process, the rigid and shear stress is potentially harmful to graphene layers, creating cracks or holes¹⁴⁷. In addition, thermal release tape may leave residue, just like PMMA.

4.2 Experiment Details of PMMA Assistant Wet Transfer

4.2.1 General Protocol

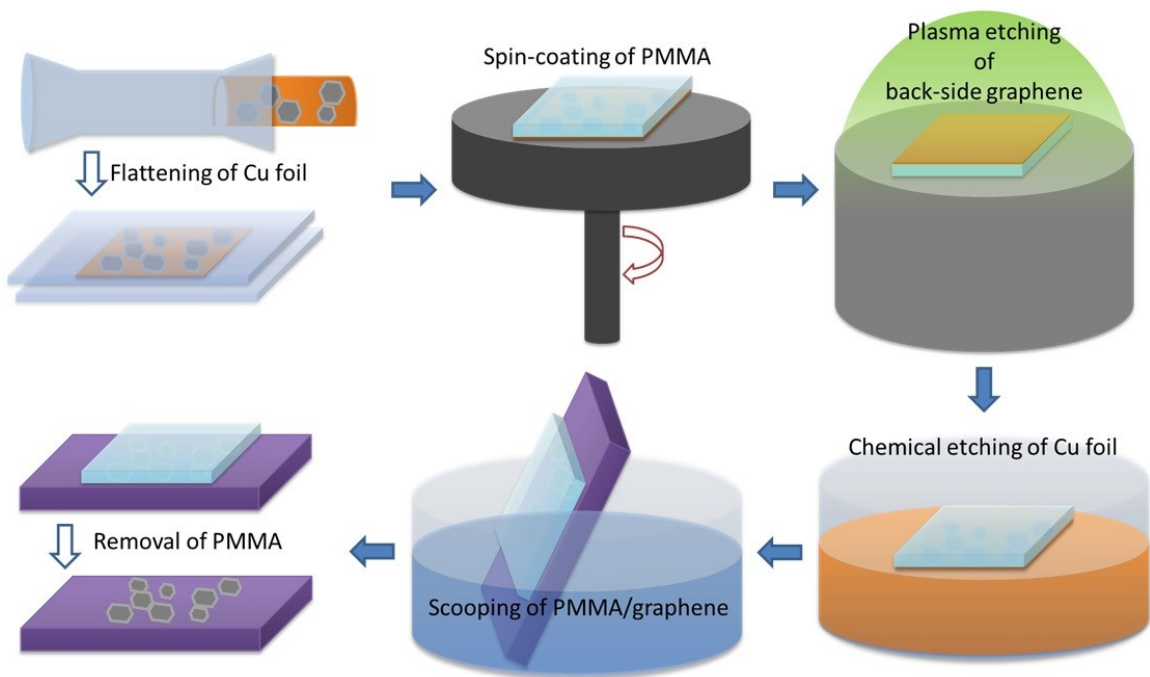


Figure 4.3 Flow chart of PMMA assistant wet transfer applied in this study.

Upon the above discussion, the PMMA assistant wet transfer, which is and will most likely be the dominant method in laboratory scale graphene transfer, is employed, but with extra attention to reducing undesired residues. The flow chart shown above is outlined the main steps in PMMA assistant wet transfer of graphene domains from Cu foil to target substrates, Si wafers with ~300 (or ~285) nm thick of oxidized layer or CaF₂ windows. In our synthesis procedure, the Cu foil is wrapped into cylindrical roll to overcome the loss of Cu through evaporation during high temperature annealing and growth. So after synthesis, the Cu foil with graphene grown on is flatten by pressing between two glass slide. After examined by secondary electron microscope (SEM), one side of a graphene sample is spin-coated with a thin layer of PMMA (MicroChem 950 PMMA C, 3% in chlorobenzene) at 3000 rpm for 1 min, which was then cured at 100 °C for 1 min. This mild curing condition is based on the concern that over-baking may stiffen the PMMA layer and create cracks in as-prepared graphene samples. It should be noted that, graphene can formed on both side of the Cu foil, as shown in Figure 3.16 in chapter 3. A plasma etching step is introduced to dissolve the permeability barrier, as which the back-side graphene may act, and is beneficial to the following step of Cu removal. Besides the possible barrier effect, this back side graphene intends to leave some abominable marks. The back etching step, which has been overlooked in most of the reported papers, will be evaluated below. After the back etching, sandwich-structured PMMA/graphene/Cu foil is placed on the surface of 0.1 g/ml (15g in 150 mL) iron nitrate solution, with clean Cu side immersed in. There is no observable Cu remains after a 4-hour etching, but an extended duration, overnight, is taken to ensure the completeness of reaction. The PMMA/graphene membrane is washed in deionized water (DIW)

for triple times. A target substrate, which is sequentially cleaned in acetone, isopropyl alcohol (IPA), and DIW with sonication bathing and dried by nitrogen gas, carefully approaches to the floating PMMA/graphene membrane and picks it up. The excess water between PMMA/graphene membrane and substrate is dried out naturally in air. During this drying step, a considerable van de Waals force arises, binding graphene and the substrate together. The final step is removing PMMA in hot (~60 °C) acetone, washing with IPA and DIW for several times, and drying sample in N₂ gas. Including etching of back side graphene, some key factors will be investigated and optimized in the following subsections.

4.2.2 Removal of Back Side Graphene by Plasma Etching

Since CVD is a heterogeneous chemical reaction process, graphene can grow on both side of Cu foil. One argument of removing the redundant graphene layer is that it may impede the Cu etching, considering the solution and chemicals permeability of graphene. In some initial studies, a mechanical polishing or O₂ plasma etching step is prescribed to remove the back side graphene¹⁴³. But it is seldom mentioned in later improved PMMA assistant wet transfer recipes.

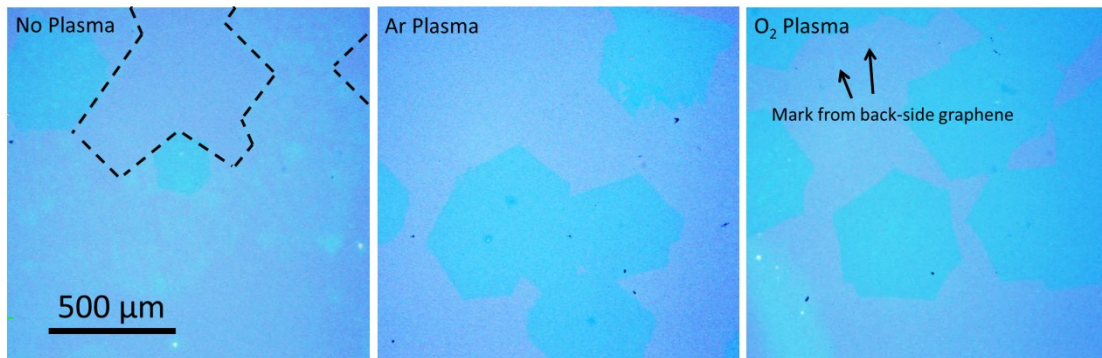


Figure 4.4 Optical images of transferred graphene samples on SiO₂/Si substrate without plasma etching of back side graphene (left), with 5 min Ar plasma etching (middle), with 5 min O₂ plasma etching (right).

The transfer recipe previously developed in our group adapts a 1-minute O₂ plasma (50 W forward power, 20 sccm O₂ flow rate). But some film-like residues appear constantly on the as-transferred samples. And interestingly, these residues show well-defined or even quasi-hexagonal outlines, as labeled in Figure 4.4. This issue becomes severe, if skipping the O₂ plasma step. It's reasonable to infer that these residues may come from the back side graphene.

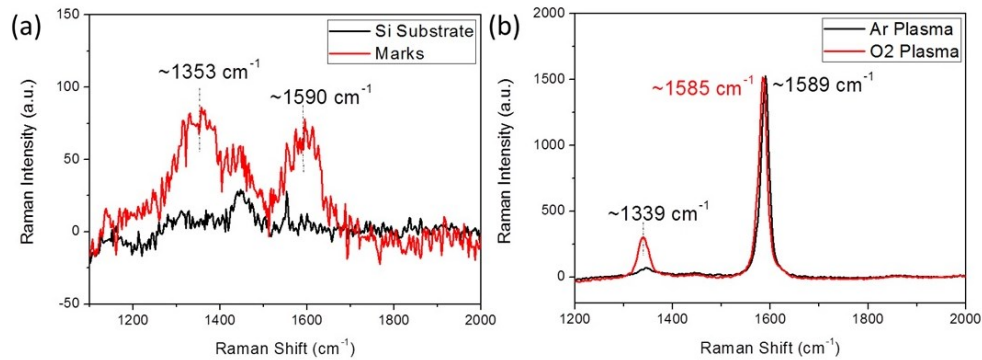


Figure 4.5 (a) Comparison of Raman spectra collected from clean SiO₂/Si surface and marks of back side graphene on one O₂ plasma treated sample. (b) Raman spectra of graphene samples treated with 5 min Ar plasma and O₂ plasma back etching, respectively.

In order to remove the back side graphene completely, extended duration and different plasma species, Ar plasma, are carried out. Through a same duration of etching (along with same forward power and flow rate), sample treated with Ar plasma has a cleaner appearance in optical microscope images (Figure 4.4) and also noticeably less defects as revealed in Raman measurement (Figure 4.5 (b)). Amorphous carbon signals can be detected from those marks left by back side graphene on the O₂ plasma treated sample (Figure 4.5 (a)). Figure 4.6 exhibit the photo of Cu foil without back etching, with 5 min of Ar plasma etching, and with 5 min of O₂ plasma etching, after heating at 150 ° in humid atmosphere overnight. Serious oxidized Cu surface of the one treated with Ar plasma suggests the lack of protection from graphene.

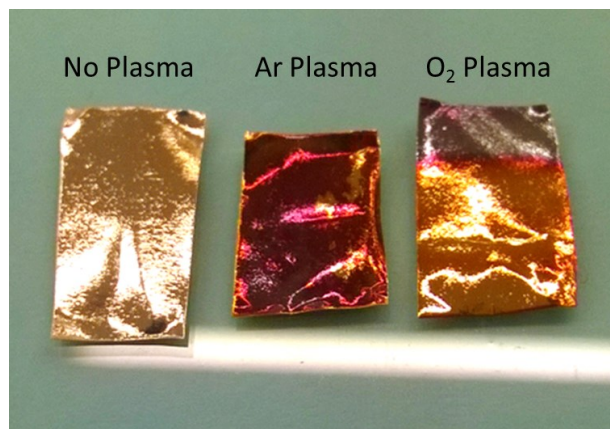


Figure 4.6 Oxidation tests of Cu foils without plasma etching of back side graphene (left), with 5 min Ar plasma etching (middle), with 5 min O₂ plasma etching (right).

It has been realized that the removal of graphene by O₂ plasma is based on oxidation reaction between O⁺ and C to form volatile products. The oxidation preferentially starts at the defect sites of graphene, mainly at the edges, where the reactivity of carbon atoms is higher than that of the fully bonded sp² coordinated carbon atoms¹⁴⁸. But for continuous, defectless graphene film, the step prior to oxidation is to overcome a very high energy barrier and make the first defects. It is evident that the energy of O₂ plasma applied in above tests is countable for breaking down the delocalized sp² structure of graphene, but not adequate to wipe off all the carbon fragments. On the contrary, Ar plasma etching is basically a sputtering process, regardless of the reactivity. Therefore, under our experimental condition, Ar plasma performs energetically in etching of back side graphene and is employed in the general protocol of transfer.

4.2.3 Minimizing of Cracking during Transfer

To minimize the cracking of transferred graphene samples, two strategies, dehydrating target substrate and applying additional PMMA, are practiced here. As shown in chapter 3, the

as-synthesized graphene is ideally flat. It tends to follow the waves and steps of underlying Cu foils and also wrinkles inevitable arise due to the huge difference in thermal expansion coefficient of graphene and Cu. These geometric defects will remain even the Cu foil is etching away. Therefore, when graphene contact with a much flatter surface, such as a polished SiO₂/Si wafer, there are always some small gaps between the graphene and the substrate surface. These unattached regions are more likely to break when the PMMA supporting layer dissolved away.

It is important to enhance the adhesion between graphene and target substrate which highly depends on the roughness of the substrate and its hydrophobicity. Therefore, following the standard cleaning step, the target substrates are heating up to 120 °C for 20 min, as fulfilled in most lithography process, to dehydrate.

Controlling the rigidness of PMMA supporting layer is also crucial to reduce the cracks. It is assumed that the hard PMMA layer is harmful, since the graphene cannot relax when it is removed away. For this reason, the curing of PMMA is executed at a relatively low temperature (100 °C), as mentioned in 4.2.1. Moreover, after scooping the PMMA/graphene stack onto the target substrate, an additional drop of liquid PMMA solution is applied on the cured PMMA layer. This redissolution of PMMA has been demonstrated favorable to mechanically relax the underlying graphene, leading to a better contact with the substrate.

4.2.4 PMMA Residue /Substrate Doping Effects and Post-Annealing

Previously stated, residue of PMMA is one of the most serious issues that undermine the quality of as-transferred graphene samples. These residues tend to have a p-doping effect on graphene and cause carrier scattering, thus leading to a degradation of the electrical properties.

The aforementioned redissolution of PMMA is helpful to decrease the residues, to a certain extent, but not sufficient to solve the problem. Besides PMMA residues, the moisture and oxygen trapped between graphene and the substrate are always accused for the doping effect. Different from dry oxygen, the wet ambient unintentionally dopes graphene from the edges and grain boundaries or from the substrate in the vicinity of the edge¹⁰⁹.

A post-annealing (150–300 °C, under H₂/Ar, H₂/N₂, or ultrahigh vacuum) has been widely used and is expected to burn off the PMMA residues and repel the moisture. However, recent studies show that the influence of post-annealing is quite controversial. As suggested in the reference, the PMMA facing the air starts to decompose at a rather low temperature, ~160 °C, but the PMMA directly contacting with graphene is much more stubborn, which cannot be totally removed at over 700 °C in a high vacuum chamber. It means a lower-temperature annealing (~200 °C) can somehow restore the intrinsic properties of graphene; a higher-temperature annealing (> 250 °C) does not really yield a much cleaner surface, but at the risk of structural damages of graphene. Overall, it remains far from satisfactory for gaining clean surface in large areas. Also, the effect of post-annealing on eliminating substrate doping is not as straightforward and promising as predicted. Since the edges and grain boundaries are involved, the doping of wet ambient is not fully recoverable, even upon vacuum annealing. Contrarily, in the annealing taken place under less vacuum condition, the dry oxygen doping emerges at a temperature higher than ~400 °C, thereby aggravate the doping effect¹⁴⁹. Moreover, in-plane compression and rippling have been witnessed on graphene supported on SiO₂/Si substrates, due to conformal adhesion or differential thermal expansion, when annealed at > 100 °C.

On balance, post-annealing treatment is declined in preparation of graphene samples in this study. Furthermore, to suppress any unexpected thermal effects, no heating temperature excess 150 °C is allowed during the whole transfer process.

4.2.5 Visualization of Graphene by Oxidizing Cu Foil

As mentioned at the beginning of this chapter, the graphene domains can be directly visualized on oxidized Cu foil. Thanks to the barrier effect of graphene, the graphene covered Cu foil can survive during mild thermal annealing in air (150 °C, 30 min in our case), while naked Cu foil is oxidized and present interference color contrast, as shown in Figure 4.7. This color contrast provides a simple and quick approach to examine the morphology of as-synthesized graphene domains.



Figure 4.7 Photo of graphene domains on oxidized Cu foil.

To verify the graphene quality after Cu oxidation, Raman spectroscopic measurement is employed. Here only the conclusive results are covered, the theoretical explanations and experimental details will be discussed in the next chapter. Figure 4.8 (a) provide an optical microscope image of a monolayer graphene domain on oxidized Cu foil, in which graphene covered Cu shows bright rose gold color, oxidized Cu looks duller by contrast. Quasi-parallel-line

textures of commercial Cu foil, also mentioned in Section 3.3.2, can be clearly observed under a 10× objective here. In order to prevent the disturbance from strong luminescence background of Cu foil, a laser with relatively low energy, 1.94 eV, is utilized to excite the Raman scattering and the collected spectrum is given in Figure 4.8 (b). The band position and the full width at half maximum of characteristic bands, G band and 2D band, are comparable with as-grown graphene samples by CVD method. A negligible D band ascribed to the structural defects, and a large intensity ratio of A(2D)/A(G) suggest the annealing process is fairly nondestructive to graphene.

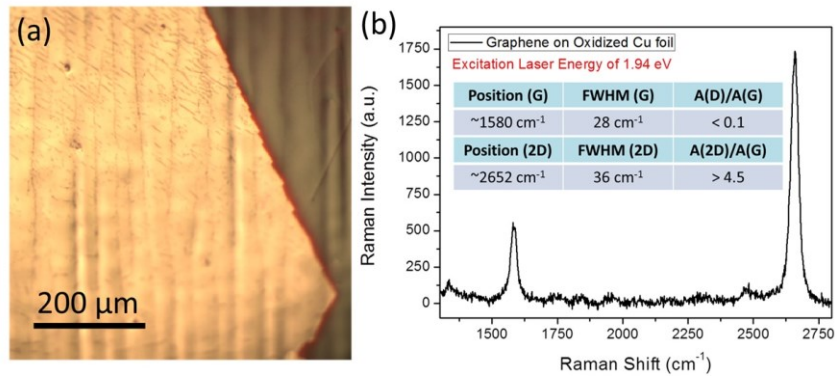


Figure 4.8 (a) Optical microscope image of a graphene domain on oxidized Cu foil. (b) A typical Raman spectrum collected from the graphene domain shown in (a).

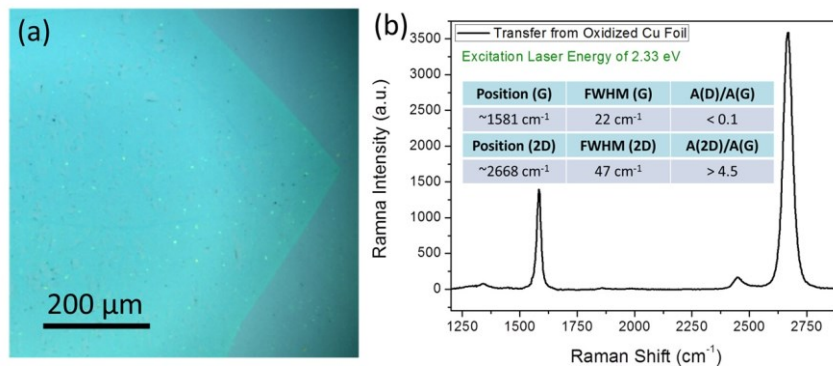


Figure 4.9 (a) Optical microscope image of a graphene domain transferred from oxidized Cu foil onto a 300 nm SiO_2/Si substrate. (b) A typical Raman spectrum collected from the graphene domain shown in (a).

To further demonstrate the transferability of graphene on oxidized Cu, the sample is transferred onto a 300 nm SiO₂/Si substrate using the general protocol. The optical microscope image and corresponding Raman spectrum of transferred domain are shown in Figure 4.9. Although a narrowed G band and expanded 2D band indicate the doping effect introduced by the transfer, the graphene domain still preserves a small intensity ratio of A(D)/A(G) and a large A(2D)/A(G). It should be pointed out that a different excitation laser with energy of 2.44 eV is used here, which is responsible for the position shift and broadening of 2D band. And slightly narrower G band may results from the substrate doping. Also worth to mention, the spectrum of transferred sample presents a significantly larger signal to noise ratio than the one on Cu foil, because of the interference effect originated from the interface of dielectric SiO₂ layer and graphene.

4.3 Transfer of Monolayer Graphene Crystals

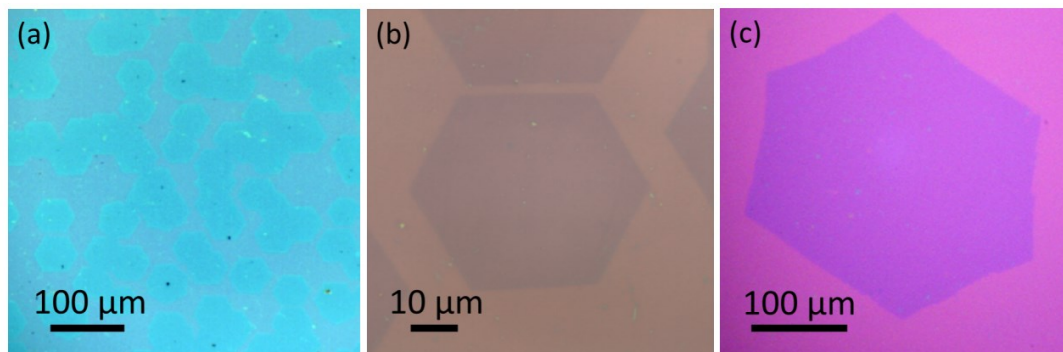


Figure 4.10 Typical optical microscope images of H₂-rich sample (a-b), and O₂-rich sample (c) under different magnification.

There are two types of monolayer graphene crystals synthesized in this study, H₂-rich and O₂-rich, distinguished by whether flowing H₂ gas during the annealing step. As discussed in the

last chapter, H₂-rich samples possess nearly perfect hexagonal shape with modest dimensions, tens of micrometers; while O₂-rich samples is giant in size, hundreds of micrometer to a few of centimeters, but with some imperfection in morphology. Figure 4.9 exhibit typical optical microscope images of H₂-rich (a-b) and O₂-rich graphene crystals after transferred. It is noticeable that the substrates appear different color due to the different thickness of SiO₂ layer: the one with 285 nm SiO₂ layer looks purpler, but the one with 300 nm looks bluer.

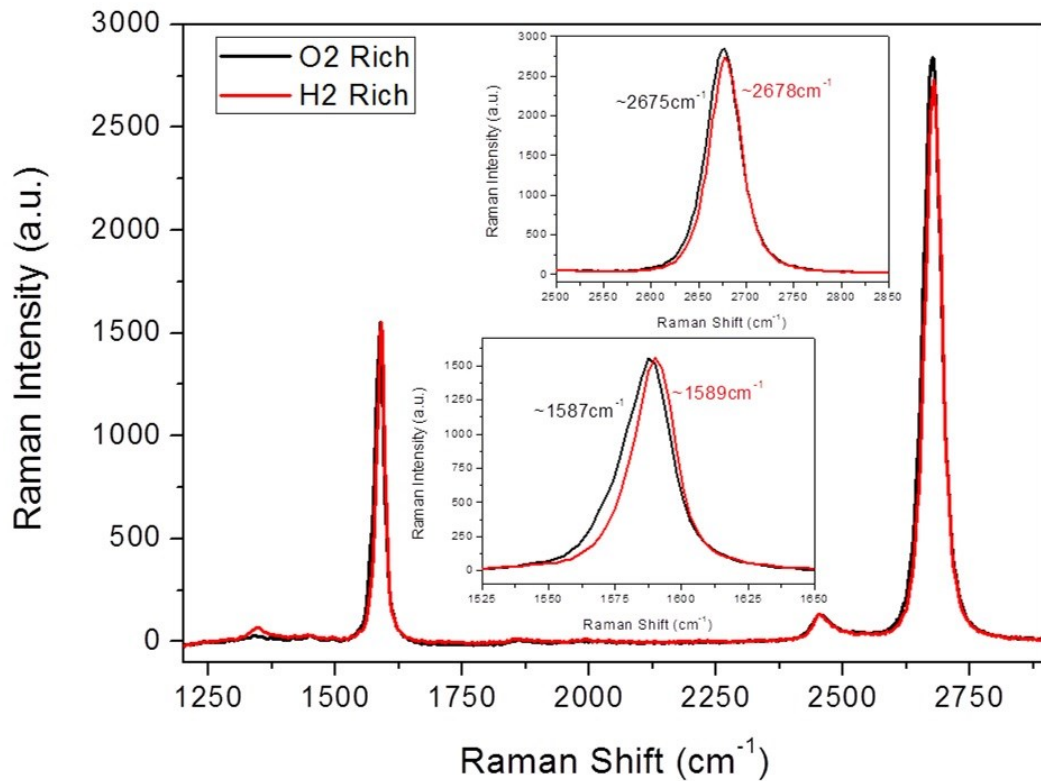


Figure 4.11 Typical Raman spectra collected from the H₂-rich and O₂-rich graphene domain shown in Figure 4.10, respectively.

The corresponding Raman spectra are provided in Figure 4.11. Both spectra have sharp and symmetric G band and 2D with comparable large A(2D)/A(G) ratio, implying the single layer nature. H₂-rich sample shows a slightly larger intensity of D band, which is understandable in the

consideration of etching effect of H₂. But a decent A(D)/A(G) ratio suggests a satisfactory crystalline quality. The negligible shifts in band position, both G band and 2D band, could be attributed to the substrate doping effect or bias in measurement.

4.4 Creation of Twisted Bilayer Graphene by Artificial Stacking

In highly crystalized graphite samples, Bernal stacking is the most favorable stacking order between adjacent layers. However, bilayer graphene with twisted stacking orientation can be witnessed on the samples synthesized by CVD method or silicon sublimation of SiC, due to the weak coherence between two layers, which are mediated through catalytic metal or SiC substrates during synthesis. Latest theoretical calculation also expects that there is no preference for the twisted angle in the experimental bilayer graphene samples, from the interlayer energy point of view¹⁵⁰.

The rotation-angle dependent electronic band structure is the most remarkable feature of twisted bilayer graphene. Creation of large area twisted bilayer graphene with predefined rotation angle is not only an intriguing topic in material science, but also a promising approach to engineering the electronic and photonic properties of graphene for further application. But apparently, conventional thermal synthesis methods couldn't be competent for this task.

Beyond thermal synthesis, artificial stacking has revealed considerable potentials in creating twisted bilayer graphene. The concept has been demonstrated on mechanical exfoliated flakes as early as in 2008⁶¹. The folded graphene flakes by water flushing displayed quite distinct Raman features, compared with their Bernal stacking counterparts. However, the size of as-prepared twisted bilayer areas is only few of micrometers, and the rotation angle is still

uncontrollable. Layer-by-layer stacking of CVD grown graphene films is also a widely applied strategy to create large area multilayer films, which is difficultly achieved in direct growth. But whether there is interaction between as-stacked layers is still under debated. Unlike samples from mechanical exfoliation, transferred graphene samples always suffer the aforementioned PMMA residue issue, which is suspected to separate the adjacent layers and thus impede the formation of binding between them.

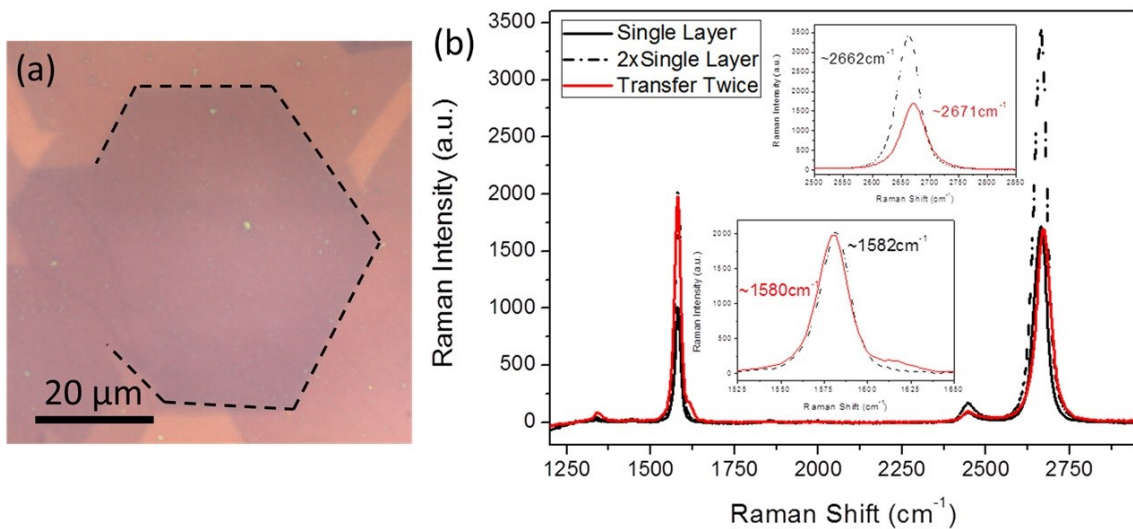


Figure 4.12 (a) Optical microscope image of a bilayer graphene sample prepared by artificial stacking of two H₂-rich graphene layers. (b) Typical Raman spectra collected from single-layer area and the overlay area outlined in black dash line in (a).

But in our experiment, a similar Raman behavior as bilayer samples directly grown by CVD has been noted on bilayer samples prepared by artificial stacking. Figure 4.12 (a) labeled out a quasi-hexagon overlay area consisting of two H₂-rich graphene layers. Uniform Raman signals have been detected over this hundreds-of-micrometers area and a typical spectrum is presented in Figure 4.12 (b). Assuming there is no interaction between these two layers, the Raman signal should have a similar profile, band position and band width, as single layer, but

with doubled intensity (black dash line in (b)); while, this disobeys our observation. The 2D intensity of overlay part is comparable with the one of single layer, but the band position of 2D band shifts by 9 cm^{-1} . The PMMA residue or substrate doping effect may have some contribution to this significant blue shift, but most likely it comes from the flattened band structure and reduced Fermi velocity of twisted bilayer.

To rule out the suspected impact of PMMA residues, an alternative stacking procedure is carried out, in which the first PMMA/graphene layer is transferred onto a new graphene grown on Cu foil and then they are transferred together onto target substrate without PMMA in between. Distinguished from the original layer-by-layer stacking approach, which is represented by “separate”, this one is referred as “together”. Figure 4.13 gives two bilayer samples obtained by stacking together and separately of two O_2 -rich layers, respectively. The Raman profile of overlay regions on both samples deviates from the simple double of the single-layer one. More noticeably, the two set of spectra have an equivalent defect level, inferred from a similar $A(\text{D})/A(\text{G})$ ratio. It seems the effect of PMMA residues is not as profound as presumed.

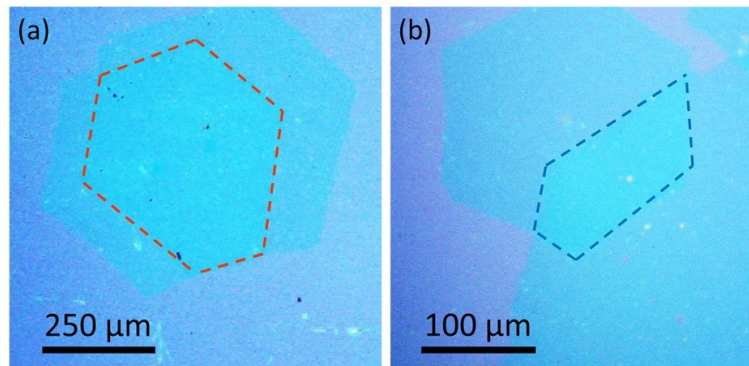


Figure 4.13 Optical microscope images of bilayer graphene samples prepared by “together” stacking (a) and “separate” stacking (b) of two O_2 -rich layers.

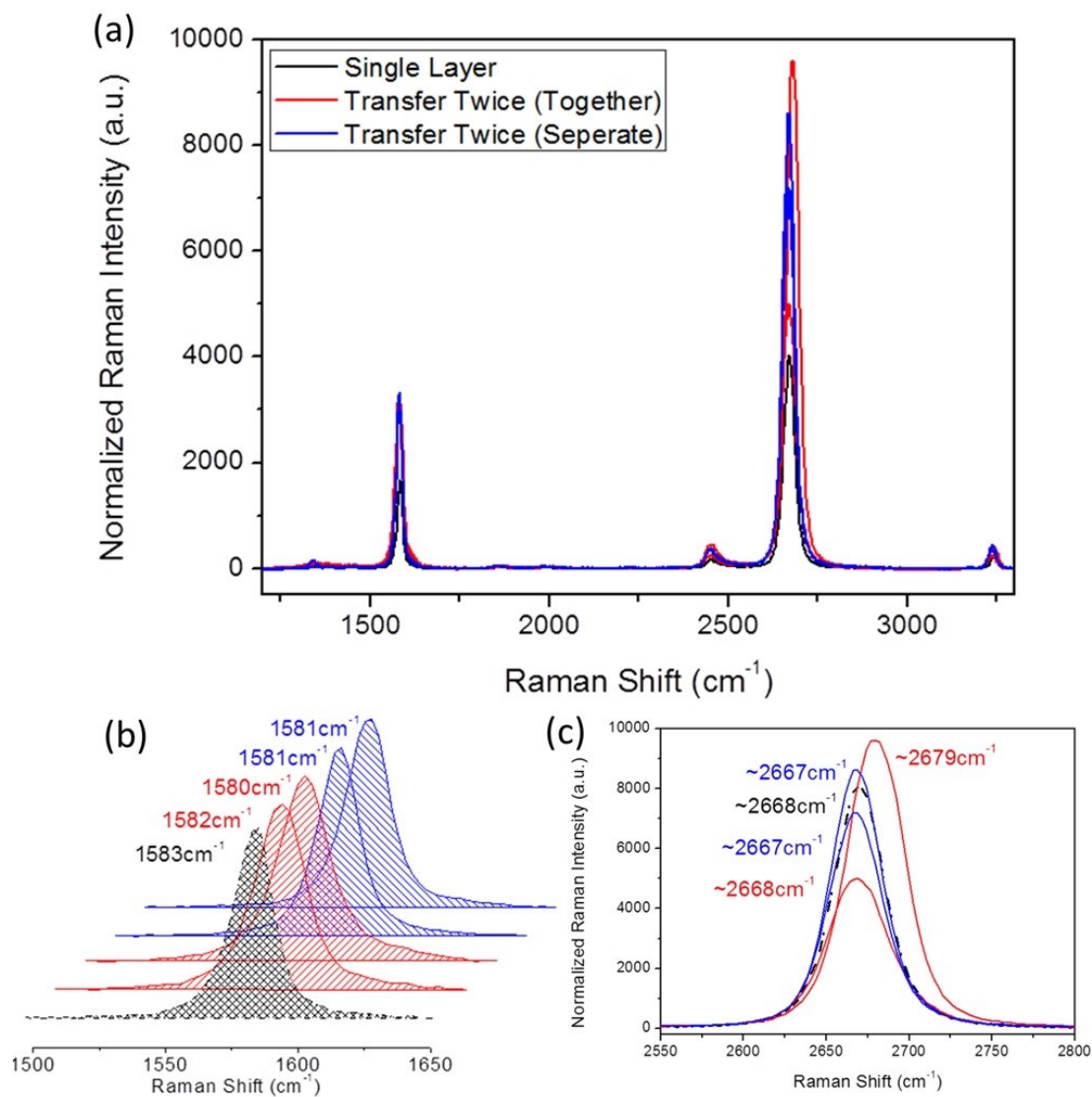


Figure 4.14 Typical Raman spectra collected from single-layer area and overlay areas on samples prepared by “together” stacking and “separate” stacking of two O₂-rich layers: overview (a), enlarged view of G band (b), and 2D band (c).

To observe the difference clearly, the spectra are normalized based on the intensity of G band and two times of single-layer spectrum is plotted in black dash line. Again, compared with the slight blue shifts in G band, non-ignorable shifts in 2D band have been observed, which couldn't be explained by doping or strain effects. And the intensity of 2D band can dramatically

vary upon different stacked regions. These anomalous Raman behaviors signify an underlying relation between stacking order and electronic band structures, which will be further discussed in the next chapter.

By far, the feasibility of creating twisted bilayer graphene by artificial stacking of two graphene layers synthesized by CVD method has been verified. Although the precisely stacking of two domains with predefined rotation angle has not yet been accomplished, the visibility of large size graphene single crystals endows certain controllability during transfer.

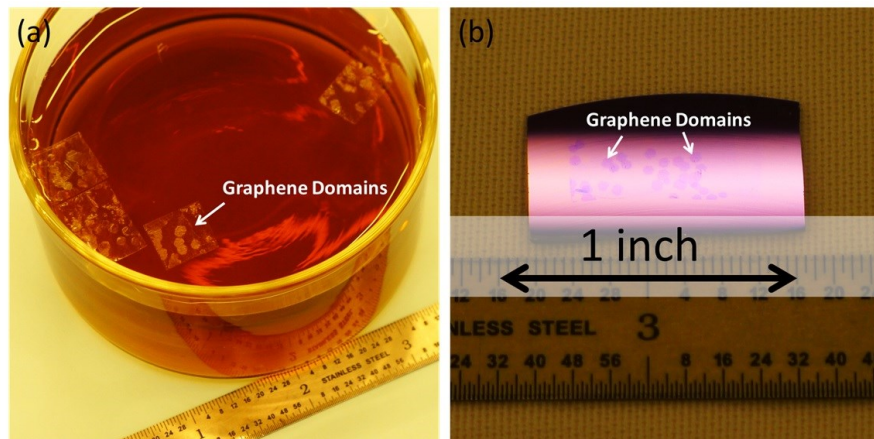


Figure 4.15 Photos of PMMA/graphene membrane floating on $\text{Fe}(\text{NO}_3)_3$ solution (a), and bilayer graphene sample transferred onto SiO_2/Si substrate by artificial stacking (b).

Chapter 5 Raman Spectroscopy Study of Hexagon Graphene Crystals

Raman spectroscopy has long been recognized as a valuable research technique in the years since the phenomenon was first observed by Dr. C. V. Raman in 1928. Due to its sensitivity, high information content, and non-destructive nature, Raman is extensively used in many applications across the fields of chemistry, biology, geology, pharmacology, forensics, pharmaceuticals, materials science, and failure analysis¹⁵¹.

At the initial stage of graphene study, Raman spectroscopy played a canonical role to determine the number of layers and the quality of as-prepared samples^{42, 151, 152}. The profiles of characteristic bands, combination of shapes, intensities and positions, give a considerable amount of information, often comparable to that obtained by competing techniques that are more complicated and destructive. With progresses in synthesizing and functionalizing graphene samples, the understanding of the Raman process in graphene is also matching forward. Raman spectroscopy has been proven surprisingly versatile and capable to evaluate the doping level and chemical functionalization, examine the edge geometry and crystalline orientation, sense the strain and stress, etc¹⁵³⁻¹⁵⁵. The behaviors of phonons contributed to Raman signals, how they move, interfere and scatter, to a large extent rely on electrons behaviors. Thus, any variation of electronic properties can be probe via Raman spectrum.

In the first part of this chapter, the principle of Raman scattering and some basic concepts of solid-state physics will be reviewed as the theoretical foundation for further discussion. Characteristic Raman features of graphene will be introduced. The second part will elaborate the Raman systems applied in this study and other experimental details. The samples prepared in

former chapters will be examined in the rest of this chapter and a comprehensive understanding of Raman signatures and their underlying structural and electronic properties will be established for monolayer hexagon graphene single crystals, bilayer hexagon graphene domains synthesized by CVD method, twisted bilayer graphene domains prepared by artificial stacking, respectively.

5.1 Principle of Raman Spectroscopy

5.1.1 Raman Scattering Effects

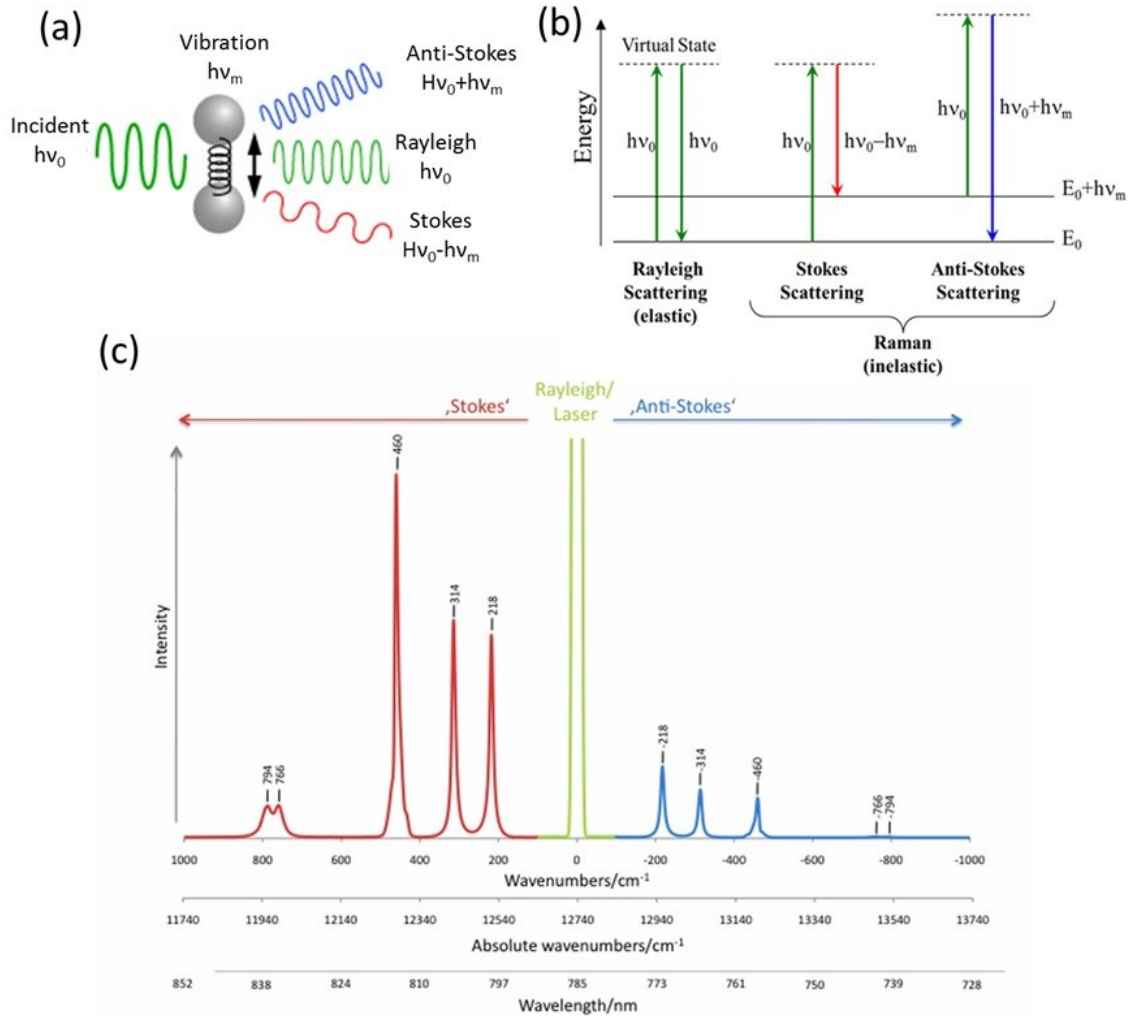


Figure 5.1 Schematic drawings of Rayleigh and Raman scattering from molecule vibration (a), energy level diagram (b), and spectral view (c).

When a sample is irradiated with an intense monochromatic light source (usually a laser), most of the radiation is scattered by the sample at the same wavelength as that of the incoming laser radiation in a process known as Rayleigh scattering (Figure 5.1)¹⁵⁶. However, a small proportion of the incoming light – approximately one photon out of a million – is scattered at a wavelength that is shifted from the original laser wavelength. This phenomenon is Raman scattering, named after the discoverer who was awarded the Nobel Prize in 1930.

As illustrated in the simplified energy level diagram (Figure 5.1 (b)), a molecule at rest resides in the ground vibrational and electronic states. The electric field of the laser beam raises the energy of the system for an instant by inducing a perturbation in the chemical species. The perturbed condition is not (or not necessary) a true energy state and is referred to as a “virtual state”. Relaxation from the virtual state occurs almost instantaneously and is predominantly to the initial ground state. This process results in Rayleigh scatter, which is scattered light of the same wavelength as the excitation laser. Relaxation to the first excited vibrational level results in a Stokes-Raman shift. Stokes-Raman shift scattered light is of lower energy (longer wavelength) than that of the laser light. In addition, most systems have at least a small population of molecules that are initially in an excited vibrational state. When the Raman process initiates from the excited vibrational level, relaxation to the ground state is possible, producing scatter of higher energy (shorter wavelength) than that of the laser light. This type of scattering is called anti-Stokes Raman scattering.

Worth to emphasizing, for regular Raman scattering doesn't involve a stationary state, as shown above. But if the excitation is selected to match a specific energy level, then the process is

resonant, and the intensities are strongly enhanced, as a result of the greater perturbation efficiency.

5.1.2 Raman Spectroscopy

Based on Raman scattering effect, the energy difference between incident and scattered light is extracted and plotted versus corresponding intensity to give a Raman spectrum. Since this energy shift, or so called Raman shift, is nearly negligible compared with incident light energy, the spectra are historically plotted in a very small energy unit, wavenumber (cm^{-1}), approximately equal to 1.24×10^{-4} eV.

For specific molecule, the Raman bands always appear as a set, but not alone, because of the complexity of the vibration states. Thus, no two molecules can give exactly the same Raman spectrum, and the intensity of the scattered light is proportional to the amount of material present. The position and intensity of features in the spectrum reflect the molecular structure and can be used to determine the chemical identity, to characterize the crystalline form of the samples. Noticeably, by comparing the ratios of the intensity of the Stokes and anti-Stokes lines, Raman spectroscopy can also be used to estimate the popularity of molecules in excited state, and serve as a sensitive temperature probe in some circumstance.

For simplicity, throughout this dissertation, we will use the notation I for band height, A for band area or integrated intensity, Pos for band position, FWHM for the full-width at half-maximum and Disp for band dispersion (that is, the rate of shift in band position with changing excitation energy). So, for example, $I(\text{G})$ is the height of the G band, $A(\text{G})$ its area, $\text{FWHM}(\text{G})$ the full-width at half-maximum, $\text{Pos}(\text{G})$ its position and $\text{Disp}(\text{G})$ its dispersion.

5.1.3 Phonon Modes

The measurement of Raman spectrum is relative simple and approachable, which will be discussed in Section 5.2, but it does require data interpretation involving certain solid-state physics knowledge. In order to explain the Raman spectra, a wide-accepted concept in condensed matter, phonon is introduced here.

In Raman scattering process, either Stokes or anti-Stokes, the energy can be considered transferring in form of phonons. Solids with more than one type of atom – either with different masses or bonding strengths – in the smallest unit cell, exhibit two types of phonons: acoustic phonons and optical phonons. Acoustic phonons are coherent movements of atoms of the lattice out of their equilibrium positions; while optical phonons are out-of-phase movement of the atoms in the lattice, one atom moving to the left, and its neighbor to the right. The vibration directions, longitudinal, transverse, and out-of-plane, are often abbreviated as L, T, Z, respectively. And according to the way optical phonons interacting with the light, relevant with strong dipole moments or not, they can be distinguished as infrared active modes or Raman active modes¹⁵⁵.

5.1.4 Raman Modes in Graphene

Grasping the basic concept of Raman spectroscopy and phonon modes, we can start to study the interested case, graphene. The schematic drawing of graphene in reciprocal space is presented here again, but with labelling out the electronic Brillouin zones and first phonon Brillouin zone (Figure 5.2 (a))¹⁵⁴. Former mentioned, there are two atoms in a unit cell of graphene, thus there are six vibration modes (Figure 5.2 (b)). Along the high symmetry Γ -M and Γ -K directions, the six phonon dispersion curves are assigned to LO, TO, ZO, LA, TA, and ZA

phonon modes, respectively (Figure 5.2 (c))¹⁵⁵. At the zone center, TO and LO modes, the vibrations of the sublattice A against the sublattice B, are degenerate. According to Group Theory, these two modes from E_{2g} representation, therefore, they are Raman active.

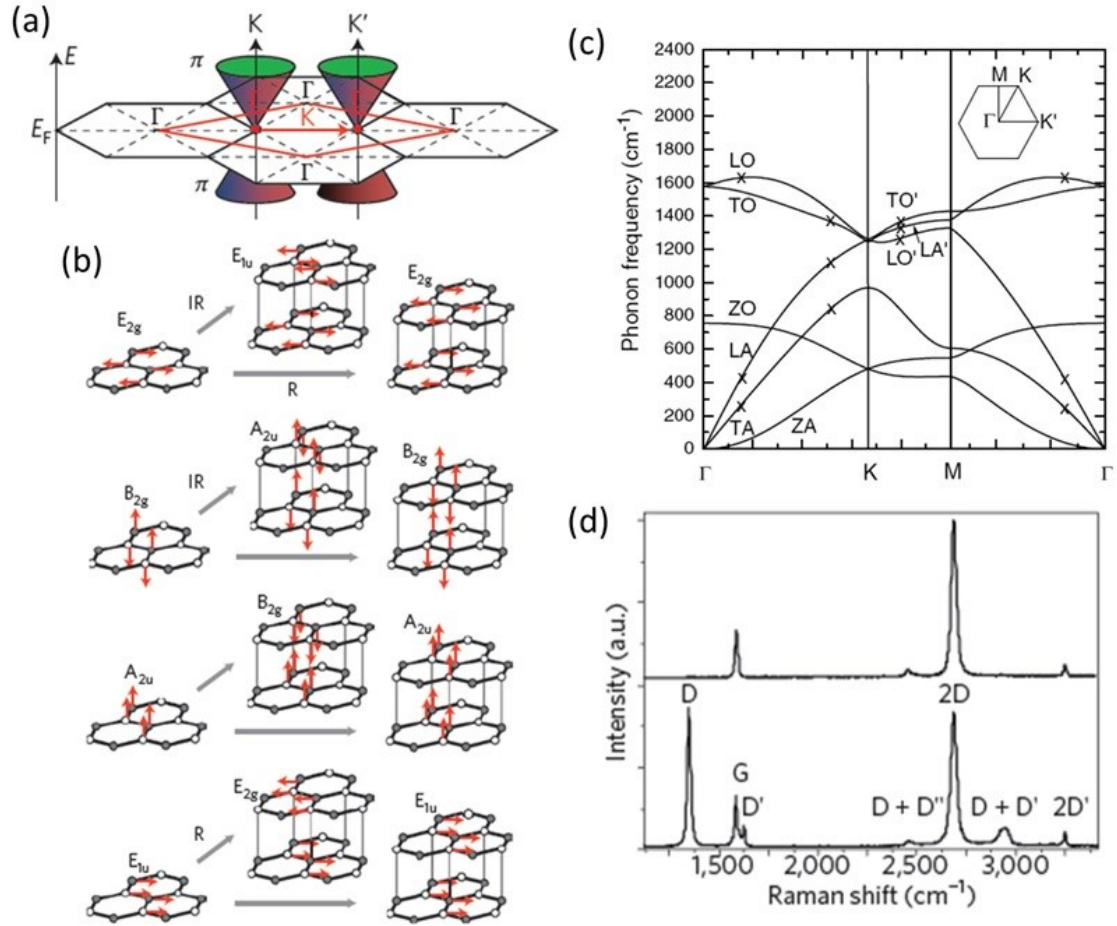


Figure 5.2 (a) Schematic drawings of electronic and first-phonon Brillouin zones of graphene, and electronic dispersion. (b) Γ -point phonon-displacement patterns. (c) Phonon dispersion curve. (d) Raman spectra of pristine (top) and defected (bottom) graphene.

A typical Raman spectrum of monolayer graphene is provided in Figure 5.2 (d) (top). Two most distinct bands at $\sim 1580 \text{ cm}^{-1}$ and $\sim 2700 \text{ cm}^{-1}$ are named as G band and 2D (or G') band, respectively. The former is associated with the aforementioned degenerate phonon modes (TO

and LO) at Γ point, which is the only band coming from a normal first order Raman scattering process in graphene (Figure 5.3)⁴². The latter originates from a second-order process, involving two TO phonons near the K point. After breaking the perfect planar lattice, a couple of disorder-induced second-order bands appear in the Raman spectrum (Figure 5.2 (d) (bottom)). The most significant one, D band at $\sim 1350 \text{ cm}^{-1}$ is the breathing modes of six-atom rings, originating from TO phonons around the Brillouin zone corner K, and requires a defect for activating. It is an intervalley double resonance process, because it connects points in circles around inequivalent K and K' points in the first Brillouin zone of graphene. And if it is an intravalley process, that is, connecting two points belonging to the same cone around K (or K'), this gives the so-called D' band, at $\sim 1620 \text{ cm}^{-1}$.

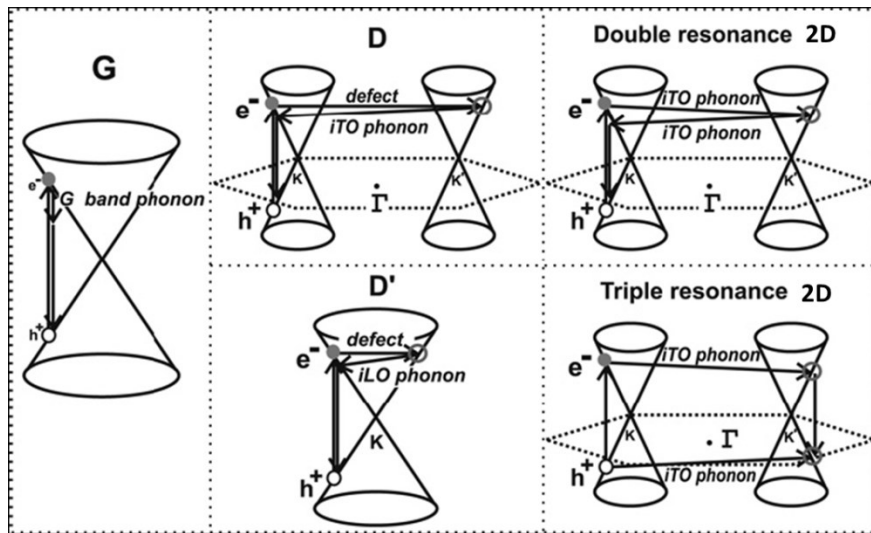


Figure 5.3 Schematic drawings of first-order G band process, second-order process for the D band (intervalley process), the D'band (intravalley process), and 2D band.

It is noticeable the second-order band at $\sim 2700 \text{ cm}^{-1}$ is assigned as “2D” band, because it is also an intervalley double resonance process and its frequency is approximately twice the

frequency of D band. Nevertheless, 2D band is allowed in the second-order Raman spectra of graphene without any kind of disorder or defects. Due to the intervalley mechanism, D and 2D band show strongly dispersive behavior with excitation laser energy. The wavevectors q of the phonons would couple preferentially to the electronic states with wavevectors κ , such that $q \approx 2\kappa$.

When the number of graphene layer increases, not only the in-plane vibrations, such as D, G, 2D, and so on, but also the shear (C) modes and the layer-breathing modes (LBMs), due to relative motions of the planes themselves, either perpendicular or parallel to their normal, will present in the Raman spectrum. These out-plane modes directly depend the number of layers N and can serve as the probe of N ; however, they usually appear in the low frequency range of spectra, below the notch and edge filter cut-off of many spectrometers, and hardly detectable.

Upon above discussion, it is imaginable how complex the Raman spectra of graphene can be. It is presumed that up to six-phonons process can be measured in graphene. However, the Raman spectra in most literature reports display from $\sim 300 \text{ cm}^{-1}$ to $\sim 3,300 \text{ cm}^{-1}$. This restricts our attention to one- and two-phonon bands. Necessary calculation and deeper theoretical explanation will be provided to analyze some specific Raman features below.

5.1.5 Rules of Thumb

Again, the richness of phenomena and the volume of information comprised in Raman spectrum somehow make it challenging to decipher. Seemingly, graphene is the simplest 2D mode. But its peculiar electronic band structure, the strong electron-phonon, and electron-electron interactions complicate the interpretation even more. After decades of study (yes, far prior to the isolation of graphene), some theoretical predictions and experimental results, which can provide

invaluable insight to understand the Raman behaviors and shed light on the underlying electronic properties, are summarized here.

Table 5.1 Experimental Rules of G band and 2D band.

G Band				
	Position	FWHM	Intensity	Shape
Number of layers	Red shift with increased layers ($\text{PosG}(n)=\text{PosG}(\infty)+\beta/n$, where $\beta \approx 5.5 \text{ cm}^{-1}$ is a constant, n is the number of layer) (For intrinsic monolayer $\sim 1582 \text{ cm}^{-1}$)	Constant	Linear increasing with increased layers (For Bernal stacking, number of layer $n < 19$)	Single Lorentzian
Doping concentration	Blue shift with both electron and hole doping	Narrow	Constant	Single Lorentzian
Temperature dependence	Red shift with increasing temperature	Not sensitive	Constant	Single Lorentzian
Uniaxial strain	Blue shift with compressed strain	Not sensitive	Constant	Single Lorentzian
Biaxial strain	Blue shift with compressed strain	Not sensitive	Constant	Single Lorentzian
Dispersion with excitation laser energy	Non-dispersive	—	—	—
2D Band				
	Position	FWHM	Intensity	A(2D)/A(G)
Number of layers	Splitting to some components with increased layers (For Bernal stacking)	Bigger for bilayer than single layer	Not sensitive (For Bernal stacking)	Decreasing with increased layers (For Bernal stacking, number of layer $n < 19$)
Doping concentration	Blue shift with hole doping and red shift with electron doping	Narrow	Decreasing with increased electron concentration	Decreasing with increased electron concentration
Temperature dependence	Red shift with increasing temperature	Not sensitive	Constant	—
Uniaxial strain	Blue shift with compressed strain	Not sensitive	Constant	—
Biaxial strain	Blue shift with compressed strain	Not sensitive	Constant	—
Dispersion with excitation laser energy	Dispersive (With a slope of $\Delta\text{Pos}(2D)/\Delta E_{\text{laser}}$ is about $100 \text{ cm}^{-1}/\text{eV}$)	—	—	—

- (1) Number of graphene layers: For Bernal stacking graphene, the intensity of the G band increases in an almost linear relation with increased layers which can be easily understood as more sp^2 bond carbon atoms being detected by the laser spot with increased layers of graphene. The position of G band also tends to shift downwards. But it is hard to rule out the doping or strain effects which also lead to shift in G band position. Due to the sensitivity to electronic band structure, double resonance band, D and 2D, undergo an evolution in the shape and intensity. From single-layer graphene (SLG) to bilayer layer graphene (BLG), the electron band divide in four, with a different splitting for e and h. This band splitting is responsible for the arising of four branches of 2D band, $2D_{11}$, $2D_{12}$, $2D_{22}$, $2D_{21}$.
- (2) Defects and disorder: When the sp^2 carbon structures are being destroyed gradually, the Raman spectrum evolves as follows: (a) a D band appears and $I(D)/I(G)$ increases; (b) a D' band appears; (c) all bands broaden, so that the D and 2D bands lose their doublet structure in graphite; (d) the $D + D'$ band appears; (e) the G and D' bands are so wide that it is sometimes more convenient to consider them as a single, upshifted, wide G band at $\sim 1,600 \text{ cm}^{-1}$.
- (3) Edge: Edges can be viewed as extended defects, breaking the symmetry, even though a perfect zigzag or armchair edge still preserves the translation symmetry along the edge. Due to translational invariance along the edge, a perfect zigzag edge cannot scatter electrons between the K and K' valleys, hereby prohibit the D band process. Therefore, D band intensity along armchair edges is more profound than the zigzag ones. But this

does not apply to the intravalley process of D' band, which can be activated both by armchair and zigzag edges.

(4) Doping: Doping can also introduce defects, but more profoundly change the Fermi level (E_F) of graphene. Doping changes occupations of electronic state and, since transitions from an empty state or to a filled state are impossible; it can effectively exclude some regions of k from contribution to the Raman matrix element. The intensity of 2D band drops when E_F moves away from the Dirac point, and it is even suppressed when the conduction band becomes filled at the energy probed by the laser. And G band also exhibits E_F dependent, especially at a high doping level. Remember the samples prepared by PMMA-assistant wet transfer method are unintentionally doped by holes.

5.2 Experimental Details of Raman Measurement

5.2.1 Overview of Dispersive Raman Microscopy

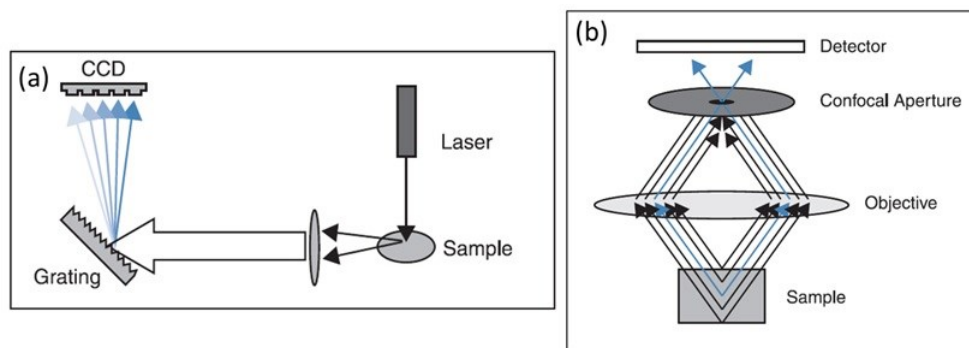


Figure 5.4 Schematic drawings of dispersive Raman spectroscopy (a) and confocal setup (b).

Prior to the measurement, it is crucial to understand the working principle of the Raman systems. Typically, Raman spectrometers are based on one of two technologies: dispersive Raman

and Fourier transform Raman. Only the former will be introduced here, since all of the four systems applied in this study are dispersive Raman systems.

To observe the Raman spectrum, it is necessary to separate the collected Raman scattered light into its composite wavelengths. In dispersive Raman instruments, this is accomplished by focusing the Raman scattered light onto a diffraction grating, which splits the beam into its constituent wavelengths. And these monochromatic lights are directed onto a charge-coupled device (CCD) (Figure 5.4 (a)). Accompanying with microscope objectives and confocal techniques, a modern Raman microscope can achieve sub-micron spatial resolution (Figure 5.4 (b)).

For regular Raman scattering, excluding the resonance cases, the Raman shift is non-dispersive with the excitation laser energy. Therefore, laser sources with various wavelengths, such as 780 nm, 633 nm, 532 nm, and 473 nm, can be employed in the dispersive Raman systems. Generally speaking, the intensity of the Raman scattering is proportional to $1/\lambda^4$, so short excitation laser wavelengths deliver a much stronger Raman signal. Also short excitation laser wavelengths can provide a better spatial resolution, which is proportional to diffraction limitation. But on the other hand, fluorescence is much more likely to occur with higher excitation laser energy. Previously stated, Raman scattering is not a high-probability process, of which the cross section for a molecule is about 10^6 and 10^{14} times smaller than those of fluorescent process. Strong fluorescence intends to saturate the CCD and make Raman measurements impossible. These impacts should be balanced to choose suitable excitation laser energy for measurement.

Spectral resolution of a Raman system is mainly determined by the resolution of grating and CCD. Usually, a grating with higher resolution contains more lines in a prescribed area, which leads to a smaller scanning window. During the acquisition of spectrum, the spectrometer needs to rotate the grating and take several windows to fulfill a wide range scanning, which is time-consuming. For a confocal setup, the spectral resolution is also confined by the magnification of objective and the size of aperture. Higher magnification and smaller aperture is preferential to gain a higher resolution. These basic understandings are helpful to design the setup and operation protocol in the following study.

5.2.2 Operation of Commercial Raman Microscopes



Figure 5.5 Commercial Raman system applied in this study.

There are two commercial Raman microscopes employed in this study: XploRA One (Horiba) and T64000 (Horiba) (Figure 5.5). Both systems are equipped with a 10 \times and a 100 \times objective with a similar spatial resolution of 1 μm \times 1 μm . And automatic XYZ stages enable the function of Raman mapping. The XploRA One is a compact system assembled with two laser lines at 638 nm (1.94 eV) and 532 nm (2.33 eV), and an air-cooled CCD for detection. It is

suitable for fast scanning. While, T64000 is a more sophisticated and versatile platform adapted with a liquid-nitrogen-cooled CCD and multiple laser lines, but only three of them, 514 nm (2.41 eV), 488 nm (2.54 eV) and 458 nm (2.71 eV), are utilized in this study. With the kit of polarizer and analyzer, it can measure polarization dependent Raman spectrum.

With both systems, the measurement is performed at a relatively low laser intensity, less than 2mW, to suppress the heating effects. A grating with modest density of lines is chosen upon the excitation laser energy and the aperture and slit are set at the minimum value to obtain a spectral resolution of $\sim 1\text{cm}^{-1}$. Multiple cycles of scanning are preferred to improve the signal-to-noise ratio. Without specification, the mappings and spectra discussed in this dissertation were fulfilled by the XploRA, with 532 nm laser excitation and 100 \times objective.

5.2.3 Setups and Operation of Lab-Built Raman Systems

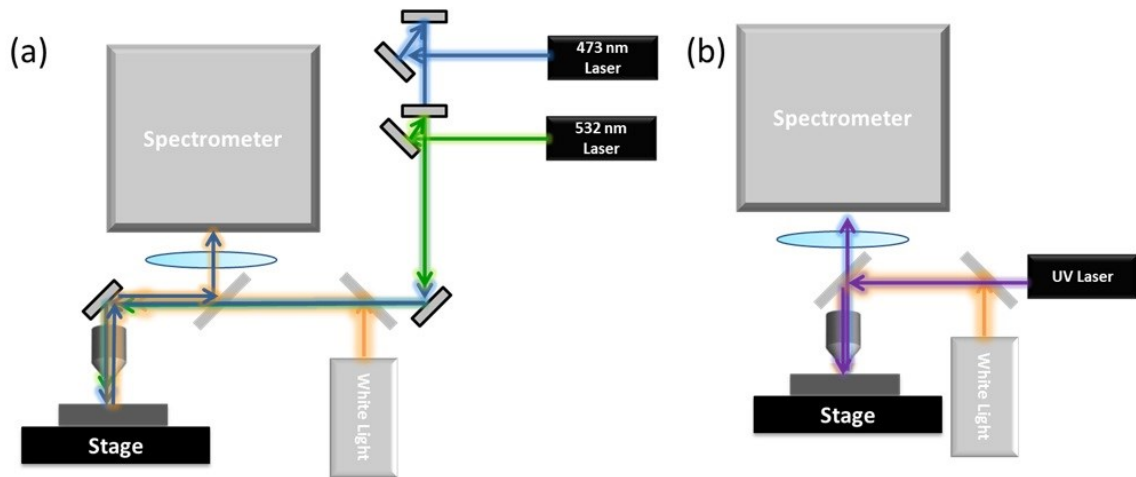


Figure 5.6 Configurations of the lab-built micro-Raman systems with visible laser sources (a) and ultraviolet (UV) laser (b).

Besides the commercial systems, two micro-Raman systems with different configurations are specifically designed and built for this study. As shown in Figure 5.6, the system with two

visible laser sources, at 473 nm (2.62 eV) and 532 nm (2.33 eV), is equipped with a three-grating iHR550 imaging spectrometer (Horiba). Different from commercial systems, the lab-built one is more flexible and is capable to fulfill not only Raman, but also luminescence, and reflection spectrum measurement.

As mentioned, ultraviolet laser is not frequently as the choice of the excitation laser source for Raman measurement. Not only because it may induce undesired luminescence process, but also because UV laser with adequate power to excite Raman scattering is not common. Here, an Ar laser (Spectra-Physics), with maximum output of ~ 100 mW at wavelength of 363.8 nm (3.41 eV) has demonstrated its capability in Raman measurement, with assistant of iHR 320 spectrometer (Horiba). A compact configuration is adapted to eliminate the possible scattering and emissions from optical components and also to collect more portion of effective scattering from the sample. It should be mentioned, the high power density of focus UV laser incline to damage the atomic thin graphene layers. Therefore, the minimum output, ~ 30 mW, is actually applied for measurement.

5.2.4 Spectrum Analysis

In order to compare the spectra obtained from different systems, a certain spectrum analysis is required. Without specific notice, all the spectra present in this dissertation are calibrated with the first order Si band at 520 cm^{-1} , which is non-dispersive with excitation laser energy. After manually subtracted the baseline, the spectra are also normalized with the intensity of 520 cm^{-1} Si band, when comparison of intensity is demanded.

5.3 Raman Spectroscopy Study of Monolayer Hexagon Graphene Crystals

There are two catalogs of monolayer layer hexagon graphene crystals prepared in this study, H₂-rich and O₂-rich. As demonstrated in Chapter 4, both of them distinct single-layer Raman features with negligible defect bands. A closer examination will be carried out here.

5.3.1 Uniformity

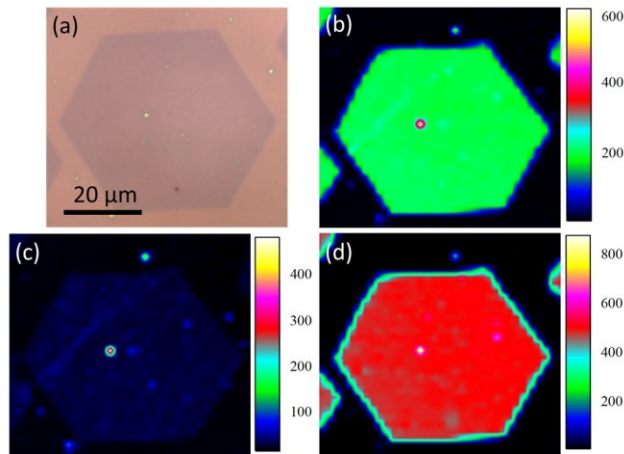


Figure 5.7 Optical microscope image of a H₂-rich monolayer graphene hexagon (a) and its corresponding Raman mappings of G band, D band, and 2D band (c-d).

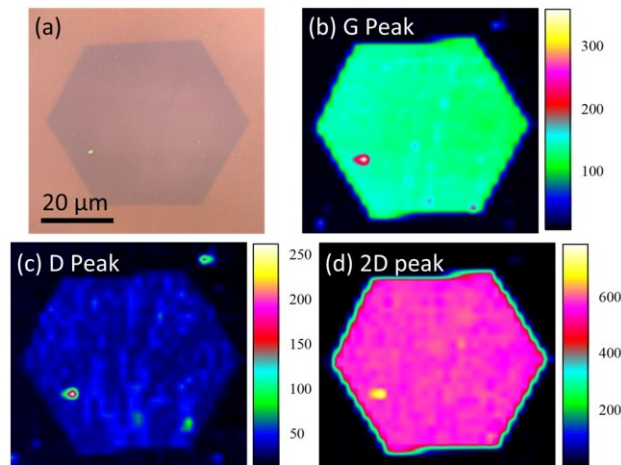


Figure 5.8 Optical microscope image of another H₂-rich monolayer graphene hexagon on the same sample (a) and its corresponding Raman mapping of G band, D band, and 2D band (c-d).

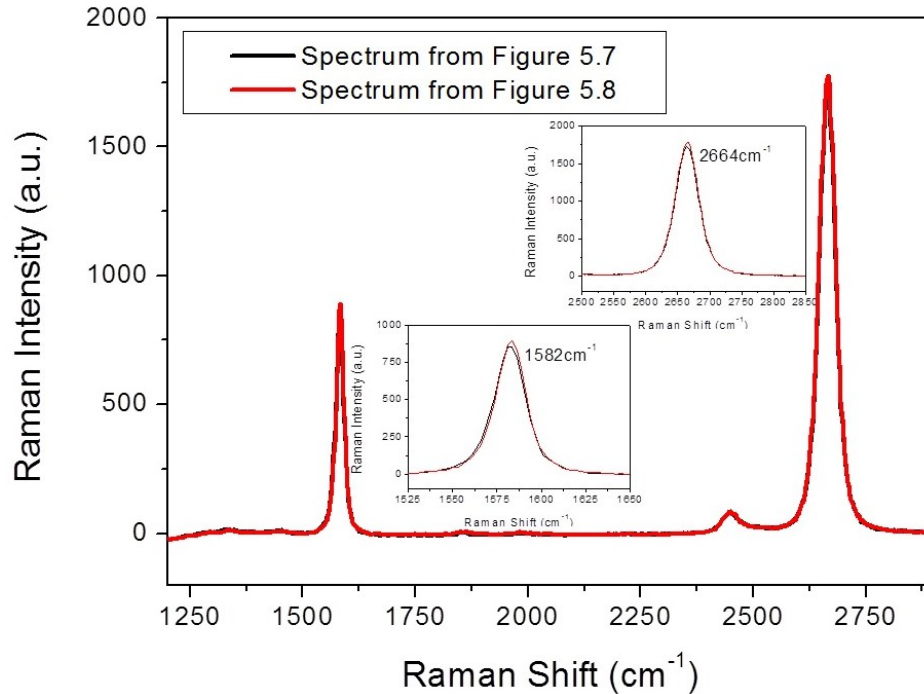


Figure 5.9 Spectra from point measurement of domains in Figure 5.7 and 5.8, respectively.

Compared with sophisticated energy spectrum measurement, such as scanning tunneling microscope (STM) and angle resolved photoemission spectroscopy (ARPES), of which the working area is quite limited, Raman has superiority in characterizing the samples in a large scale. Especially, the Raman mapping can provide a straightforward image of the uniformity of the sample. Two sets of Raman mapping are obtained from different domains on a same H₂-rich sample. As displayed in Figure 5.7 ~ 5.8, both monolayer graphene hexagons possess identical Raman features over hundreds of micrometer areas, except for one or two minus points which is suspected as the nucleation centers. The regular steps along the edges in the mapping reflect the interval of scanning mesh, which is around 2.5 μm for these two figures. A slightly low intensity at the edges comes from the mapping mechanism, which average the signal collected between each interval. Also from the color contrast, the I(D)/I(G) and I(2D)/I(G) ratio can be roughly

estimated. But it should be point out that the individual mapping for each band are plotted in different intensity scale. The mapping results in Figure 5.7 & 5.8 not only indicated the uniformity of single domain, but also show the equivalent quality of domains synthesized in the same batch, which is further revealed by the point spectra measurement (Figure 5.9). With acceptable deviation in intensity, no obvious shift in band position has been detected.

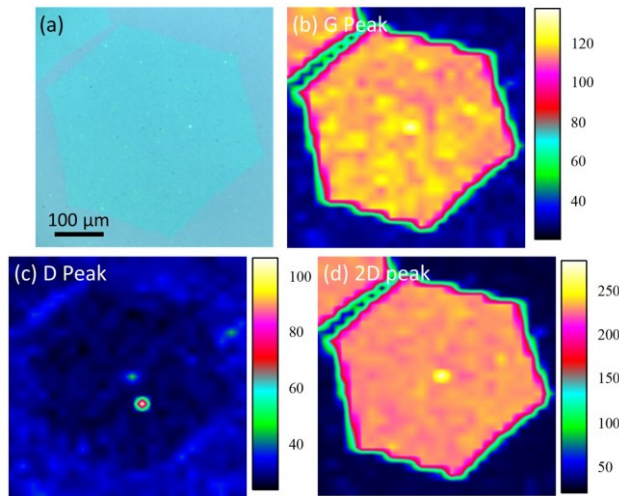


Figure 5.10 Optical microscope image and Raman mappings of a H₂-rich graphene hexagon.

Similarly, the uniformity of O₂-rich samples has also been verified. But the steps along the edges appear more obvious, because a much larger mesh interval, ~20 μm, is applied. The comparison between H₂-rich and O₂-rich samples has been made in Chapter 4, which shows a 2~3 cm⁻¹ shift in G and 2D band position but quite comparable I(2D)/I(G) ratio.

Above results demonstrate the reliability in quality of as-prepared hexagon graphene single crystals, no matter which synthesis recipe is applied and how large it expands in dimensions. The uniformity and consistence of Raman profile is critical to discover and evaluate the anomalous behavior which will be discussed in Section 5.4.

5.3.2 Defects, Edges and Boundaries

Taking a closer look at the mapping and spectra provided in Section 5.3.1, we can clearly identify the characteristic bands G, G* (or D+D’’, at $\sim 2450\text{ cm}^{-1}$), and 2D. While the defect-related D band is negligible, which suggests little amount of defects in as-prepared graphene domains. To further quantify, the intensity ratio of D band to G band $A(D)/A(G)$, varied inversely with the crystal size^{157, 158}, is determined as small as 0.08. And as the most unique Raman signature of single-layer graphene, the intensity of 2D band is much larger than the value of G band, over 4 times, under 532 nm laser excitation. This large relative intensity of the 2D band, understood in terms of a triple resonance process involving the linear electron dispersion⁴², also authenticates the highly crystalline sp^2 carbon lattices.

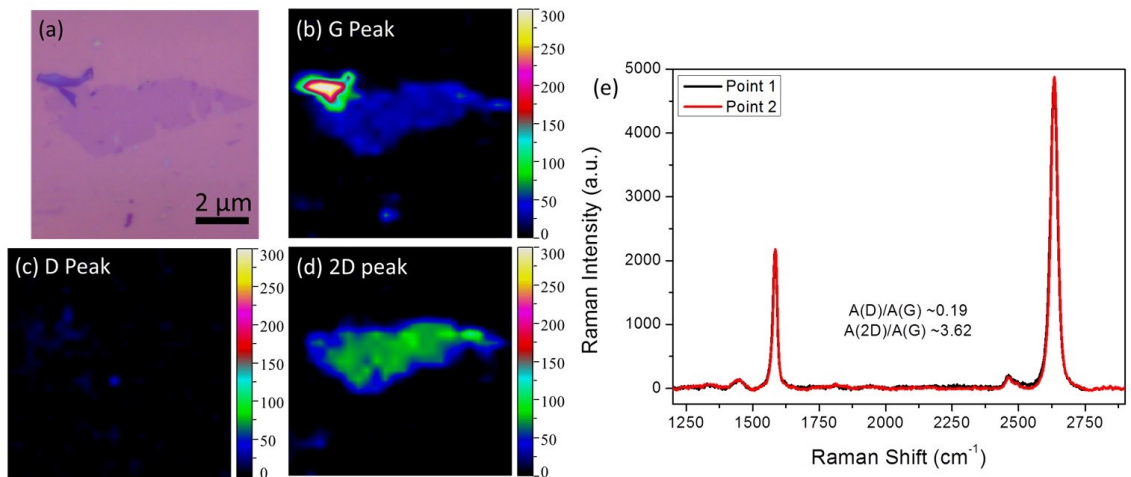


Figure 5.11 Optical microscope image (a), Raman mapping (c-d), and spectra from two point measurements (e) of single-layer graphene flake prepared by mechanical exfoliation.

For comparison, single-layer flakes, mechanically exfoliated from high ordered pyrolytic graphite (HOPG), were also examined here. Based on the spectra in Figure 5.11, the intensity ratio of $A(D)/A(G)$ and $A(2D)/A(G)$ are given as 0.18 and 3.62, respectively. These results all

strongly imply the superior quality of monolayer graphene crystals synthesized by CVD method in this study.

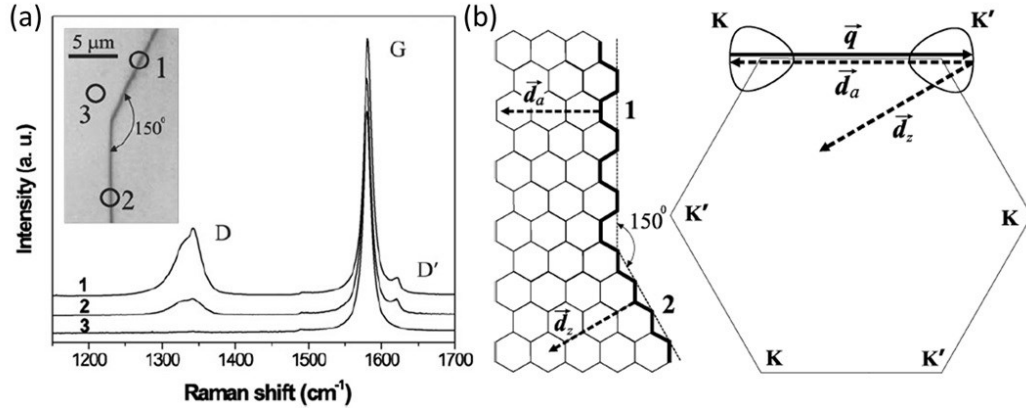


Figure 5.12 (a) Raman spectra obtained in three different regions of a HOPG sample, with excitation laser of 638 nm. (b) Schematic illustration of the atomic structure of the armchair and zigzag edges and first BZ of 2D graphite.

From mapping results in Section 5.3.1, the absence of D band is not only observed at the center of these single crystal domains but also at the edges. It is reasonable to presume an edge may expose larger amount of defects, due to the break of perfect hexagonal rings. However, the theoretical studies and previous experimental results of graphite revealed that different symmetry possessed by armchair and zigzag edges gives rise to difference in D intensity, which allows Raman spectroscopy to distinguish between these edges¹⁵⁷. Typical armchair and zigzag edges are illustrated as edge 1 and edge 2 in Figure 5.12 (b). Geometrically, it is easy to deduce that the intersection angle between an armchair and a zigzag edge should be a multiple of 30°⁴². Figure 5.12 (a) shows the Raman spectra from three different locations on such a HOPG sample, where it is possible to clearly recognize those edges that have a 150° between them¹⁵⁹. For edge 2, identified as a zigzag edge by STM, the D band is less significant with respect to that for the

armchair one. As indicated in Figure 5.3, D band originates from a double resonance process between two adjacent K and K' points. The zigzag defect wavevector (d_z) is incapable to connect the K and K' points, and thus the elastic electron scattering by the defect does not have enough momentum to span from points K to K' and satisfy the conservation of momentum in a Raman experiment performed with visible light. Therefore, D band is usually undetectable for a perfect zigzag edge, as shown in our case. This supports the hypothesis that zigzag edge is the energetic favorable termination of APCVD grown graphene hexagons with H₂ as co-catalyst^{126, 160}.

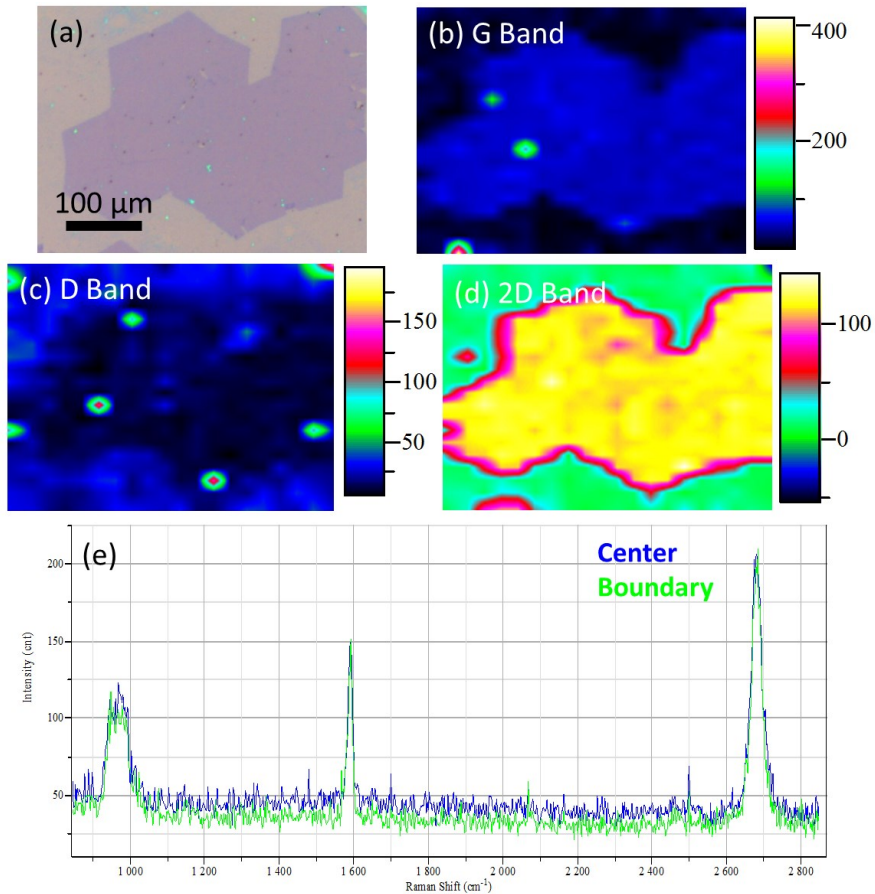


Figure 5.13 Optical microscope image (a) and corresponding Raman mapping (b-d) of merged H₂-rich hexagons with parallel edges. (e) Spectra measurement from center of domain (blue) and the boundary between domains (green).

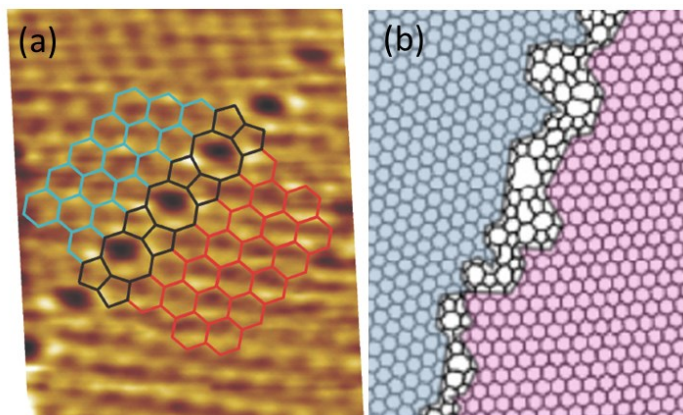


Figure 5.14 Examples of ordered (a) and disordered (b) grain boundaries.

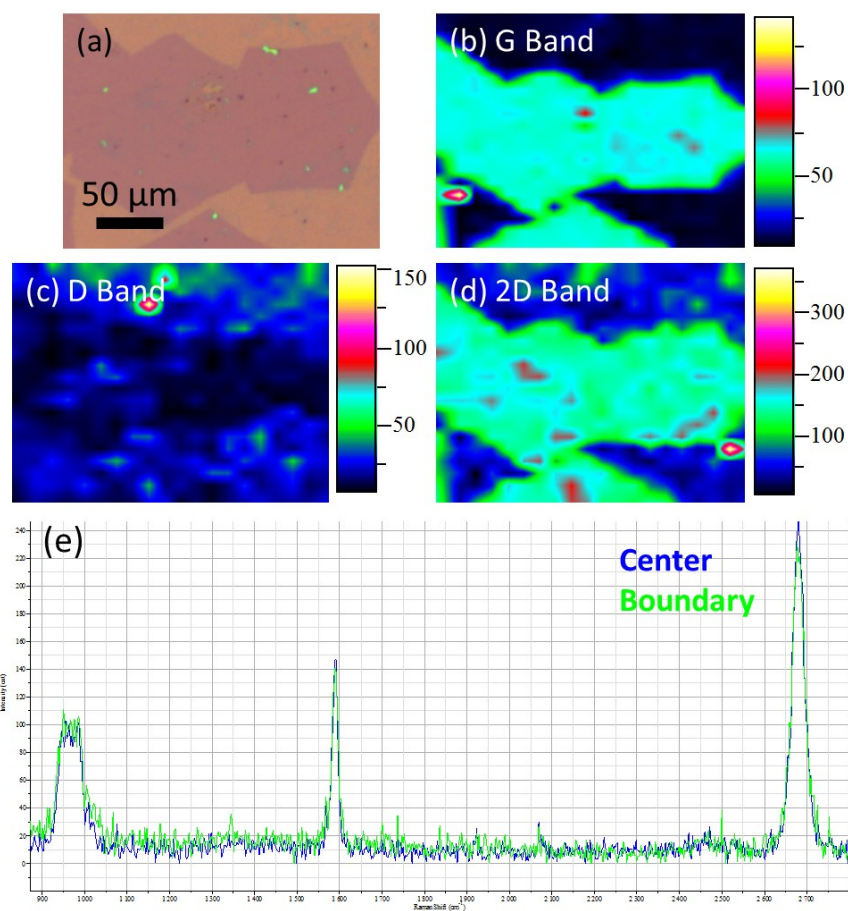


Figure 5.15 Optical microscope image (a) and corresponding Raman mapping (b-d) of other merged H₂-rich hexagons with rotated edges. (e) Spectra measurement from center of domain (blue) and the boundary between domains (green).

Besides, grain boundary effect can be also evaluated by Raman mapping. The set of domains in Figure 5.13 have nearly parallel edges, indicating analogous crystal orientations. Therefore, when two domains adjoin, they intend to be stitched with ordered boundaries, as suggested in Figure 5.14 (a)¹⁶¹. In contrast, if the neighbor domains aligned along different directions, it is more likely to form disordered boundary as shown in Figure 5.14 (b)¹⁰⁹. Surprisingly, no notable D band emerges even when the two adjacent domains retaining a large rotation angle, in most cases studied here (Figure 5.13 and 5.15). However, a relative low spatial resolution could be an understandable explanation for this deviate observation¹⁶⁰.

5.3.3 Dispersive Behaviors

As pointed out in Section 5.2.2, the mapping and spectra studied above were measured with excitation of 532 nm laser. In fact, the Raman features of monolayer graphene domains have been systematically investigated with varied excitation laser, from UV to near IR. Generally, the Raman shifts, originating from the intrinsic vibration of crystal lattices or molecules, should be independent on the excitation laser energy. But when an electron state involved, the Raman process could behave dispersive. Thanks to the peculiar electron band structure and strong electron-phonon interaction, resonance Raman processes have been widely witnessed on graphene, like previously mentioned D band and 2D band.

In order to visualize the dispersive Raman features, the spectra provided in Figure 5.16 were normalized with the non-dispersive G band. Since the extremely low density of defects in as-prepared samples, the evolution of D band is nearly untraceable. But learning from reported results of graphite, we acquire that the position of D band $\text{Pos}(D)$ upshifts with increasing laser

energy E_{Laser} in a linear way over a wide range, the slope of $\Delta\text{Pos}(D)/E_{\text{Laser}}$ being about $50 \text{ cm}^{-1}/\text{eV}$ (Figure 5.17 (a))¹⁵⁷. As the overtone, 2D band is expected to behave analogously, but with $\text{Disp}(2D)$ of $\sim 100 \text{ cm}^{-1}/\text{eV}$, which is well demonstrated in Figure 5.16 and Figure 5.17 (b). It should be noticed that as a first order Raman feature, although G band position is not dispersive, the intensity of G band should be proportional to E_{Laser}^4 ¹⁵⁸. While, the integrated area of second order bands, D and 2D, are predicted less dependent on E_{Laser} . Fully quantitative understanding and the actual measurements, however, are not trivial. As demonstrated in Chapter 4, graphene samples are routinely transferred onto SiO_2/Si substrate in order to exploit the interference and multi-reflection inside capping SiO_2 layer to enhance the optical visibility of graphene. This interference enhancement also could not be overlooked when interpreting the Raman intensity, especially with visible laser excitation¹⁶². Therefore, the decrease in $A(2D)/A(G)$ is only observable during the altering of excitation laser from 363 nm to 458 nm in Figure 5.16.

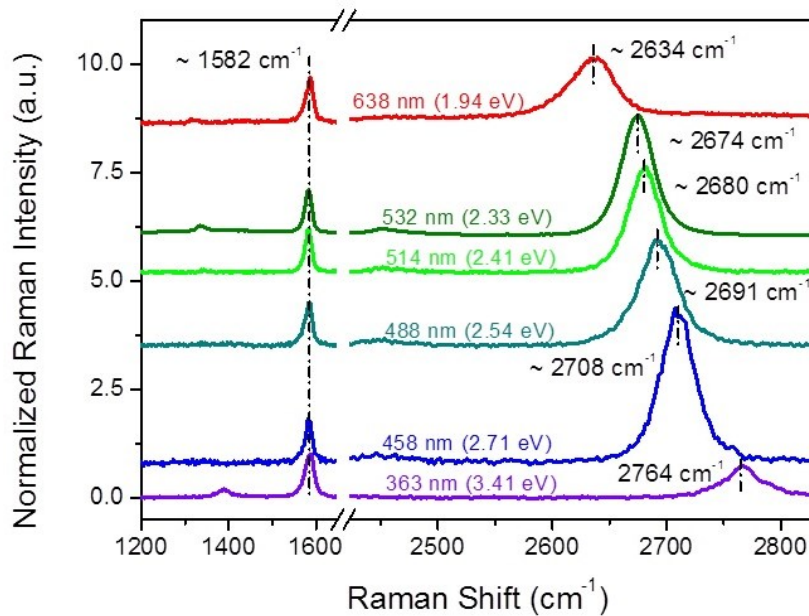


Figure 5.16 Raman spectra of a monolayer domain under different laser excitation.

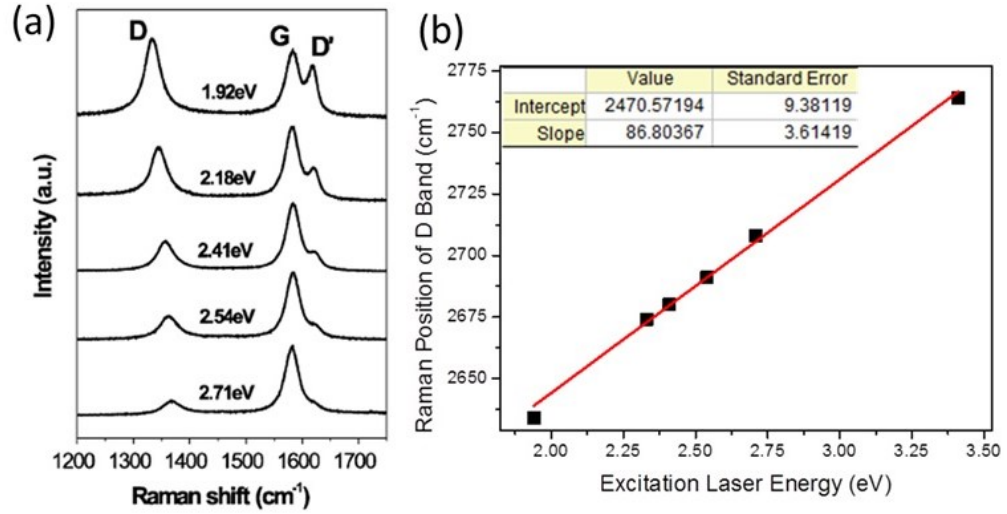


Figure 5.17 (a) Raman spectra of nanographites for five different laser energy values. (b) Plot of Raman position of 2D band versus excitation laser energy, based on spectra in Figure 5.16.

5.3.4 Summary

As a summary, the key parameters of each characteristic Raman peak for monolayer hexagon graphene crystals and exfoliated flakes are listed in Table 5.2. These results serve as the standard for later discussion of bilayer domains.

Table 5.2 Characteristic Raman peaks for monolayer graphene with 532 nm laser excitation.

	Position	FWHM	Shape	A/A(G) Ratio
Monolayer hexagon domains synthesized by CVD				
D Band	—	—	—	Less than 0.08
G Band	$1582.49 \pm 1.27 \text{ cm}^{-1}$	$20.47 \pm 0.53 \text{ cm}^{-1}$	Single Lorentz	—
2D Band	$2665.75 \pm 1.27 \text{ cm}^{-1}$	$43.74 \pm 0.18 \text{ cm}^{-1}$	Single Lorentz	4.20 ± 0.25
Monolayer flakes prepared by mechanical exfoliation				
D Band	—	—	—	Less than 0.19
G Band	$1580.31 \pm 1.34 \text{ cm}^{-1}$	$12.69 \pm 0.65 \text{ cm}^{-1}$	Single Lorentz	—
2D Band	$2667.24 \pm 1.14 \text{ cm}^{-1}$	$27.57 \pm 0.18 \text{ cm}^{-1}$	Single Lorentz	3.97 ± 0.37

5.4 Raman Spectroscopy Study of Bilayer Hexagon Graphene Domains Synthesized by CVD

5.4.1 Overview

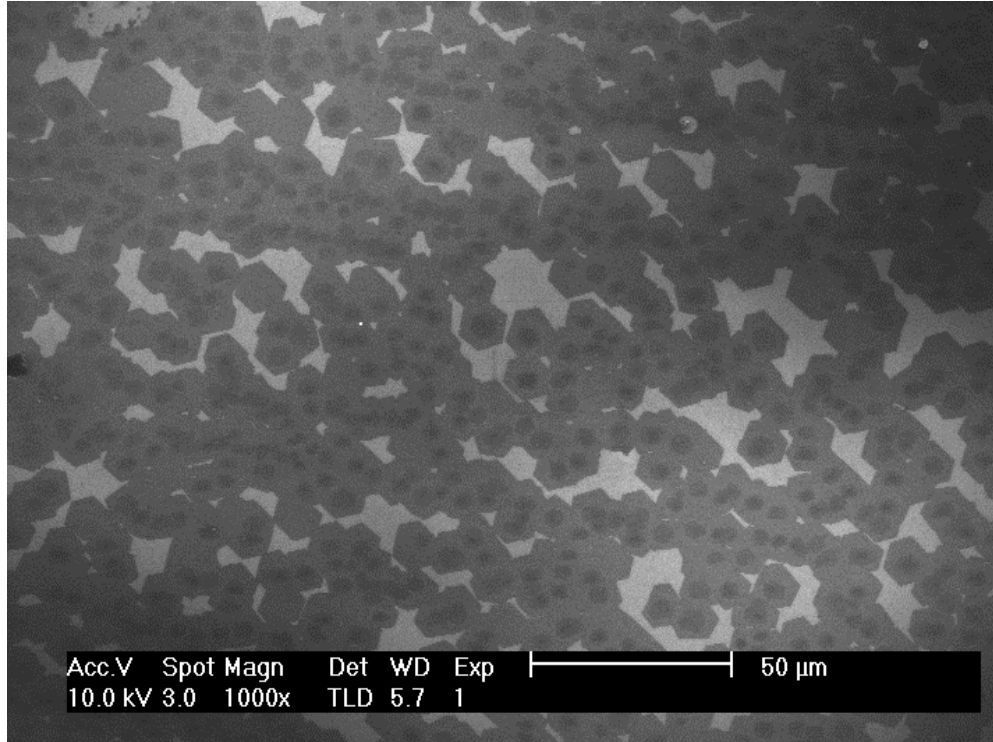


Figure 5.18 A typical SEM image of CVD synthesized bilayer graphene domains.

The CVD synthesized bilayer grains have two stacked hexagonal layers, with smaller and darker regions as the bilayer parts in SEM image (Figure 5.18). The domains seemingly align along certain directions, but varied rotation angles can be discovered (Figure 5.19 (b)). As stated before, one of the outstanding advantage of bilayer hexagon domains is the relative rotation between the two hexagons can be directly used to estimate the actual crystallographic orientation in the bilayers, due to their well-defined zigzag edges. The statistics of the rotation angle distribution over 100 domains is shown in Figure 19 (a). The graphene bilayers are more likely

(up to 15%) to possess parallel arrangement (0°) to achieve the lowest energy state. There is also a slight preference of 29° rotated bilayer graphene, although for the rotated graphene multilayers, 27.8° rotation angle has been calculated as a relatively low energy configuration. In addition, the bilayers with rotation angles between 0° and 30° can also be frequently observed, suggesting no strong confinement effect from the growth substrate on crystallographic orientation of the two layers of bilayer graphene. This agrees with the finding that the interaction between CVD graphene and the underlying polycrystalline Cu substrate is relatively weak compared to other graphene-metal systems¹⁵⁰.

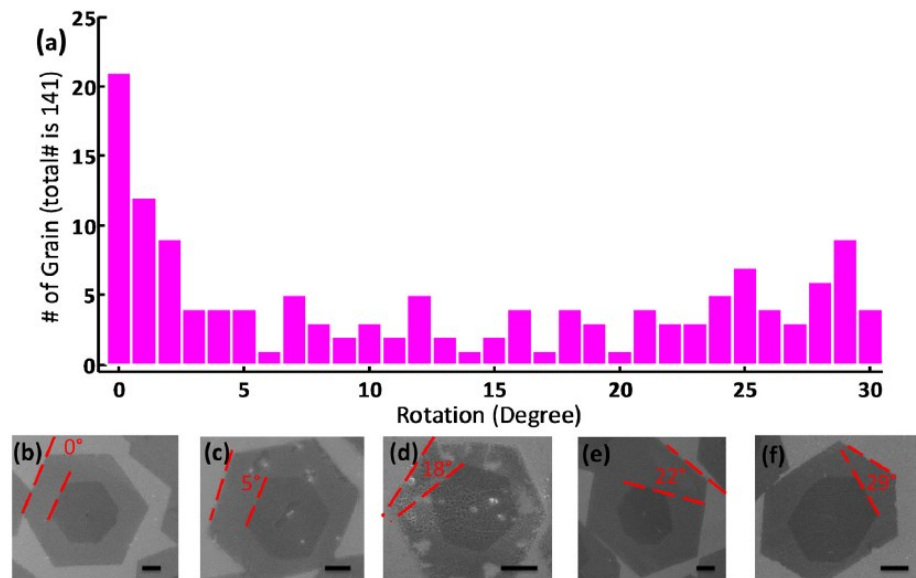


Figure 5.19 (a) Distribution results from the SEM measurements of over 100 graphene bilayer domains. (b-f) SEM images of typical individual bilayer domains on Cu foil with various rotation angles. The scale bars are 2 μm .

5.4.2 Raman features of Bernal Stacked Bilayer Graphene

As introduced in Chapter 2, we can roughly classify bilayer graphene samples into two categories, Bernal stacked and twisted. Due to the divergence in crystalline structures, these two

categories are endowed with distinguishable electron band structures, and consequently distinguishable Raman behaviors. The Bernal and quasi-Bernal stacked cases will be viewed in this section.

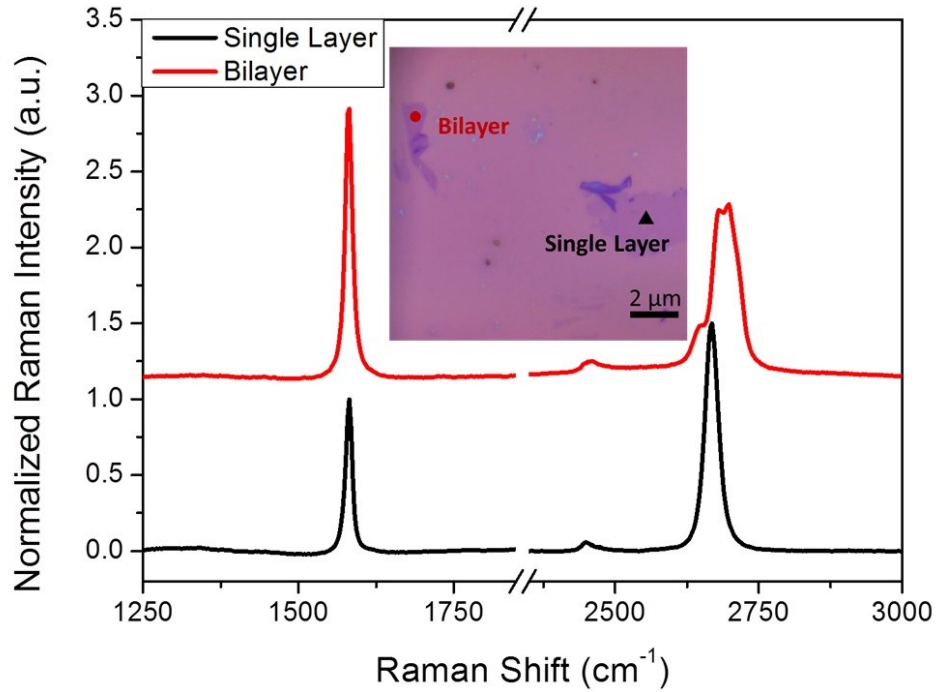


Figure 5.20 Typical Raman spectra of single-layer and bilayer flakes prepared by mechanical exfoliation.

Table 5.3 Information of G band and 2D band from Figure 5.20.

	Position	FWHM	Shape	A/A(G) Ratio	Bilayer to Single Layer Ratio
Single layer					
G Band	1582.04 cm ⁻¹	12.60 cm ⁻¹	Single Lorentz	—	—
2D Band	2668.38 cm ⁻¹	28.73 cm ⁻¹	Single Lorentz	3.47	—
Bilayer					
G Band	1579.68 cm ⁻¹	13.96 cm ⁻¹	Single Lorentz	—	2.20
2D Band	2692.06 cm ⁻¹	54.33 cm ⁻¹	Asymmetric	2.31	1.47

It is known that Bernal stacking is the preferential layer arrangement of graphite. Therefore, the Raman spectra of single-layer and bilayer flakes isolated from HOPG are provided here as

reference (Figure 5.20). Instead of the doubling in G band intensity, the change of 2D band profile is the most evidential signature of Bernal stacked bilayer graphene. The superposition of two single layers leads to the splitting in both conduction and valence bands, and hence creates additional pathways for 2D process (Figure 5.21 (a))^{40, 163}. As illustrated in Figure 5.21 (b), the four pathways, P₁₁, P₁₂, P₂₂, and P₂₁, involve with the optical phonon modes at 1395.6/1395.6 cm⁻¹ and 1400.0/1400.6 cm⁻¹^{42, 164}. Higher weight in the inner two peaks (corresponding to P₁₂ and P₂₁) could be related with a larger portion of phase space where the triple resonance is satisfied¹⁵⁴. As the results of split path, 2D band becomes broader and less symmetric, and can be fitted by a sum of four Lorentzians, each with a FWHM of ~24 cm⁻¹. It is also worth to mention that the intensity of 2D band doesn't increase as the number of graphene layers multiplies. Contrarily, the strong interaction between layers in Bernal stacking turns the linear dispersion relation around K and K' point into a parabolic one, and further weakens the intensity of 2D band.

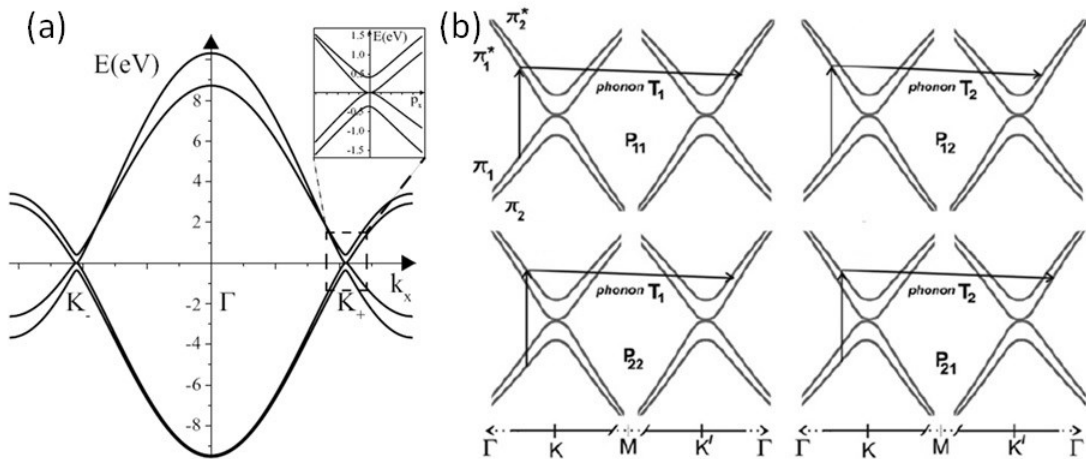


Figure 5.21 (a) Electronic band structure of Bernal stacked bilayer graphene (b) The four second-order Raman processes of 2D band.

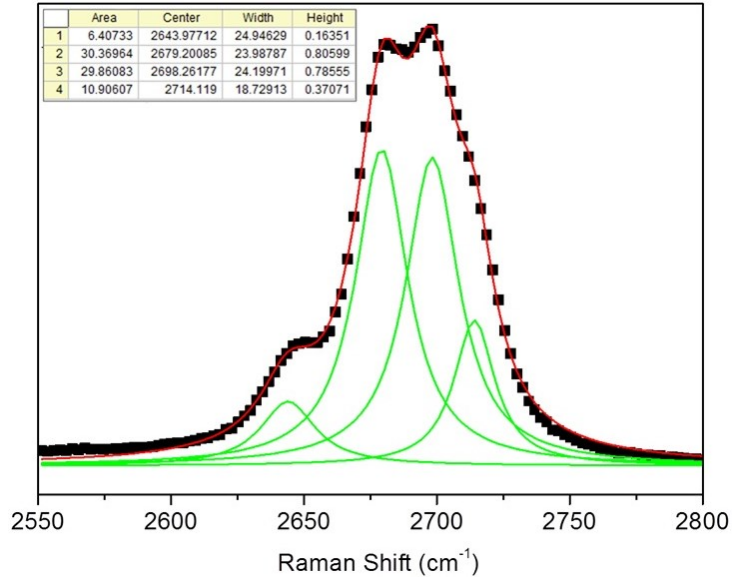


Figure 5.22 Fitting result of 2D band in Figure 5.20.

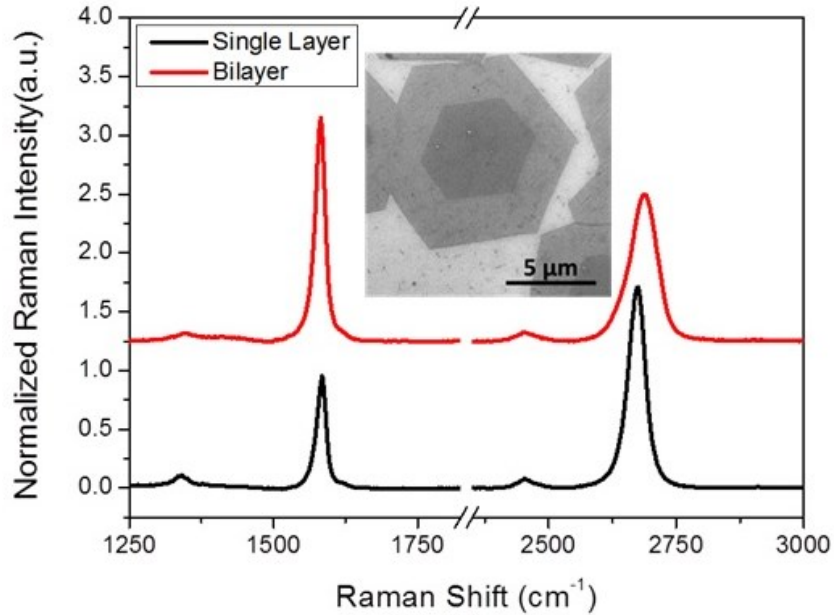


Figure 5.23 SEM image and Raman spectra of a typical 0-degree bilayer domain.

The capability of synthesizing perfect Bernal stacked bilayer graphene by CVD on polycrystalline Cu foil is still controversial, since the interaction between two graphene layers derives from the weak graphene-Cu interaction¹⁶⁵. Hence, the domains showing parallel edges

between two layers are referred as “0-degree” samples, rather than “Bernal stacked”. A typical 0-degree domain and its corresponding Raman spectra are shown in Figure 5.23.

Table 5.4 Information of G band and 2D band from Figure 5.23.

	Position	FWHM	Shape	A/A(G) Ratio	Bilayer to Single Layer Ratio
Single layer					
G Band	1584.71 cm ⁻¹	19.25 cm ⁻¹	Single Lorentz	—	—
2D Band	2675.62 cm ⁻¹	39.51 cm ⁻¹	Single Lorentz	3.52	—
Bilayer					
G Band	1582.04 cm ⁻¹	20.19 cm ⁻¹	Single Lorentz	—	2.09
2D Band	2687.00 cm ⁻¹	61.95 cm ⁻¹	Nearly Symmetric	1.77	1.05

Compared to the spectrum of Bernal stacked bilayer, the spectrum of bilayer from 0-degree sample shows considerable resemblances (Figure 5.23), as downshift and twice intensity of G band, upshift and broadening of 2D band. But the profile of 2D band remains symmetric to a certain extent. Although, it couldn't be fitted with single Lorentz peak perfectly, 3-peak fitting appears as competent as a 4-peak one (Figure 5.24), which implies the dissimilarity in electronic and phonon bands from the Bernal stacked. It is predicted that processes P_{12} and P_{21} would be degenerate, if the valence and conduction bands are mirror images of one another. Moreover, G band frequencies of both single layer and bilayer have been discovered slightly larger than the Bernal stacked cases, as the integrated effects of doping and strain. As mentioned before, the samples prepared via CVD growth and wet transfer process are unintentionally doped with holes. And the configuration, where a smaller second layer lies beneath the larger first layer, could introduce more strains, especially in the top layer, compared with the wedding cake configuration of exfoliated samples⁶⁶.

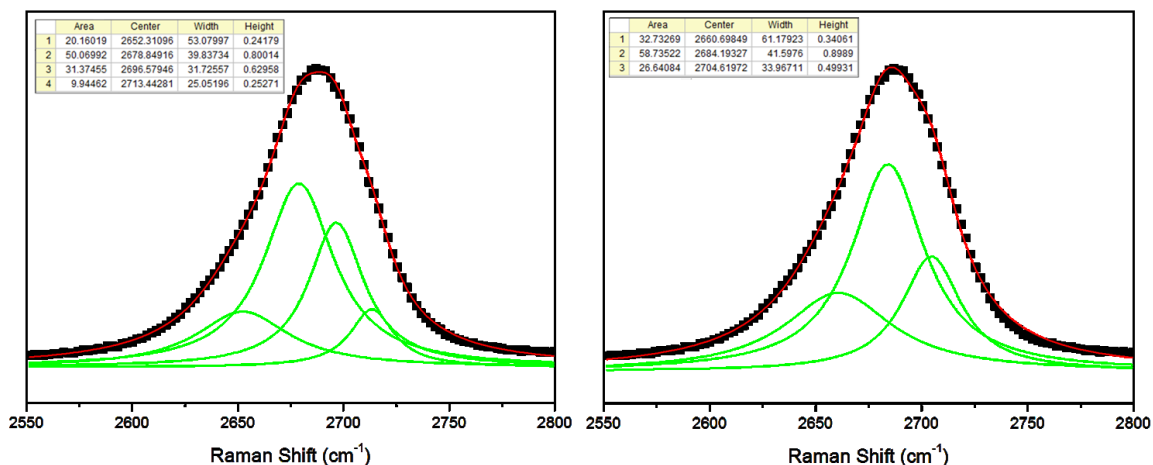


Figure 5.24 Fitting results of 2D band in Figure 5.23, with four Lorentzians (left) and three Lorentzians (right), respectively.

5.4.3 Raman Features of Twisted Bilayer Graphene — G Resonance

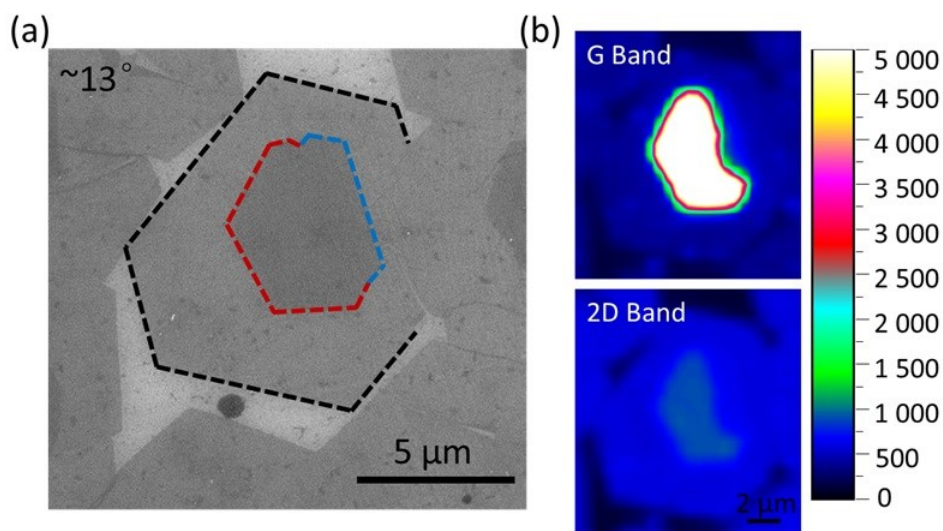


Figure 5.25 SEM image (a) and Raman mappings (b) of a bilayer graphene island consisting of a twinning structure on the second layer.

The most striking Raman feature of twisted bilayer graphene is the G band becomes resonant with excitation laser, enabling an over 50 times enhancement in intensity. However, this feature hadn't been explored thoroughly till 2012^{62, 63}. Probably limited by the size and quality of

samples studied in the initial phase, the anomalous intensity of G band was easily misinterpreted as the non-uniformity of thickness.

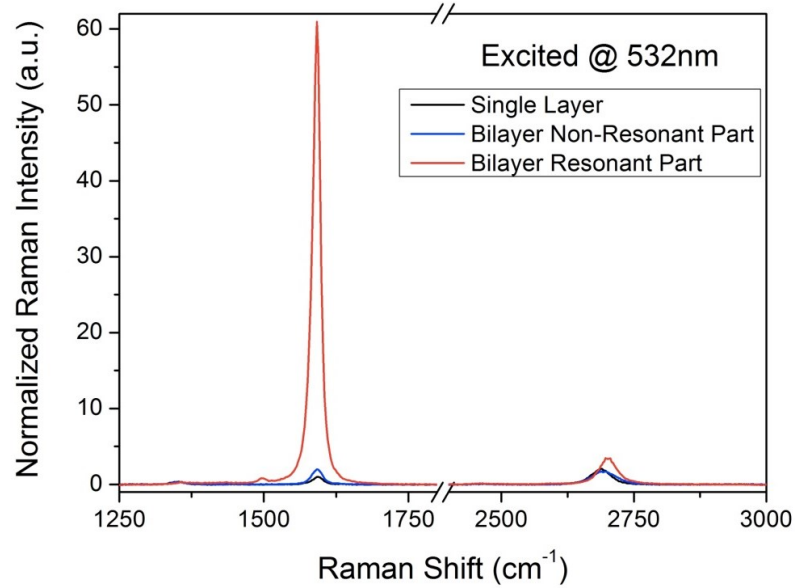


Figure 5.26 Raman spectra of bilayer island shown in Figure 5.25.

Table 5.5 Information of G band and 2D band from Figure 5.26.

	Position	FWHM	Shape	A/A(G) Ratio	Bilayer to Single Layer Ratio
Single layer					
G Band	1591.77 cm ⁻¹	17.30 cm ⁻¹	Single Lorentz	—	—
2D Band	2687.06 cm ⁻¹	41.62 cm ⁻¹	Single Lorentz	4.08	—
Bilayer Resonant Part					
G Band	1586.56 cm ⁻¹	18.32 cm ⁻¹	Single Lorentz	—	58.51
2D Band	2700.10 cm ⁻¹	35.93 cm ⁻¹	Single Lorentz	0.15	1.74
Bilayer Non-Resonant Part					
G Band	1589.16 cm ⁻¹	22.85 cm ⁻¹	Single Lorentz	—	2.03
2D Band	2692.27 cm ⁻¹	58.39 cm ⁻¹	Nearly Symmetric	1.55	1.03

As introduced in the beginning of this chapter, when a Raman process involves with a real stationary state, the electron-phonon, electron-electron interaction will be dramatically influence the cross section of Raman scattering. For twisted bilayer graphene, the presence of van Hove

singularities in the density of π electron states is considered as the origin of G resonance for specific incident laser energies $E_{\text{resonance}}$ defined by the twist angle θ ¹⁶⁶. The bilayer island labeled in Figure 5.25 (black dash line) consists of two twinning domains on the second layer. For the right one (blue dash line) possesses nearly parallel edges to the first layer, referred to a 0-degree case; while the left one (red dash line) aligns rotationally, with an angle of $\sim 13^\circ$ related to the first layer. Due to the different stacking order, when the left half meets the resonance condition, in this case at 2.33 eV, and appears saturate in the Raman mapping of G band, the right half is off-resonance. By examining the spectra, an over $50\times$ enhancement in G band intensity has been found for the 13-degree domain at excitation laser of 532 nm. Besides, a narrow quasi-Lorentz 2D band is observed, with a noticeable blueshift, up to $\sim 10\text{ cm}^{-1}$, resulting from a reduced Fermi velocity¹⁶⁷. This distinctive 2D band will further discussed in section below.

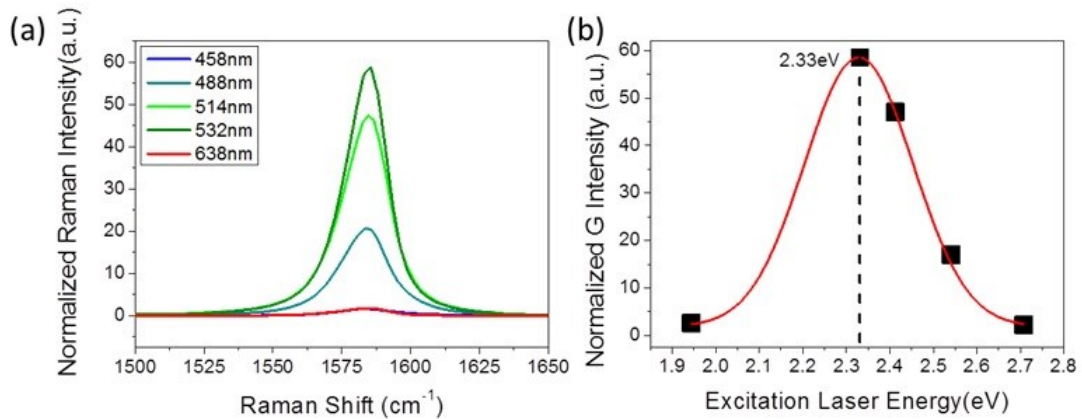


Figure 5.27 (a) Raman spectra of 13-degree domain under different laser excitation. (b) Plot of normalized G band intensity versus excitation laser energy (black squares) and fitting result of Gaussian (red line).

The dependence of G resonance on excitation laser energies is demonstrated in Figure 5.27.

In order to compare the enhancement factor, the spectra were normalized with the single-layer

value for each excitation laser energy, respectively. Based on the rotated band approximation, the relation between resonant laser energy and rotation angle can be roughly depicted as

$$\theta = 3aE_{resonance} / \hbar v_f 4\pi, \quad (5.1)$$

where a is the lattice parameter of graphene (2.46 \AA), \hbar is the reduced Planck's constant, and v_f is the Fermi velocity of monolayer graphene (10^6 m/s)⁶³. Although the rotated band approximation is defective with respect to understanding the additional phonon modes and 2D band behavior, it provides a simple method to predict the resonant behavior of G band, which agrees well with most reported cases and our observation^{59, 62, 63, 166}.

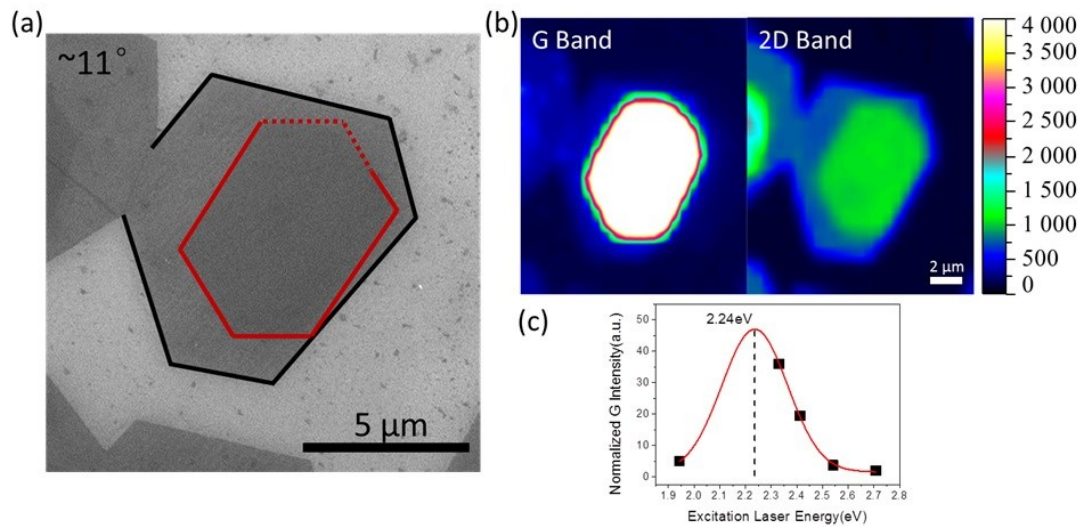


Figure 5.28 SEM image (a) and Raman mappings at 532 nm (b) of a single crystal bilayer graphene island. (c) Plot of normalized G band intensity versus excitation laser energy (black squares) and fitting result of Gaussian (red line).

The island portrayed in Figure 5.28, retaining single domain on the second layer with a rotation angle around 11° , also shows strong G band enhancement under excitation of 532 nm laser. But the profile of laser energy-normalized G band intensity plot appears different from the one in Figure 5.27 (b). From the fitting result (Figure 5.27 (c)), it is observable that the resonant

laser energy shifts to a lower one, 2.24 eV as the result of smaller rotation angle. Similarly, Figure 5.29 presents another twinning bilayer island, but with the G resonance arising on the right part (red dash line) at 638 nm, of which the rotation angle is $\sim 9^\circ$. As shown in Figure 5.28 (c), although, the lack of data points makes it difficult to sketch the complete outline, it is reasonable to deduce that the resonant energies should be under 1.94 eV. From above three examples, we can clearly see how the resonant G band intensity is sensitive to the rotation angle. This can be utilized as a reliable way to determine the relative rotation of twisted bilayer graphene.

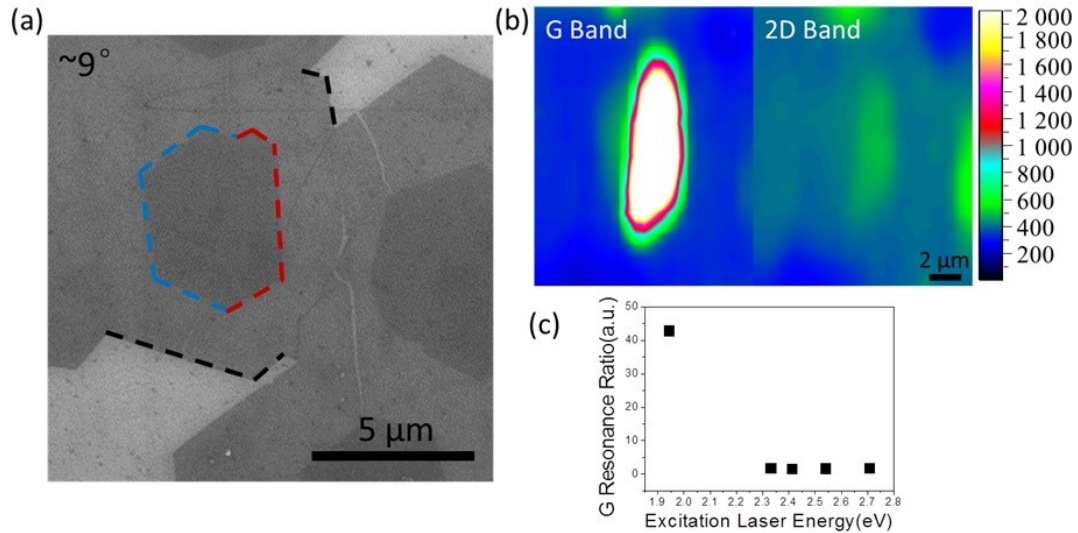


Figure 5.29 SEM image (a) and Raman mappings at 638 nm (b) of a bilayer graphene island consisting of a twinning structure on the second layer. (c) Plot of G band intensity versus excitation laser energy for the resonant part.

It is worth to mention that most twisted bilayer samples studied in the literature possess a rotation angle in the range of $8\sim 13^\circ$, because of the corresponding resonant laser energy lies in the visible light range, as demonstrated above. With a single-Lorentz shape 2D band and analogous $A(2D)/A(G)$ ratio to the single-layer one under visible laser excitation, the existence of

strong interaction between layers with relative large rotation angle was under debated^{62, 63}. Based on some STM investigation, the electronic properties of tBLG are even expected indistinguishable from those in SLG for rotation angles $>20^\circ$ ⁶⁰. This assumption is overruled by our observation of G resonance for bilayer domains with rotation angle as large as 25° (Figure 5.30). A home-built microscopic Raman system equipped with UV laser source at 363.8 nm was applied here to satisfy the requirement in resonant laser energy. An over 20 \times enhancement in G intensity has been witnessed.

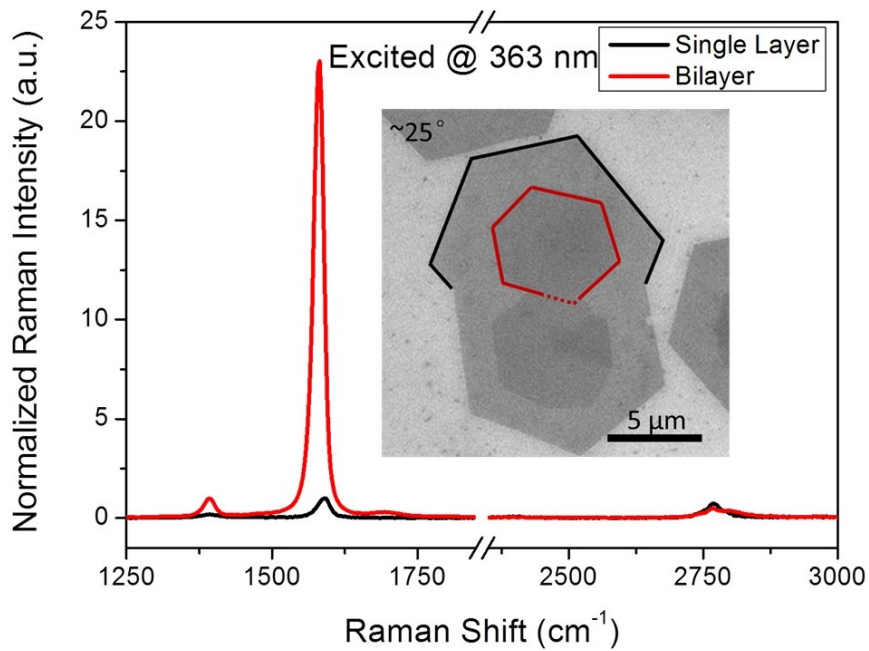


Figure 5.30 SEM image and Raman spectra of bilayer domain with rotation angle about 25° , with excitation of 363.8 nm laser.

5.4.4 Raman Features of Twisted Bilayer Graphene — Folded Phonon Modes

As demonstrated in Chapter 2, the misalignment of two graphene layers can give rise of a new periodic structure, superlattice, which is highly dependent on the rotation angle and considered as the origin of most distinctive behavior of twisted bilayer graphene. This complex

structure can activate some new Raman processes involving phonons with varied wavevectors, leading to the appearance of new peaks in the spectrum^{168, 169}.

Different from the characteristic features, like G and 2D band, these new Raman peaks have relatively small cross sections, hence lower intensities and easy to be overlooked. Figure 5.31 and Table 5.6 & 5.7 reveal the diversity and complexity of these Raman processes which can be attributed to in-plane and out-of-plane acoustic phonon modes at either K point or Γ points^{168,}

169

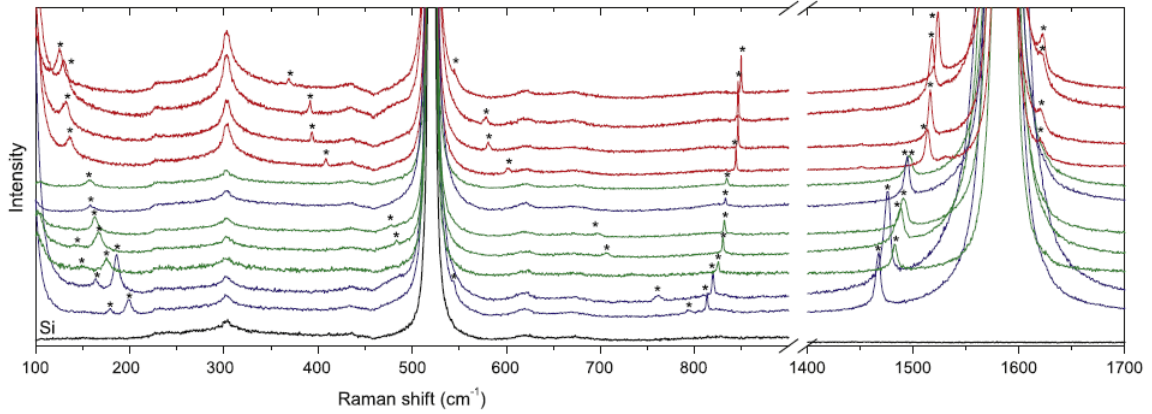


Figure 5.31 Raman spectra of tBLGs with different rotation angles on a Si/SiO₂ substrate. The * symbols point to the superlattice-induced Raman peaks. Curve coloring corresponds to the excitation laser energy: 1.96 eV (red), 2.41 eV (green), and 2.54 eV (blue).

Table 5.6 Frequencies of the out-plane optical phonons at the Γ points (cm⁻¹).

SLG	BLG	T-BLG $\theta = 21.8^\circ$	T-BLG $\theta = 13.2^\circ$	T-BLG $\theta = 9.4^\circ$	T-BLG $\theta = 7.3^\circ$
894.1	895.9	725.6–728.2 (12)	651.3–653.1 (12)	619.6–621.8 (12)	602.6 (6)
	897.4	896.36 (2)	707.4–708.0 (12)	672.9–675.5 (24)	604.6–605.0 (6)
			836.8–837.7 (12)	769.4–769.5 (12)	650.1–652.9 (24)
			896.34 (2)	802.1 (12)	666.7–667.6 (12)
				866.7–867.5 (12)	721.8 (12)
				896.34 (2)	759.3–760.7 (24)
					821.6–821.7 (12)
					841.2 (12)
					878.6–879.4 (12)
					896.35 (2)

Table 5.7 Frequencies of the in-plane optical phonons at the Γ and K points (cm^{-1}).

SLG	BLG	T-BLG $\theta = 21.8^\circ$	T-BLG $\theta = 13.2^\circ$	T-BLG $\theta = 9.4^\circ$	T-BLG $\theta = 7.3^\circ$
			Γ point		
1589.45 (2)	1589.43 (2)	1378.6–1378.7 (12)	1353.0–1353.1 (12)	1312.9–1313.0 (12)	1213.8–1214.7 (24)
	1589.52 (2)	1468.8–1468.9 (12)	1363.1–1363.2 (12)	1348.8–1350.0 (24)	1282.5–1282.6 (12)
		1589.47 (4)	1367.2–1367.3 (12)	1354.2 (12)	1345.6–1345.8 (24)
			1458.8 (12)	1407.9–1408.3 (24)	1348.6–1350.1 (24)
			1479.3–1479.4 (12)	1417.9 (12)	1367.5 (12)
			1564.1–1564.2 (12)	1434.0 (12)	1377.6–1378.7 (24)
			1589.48 (4)	1509.5 (12)	1395.8–1395.9 (12)
				1527.1 (12)	1398.5 (12)
				1543.8 (12)	1409.4 (12)
				1580.2–1580.3 (12)	1458.5–1459.4 (24)
				1589.48 (4)	1483.5 (12)
					1506.4 (12)
					1509.8 (12)
					1550.1 (12)
					1553.4 (12)
					1568.5 (12)
					1584.9–1585.0 (12)
					1589.48 (4)
			K point		
1197.3	1197.3 (2)	1197.4 (2)	1197.4 (2)	1197.4 (2)	1197.4 (2)
1347.4	1347.4	1347.4 (2)	1260.5 (6)	1259.6 (6)	1251.8 (6)
	1347.5	1350.7–1350.8 (6)	1339.8–1340.8 (12)	1262.9 (6)	1254.7 (6)
		1411.6–1411.7 (6)	1347.4 (2)	1299.7 (6)	1274.4–1276.8 (12)
		1486.8 (6)	1351.4 (6)	1317.4 (6)	1284.7 (6)
		1569.0–1569.1 (6)	1365.2 (6)	1340.2 (6)	1339.0–1341.0 (12)
			1390.4 (6)	1344.0 (6)	1345.6 (6)
			1395.6 (6)	1347.4 (2)	1347.4 (2)
			1449.6 (6)	1348.7 (6)	1348.2–1350.1 (12)
			1491.5 (6)	1363.2 (6)	1354.3 (6)
			1498.2 (6)	1367.4 (6)	1356.6–1357.4 (12)
			1547.3 (6)	1371.1–1371.9 (12)	1360.1–1362.4 (12)
			1552.8 (6)	1394.2 (6)	1370.4 (6)
			1584.7 (6)	1398.0 (6)	1374.4 (6)
				1424.0 (6)	1376.3–1376.6 (12)
				1430.3 (6)	1381.6 (6)
				1461.5–1462.9 (12)	1411.0–1412.7 (12)
				1476.7 (6)	1425.6 (6)
				1501.5 (6)	1438.9 (6)
				1506.4–1508.2 (12)	1444.7 (6)
				1555.8–1557.3 (12)	1448.9 (6)
				1567.2 (6)	1450.3 (6)
				1576.4 (6)	1452.6 (6)
				1587.5 (6)	1458.4 (6)
					1486.1 (6)
					1504.4–1504.9 (12)
					1514.2–1516.3 (12)
					1537.6–1538.2 (12)
					1549.9–1551.6 (12)
					1574.1–1575.8 (18)
					1583.1 (6)
					1588.4 (6)

In this study, we only focus on the folded phonon mode accompanying with the G resonance. For the bilayer domain with rotation angle of $\sim 25^\circ$, besides the enhanced G band, a broad band appears at $\sim 1380 \text{ cm}^{-1}$ with significant intensity, even stronger than 2D band, in

Figure 5.30. Although the position of this band is very closed to the D band, the possibility of assigning as D band can be ruled out based on the following observation. Figure 5.32 presents Raman spectra of a series of twisted bilayer domains with different rotation angles, suggesting by the difference in enhancement factors of G band. And according to the position of 2D band, the D band position of bilayer graphene under 363.8 nm laser excitation should be around 1390 cm^{-1} , labeled as dash line in inserted spectrum. However, the position of the additional band varies from case to case. For the cyan colored curve, this band even splits into two components with the left one sitting at $\sim 1390\text{ cm}^{-1}$. It is reasonable to deduce that there is another band besides D band.

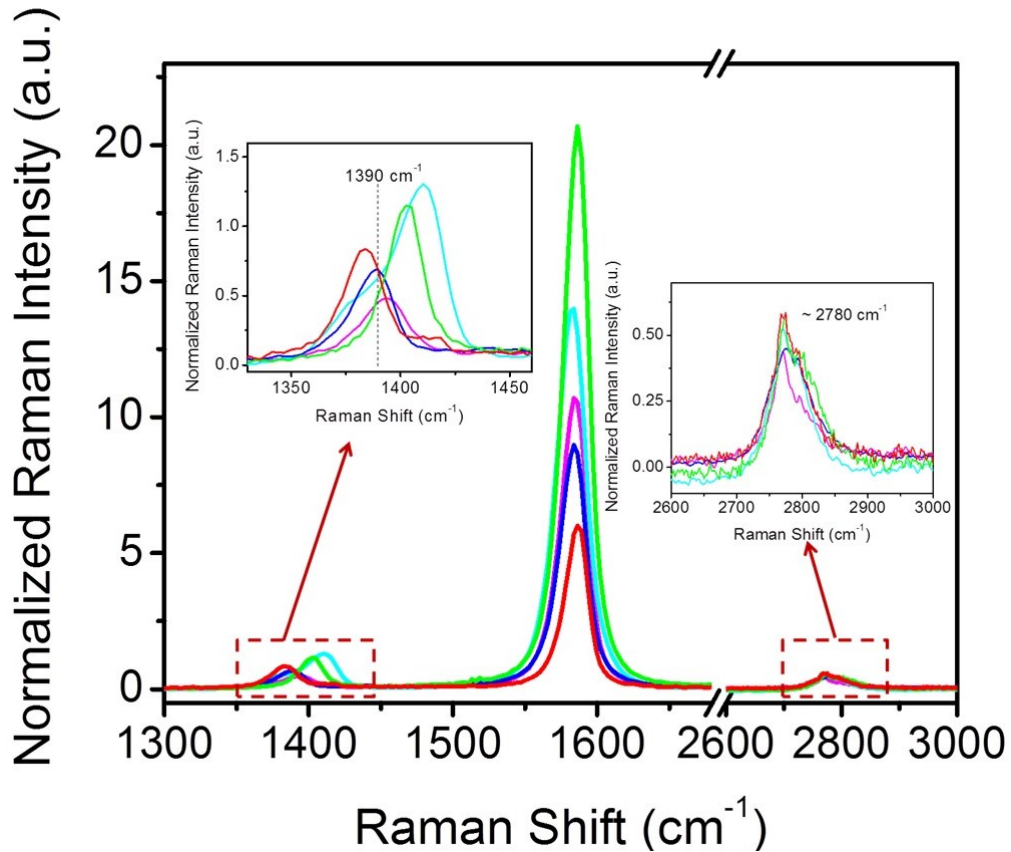


Figure 5.32 Raman spectra of a series of twisted bilayer domains show enhancement in G band under the excitation of 363.8 nm laser.

Not only for the UV measurement, this additional phonon mode can also be detected with visible laser as long as the resonant condition is satisfied. Figure 5.33 (a) is an enlarged view of Figure 5.26 for the 13-degree domain resonant at 532 nm. There is a small peak emerging at $\sim 1490\text{ cm}^{-1}$, apart from the position of D band, $\sim 1340\text{ cm}^{-1}$, under this laser excitation condition. And no obvious dispersion in position has been witnessed in Figure 5.33 (b).

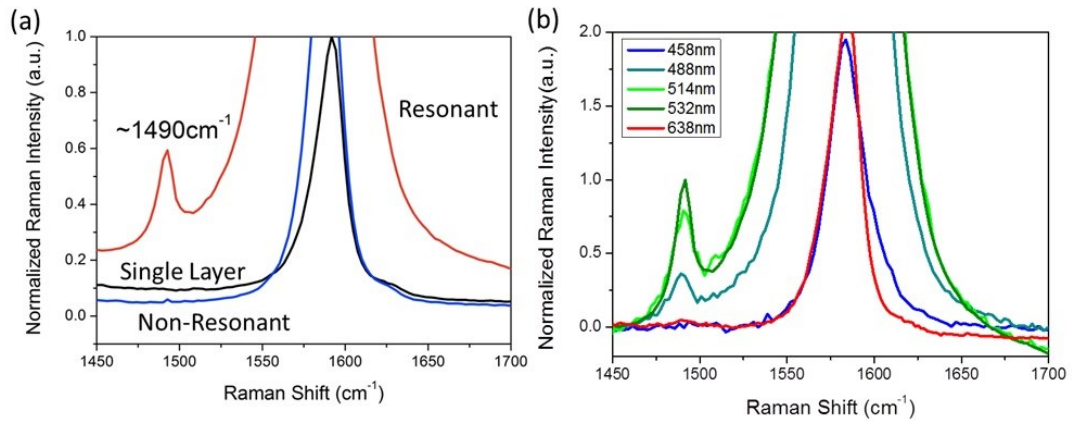


Figure 5.33 Enlarged views of Figure 5.26 and Figure 5.27, respectively, for the 13-degree bilayer domain with G resonance around 532 nm.

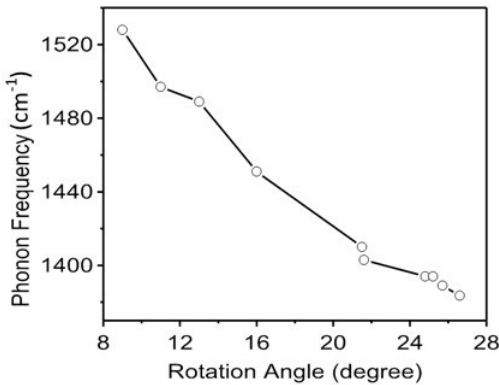


Figure 5.34 Observed phonon frequencies as a function of rotation angle.

After investigating tens of domains, a dependence of observed phonon frequencies on the rotation angles has been discovered and summarized in Figure 5.34. To understand the behavior

of this new phonon mode, a widely used ascription in 1-D superlattices, folded phonon, is introduced here¹⁷⁰. Conventionally, the frequency of folded phonons can be estimated by zone folding of the initial phonon dispersion curve into the reduced Brillouin zone (rBZ) of the superlattices. Figure 5.35 (b) shows BZ of single-layer graphene (outer hexagon), rBZ of the bilayer superlattice with a rotation angle of 13.2° (inner hexagon) and two sets of six-fold reciprocal lattices A and B of the superlattice. It is the position of these reciprocal lattices that determines the frequency of folded phonons. This can be understood in the following two ways using reciprocal lattice A as an example. When transverse optical (TO) dispersion in the larger BZ of single-layer graphene is mapped into the reduced BZ of the superlattice, point A will be mapped to the Γ -point of the BZ, and becomes Γ -point optical phonons that can be probed by Raman scattering. Another way to say this is that the Moiré lattice BZ vector $q(\theta) = \frac{8\pi}{\sqrt{3}a} \sin(\frac{\theta}{2})$ is equal to the crystal momentum Γ -A, of which frequency can be calculated directly for the specific point A in the SLG BZ¹⁷¹. Figure 5.35 (c) compares the experimental folded phonon frequencies (open circles) with those calculated for point A in SLG BZ (red curve) at angles between 0° and 30°. Both sets of frequencies are plotted against the Moiré vector $q(\theta)$. The experimental frequencies follow closely the calculated frequency dependence, which suggests that the Moiré lattice is a good approximation to the tBLG superlattice realized in our samples. According to the zone folding shown in Figure 5.35 (b), two different phonon modes are expected from reciprocal lattices A and B, but a lower-frequency phonon at B has not been observed in this study. This is probably related with a smaller cross

section for the Raman process involving higher-order crystal momentum Γ -B. And also because Γ -A is closer in energy to the G-line compared with the folded phonon Γ -B. The Γ -A phonon is thus more likely to be resonantly excited when the resonance condition for the G-line is satisfied.

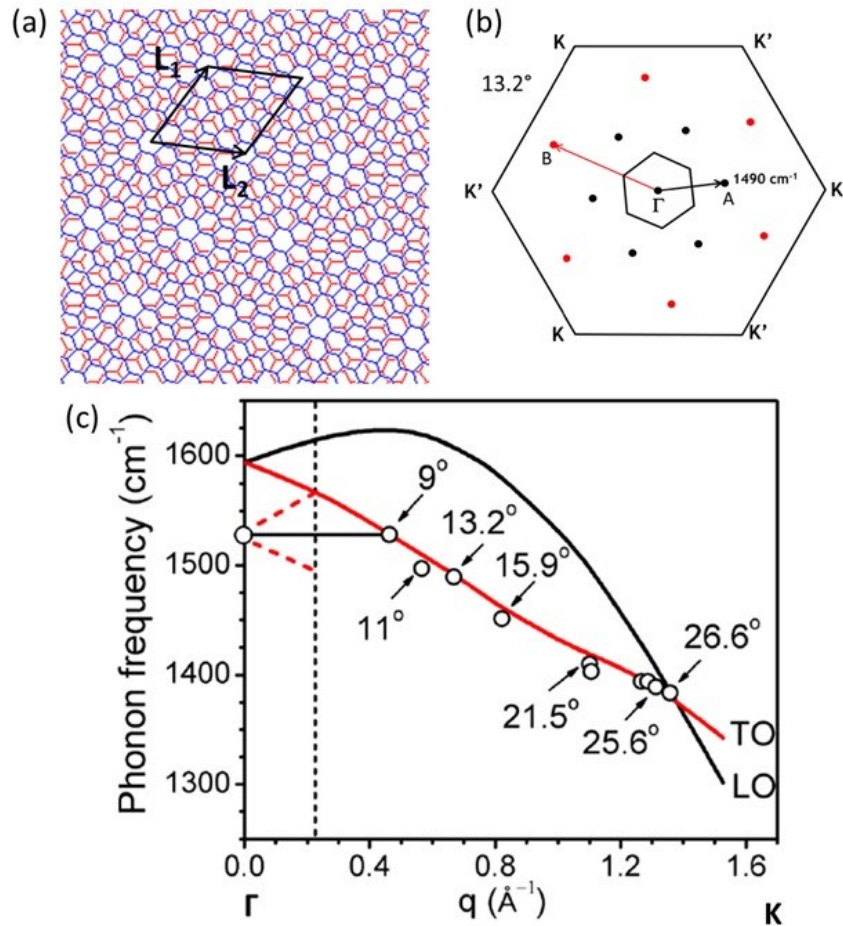


Figure 5.35 Schematic drawings of tBLG superlattice with rotation angle of 13.2° in real space (a) and in reciprocal space (b). (c) Calculated (solid line) and experimental (open circles) folded phonon frequencies as a function of reciprocal wave vector of superlattice.

5.4.5 Raman Features of Twisted Bilayer Graphene — Enhancement of 2D Band

Besides G resonance and folded phonon mode, 2D band of tBLGs also behaves differently compared with the Bernal stacked or 0-degree bilayer. As shown in Figure 5.26 and Table 5.5, a slim and nearly Lorentz-shaped 2D band, instead of a broad and split one, was observed for the

domain with rotation angle of $\sim 13^\circ$, with excitation laser of 532 nm. The small FWHM(2D) of this twisted bilayer domain, even smaller than the value of single-layer part, couldn't be explained by doping or strain effects.

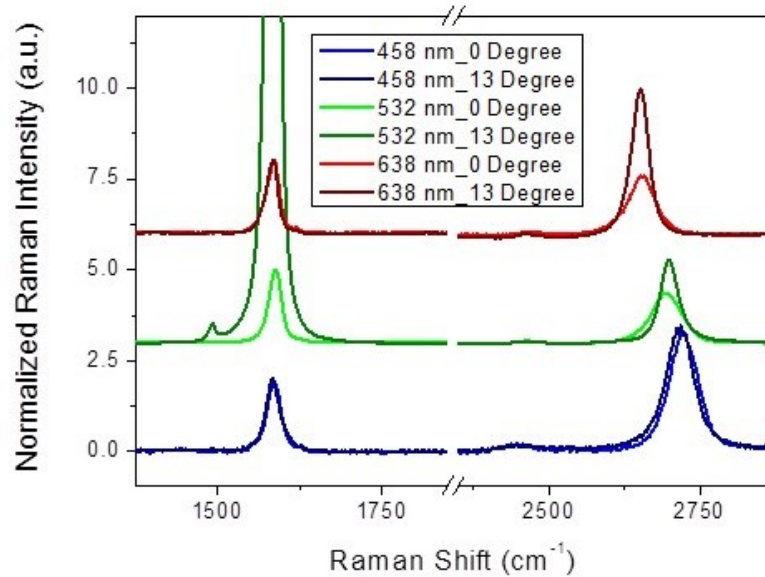


Figure 5.36 Normalized Raman spectra of 0-degree and 13-degree domain in the twinning structure shown in Figure 5.25, under different laser excitation.

When we take a closer look at the intensity of 2D band under various excitation energies, a more peculiar phenomenon has been revealed. For the twinning bilayer domains shown in Figure 5.25, it has been demonstrated that the 13-degree domain can exhibit enhanced G band with the excitation energies between 2.33 to 2.54 eV. But it is off-resonant when excited with 458 nm or 638 nm laser. And the other domain with nearly 0° rotation is always off-resonant under all the performed conditions. The normalized spectra of this twinning structure are plotted in Figure 5.36. When the excitation energy increasing from 1.94 eV (638 nm), achieving and exceeding the resonant energy, the 2D band profile of the 13-degree domain evolves from a strong, narrow,

Lorentz peak to a broader one identical with the 0-degree case. This suggests the processes of 2D band are also relied on the resonant condition of G band.

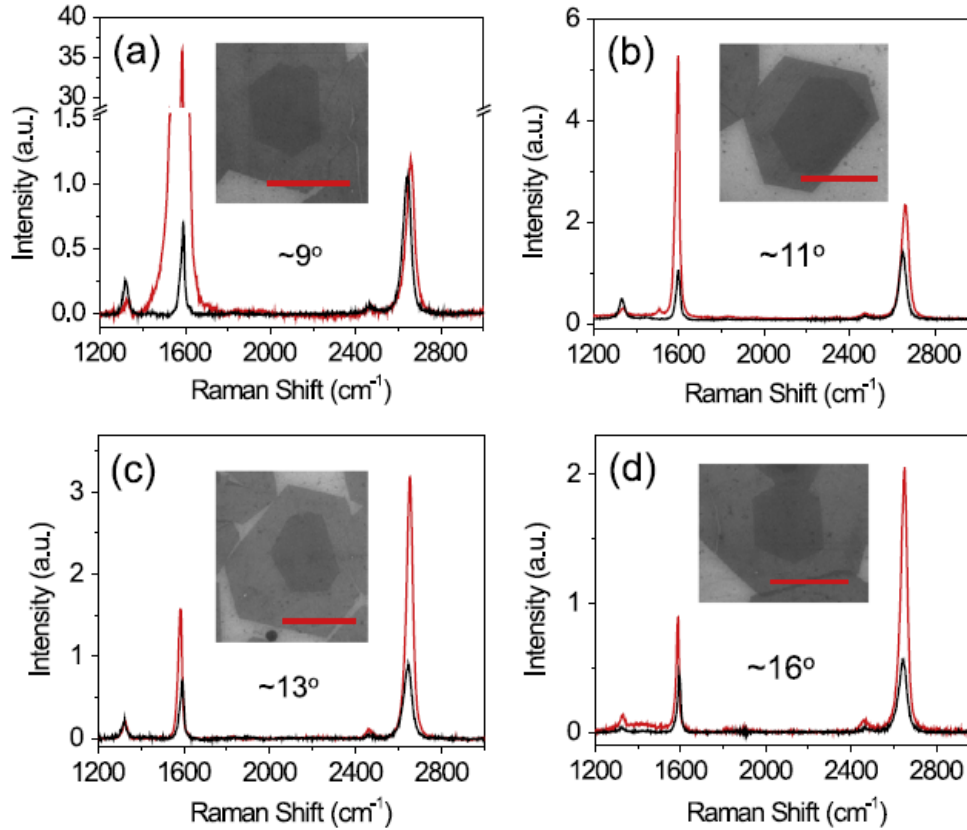


Figure 5.37 Raman spectra of single-layer (in black) and twisted bilayer graphene (in red) with rotation angles of 9, 11, 13 and 16 degrees. Insets are scanning electron microscopy (SEM) images. The excitation laser wavelength is 638 nm. The scale bar is 5 μm .

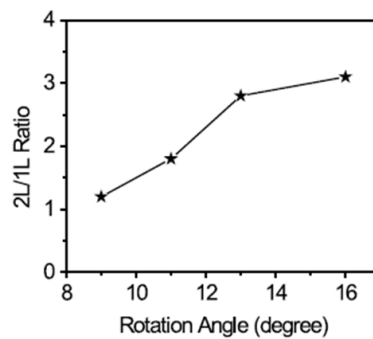


Figure 5.38 Normalized 2D band intensity of bilayer versus single-layer graphene as a function of the rotation angle.

To further understand the relation between 2D band profile and the rotation angle, a series of Raman measurements were carried out for different twisted bilayer domains with same excitation energy, 1.94 eV in this case (Figure 5.37). The G resonances can be observed in samples with smaller 9° and 11° rotation angles. The folded phonon can also be seen in Figure 5.37 (b) near 1500 cm^{-1} . In addition, the significant change in the intensity of 2D band has also been verified; the integrated intensity conducts a direct proportion to the rotation angles, as summarized in Figure 5.38. When the G band resonance energy is far above laser excitation energy, the 2D intensity becomes more than twice that of the single-layer graphene. And this observation regarding our bilayer graphene with a rotation angle larger than 20 degrees is general, of which resonant energy is as high as $\sim 3.58\text{ eV}$. Figure 5.39 gives the spectra of two domains with rotation angles around 25° . As can be seen, while the intensity of the G-line in the tBLG is doubled, the 2D band intensity becomes about four times stronger.

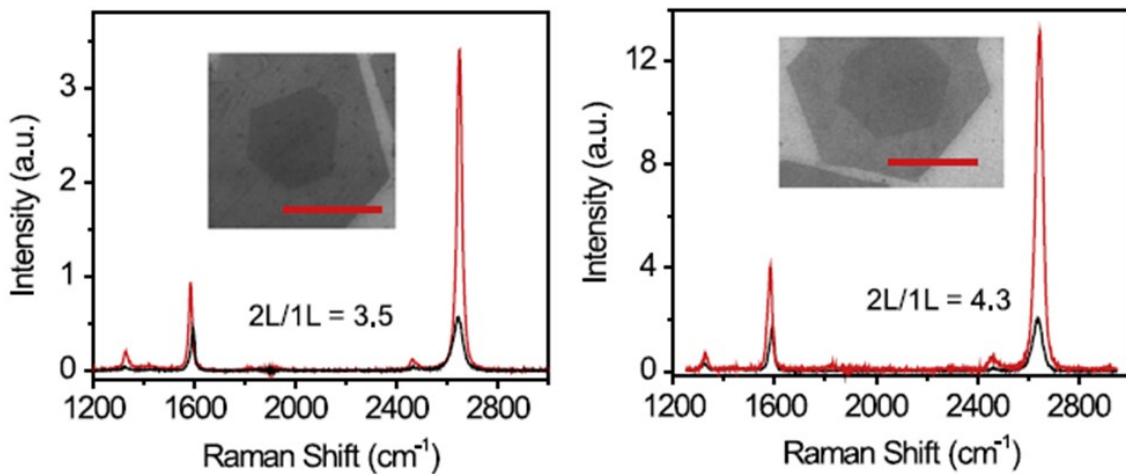


Figure 5.39 Raman spectra of single-layer (in black) and twisted bilayer (in red) graphene. Insets in (b) and (c) are SEM images of these tBLGs with large rotation angles near $\sim 25^\circ$.

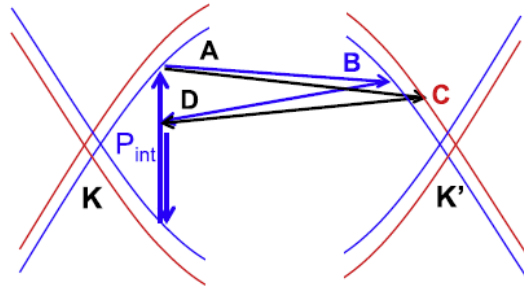


Figure 5.40 Example of two degenerate 2D Raman pathways involving an interband transition between the inner loops. The excitation laser is tuned below the G resonance of the tBLG.

To explain the enhancement in 2D intensity, the schematic drawing of the band structures of the tBLG is presented here, under assumption that twisted bilayer graphene forms two-dimensional superlattices, defined by the Moiré pattern. For simplification, only two Raman pathways that involve an interband transition between the two inner Dirac bands: $A \rightarrow B \rightarrow D$ and $A \rightarrow C \rightarrow D$, as in Bernal stacked bilayer graphene, are taken into discussion. First, we note that there are two absorption pathways for an incident photon, either through outer loop interband transition or through inner loop interband transition P_{int} , as indicated in figure 5. As a result, the G band intensity simply doubles in comparison to the one in single-layer graphene. But for 2D Band, the Raman pathway evenly splits into P_{ABD} and P_{ACD} after reaching the virtual state A, with $\frac{1}{\sqrt{2}}$ of the incident amplitude at point A ($\frac{1}{2}$ of the total incident amplitude). For Bernal stacking, $A \rightarrow B \rightarrow D$ and $A \rightarrow C \rightarrow D$ are two independent processes, because of a big splitting of ~ 300 meV between the two band branches. The total Raman intensity is the sum of the intensity of individual pathways (as $\frac{1}{4} + \frac{1}{4} + \frac{1}{4} + \frac{1}{4}$), and is expected as the same value as the single-layer one. However, the gap between two Dirac bands for tBLGs is considerably small (~ 20 meV for

13.2° rotated tBLG), thereby, the band below the M point, or G resonance, becomes a degenerate Dirac band. Quantum interference has to be concerned. The Raman intensity is calculated as a square of the superposed amplitude of each pathway (as $\left| \frac{1}{2} + \frac{1}{2} + \frac{1}{2} + \frac{1}{2} \right|^2$), which is four-times of that is found in single-layer graphene. Besides, if there is no interlayer coupling, referred as decoupled bilayer graphene, the two graphene layers are then independent from each other, and the total Raman intensity is simply twice that of the single layer.

To summarize, the characteristic Raman features for Bernal stacked bilayer graphene flakes isolated from HOPG, quasi-Bernal stacked and twisted bilayer graphene hexagon domains synthesized by CVD method have been systematically investigated in this section. Especially for twisted bilayer domains, the correlation of G resonance, folded phonon mode, and enhancement of 2D band has been apprehended from a bilayer superlattice view. Raman spectroscopy has been demonstrated as a versatile tool to reveal the stacking order and underlying electronic band structure of graphene samples.

5.5 Raman Spectroscopy Study of Bilayer Graphene Domains Synthesized by Artificial Stacking

Although artificial folding of single-layer graphene flakes was the dominant approach to prepare twisted bilayer samples in the early phase of studies, the size of as-prepared samples is limited and impedes further application. Apparently, CVD method is more practical for synthesizing scalable samples with high quality, however, the protocols developed so far still provides not adequate control in stacking orders. Therefore, artificial stacking of two single layers,

synthesized by CVD, with predefined rotation angle is a promising alternative for creating complex graphene based structures.

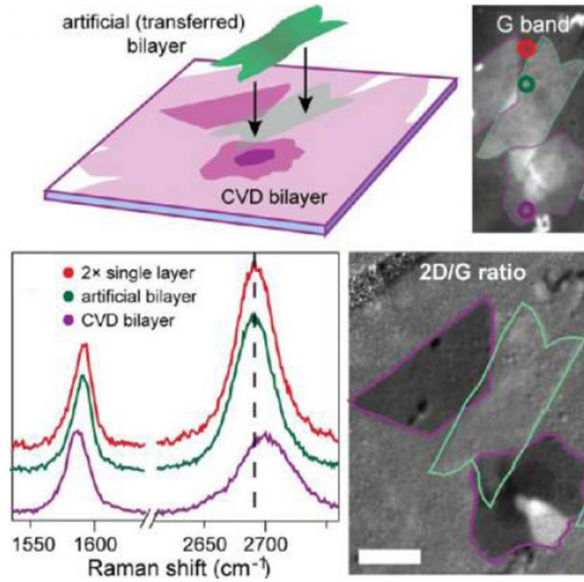


Figure 5.41 Schematic of sample; G band and 2D/G image showing CVD and artificial bilayer regions; and Raman spectra from single layer, CVD bilayer, and artificial bilayer. (scale bar 5 μm).

The most debatable issue of artificial stacking is the possibility of forming robust interlayer coupling with unavoidable residues, induced during the polymer-assistant transfer process, in between. As shown in Ref. 65, two SLG layers was sequentially transferred onto the substrate, but separated by debris and in very loose contact. A separation as large as 1 nm has been detected by AFM. Hence, the Raman spectra of this decoupled bilayer sample exhibited identical features as single layer (Figure 5.41). Additional annealing step was expected to reinforce the coupling and restore bilayer Raman features somehow.

But as discussed in Chapter 4, in order to avoided undesirable doping effects, there is no annealing step in the recipe of artificial stacking executed in this study. Nevertheless, the Raman

signatures of twisted bilayer graphene, like G resonance, folded phonon mode, and enhancement in 2D band have been identified on the artificial stacking domains prepared here. This indicates a rather clean transfer process has been achieved.

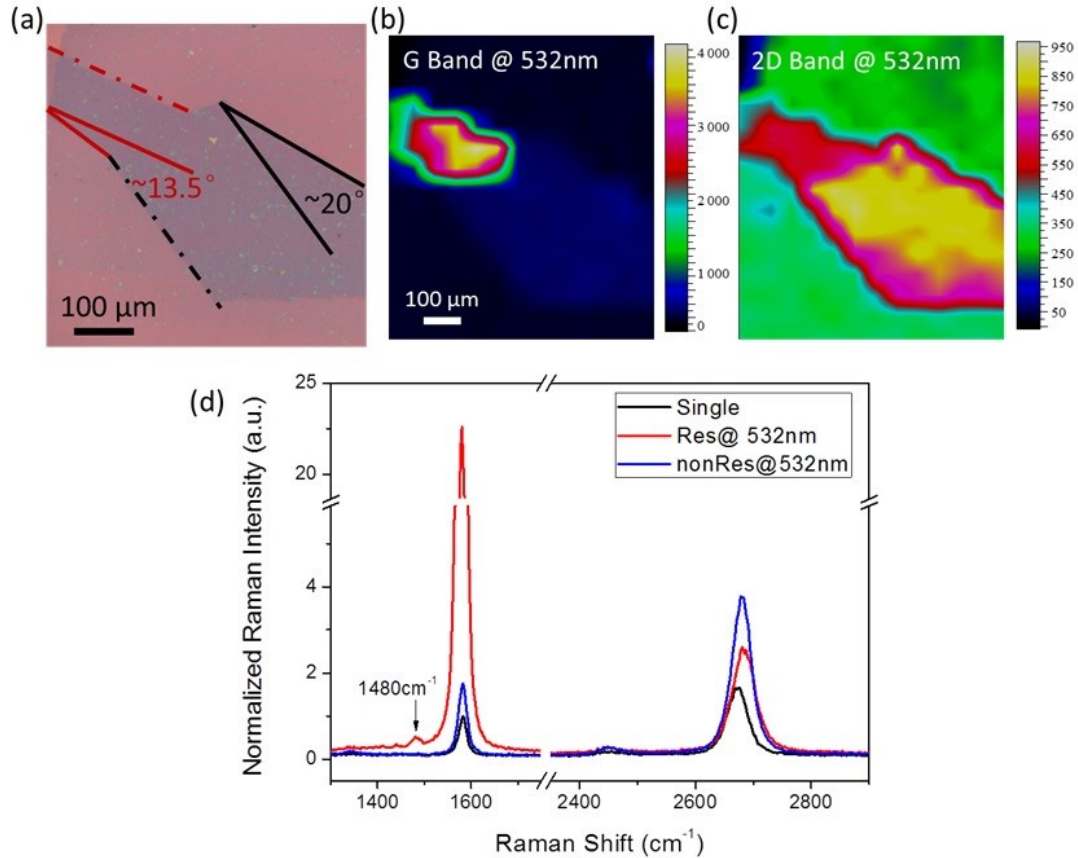


Figure 5.42 Optical microscope image (a), Raman mapping (b-c), and point measurements (d) of twisted bilayer domains prepared by artificial stacking.

As shown in Figure 5.42, one artificial stacked bilayer graphene islands consists of a twinning structure with rotation angles of $\sim 13.5^\circ$ and $\sim 20^\circ$, respectively. An over $20\times$ enhancement of G band has been detected on the $\sim 13.5^\circ$ one, of which size is as large as hundreds of μm^2 , under 532 nm laser excitation. And the appearance of folded phonon mode at $1480\ \text{cm}^{-1}$ agrees with the prediction from zone folding of the bilayer superlattice (Figure 5.35 (c)). On the other hand, the

one with $\sim 20^\circ$ has quasi-Lorentz 2D band with intensity larger than two times of the single-layer value. Based on these analogous Raman behaviors to CVD grown domains, the coupling retained in artificial stacked bilayer has been testified, and consequently the practicability of artificial stacking developed in this dissertation has been proved.

Table 5.8 Information of G band and 2D band from Figure 5.42.

	Position	FWHM	Shape	A/A(G) Ratio	Bilayer to Single Layer Ratio
Single layer					
G Band	1582.67 cm^{-1}	19.39 cm^{-1}	Single Lorentz	—	—
2D Band	2675.82 cm^{-1}	43.56 cm^{-1}	Single Lorentz	3.95	—
Bilayer Resonant Part					
G Band	1580.00 cm^{-1}	19.15 cm^{-1}	Single Lorentz	—	21.17
2D Band	2680.39 cm^{-1}	47.02 cm^{-1}	Nearly Symmetric	0.25	1.37
Bilayer Non-Resonant Part					
G Band	1581.56 cm^{-1}	21.65 cm^{-1}	Single Lorentz	—	1.72
2D Band	2678.10 cm^{-1}	39.14 cm^{-1}	Single Lorentz	4.66	2.03

Chapter 6 Synthesis and Optical Spectroscopy Study of 2D TMDCs

6.1 Overview of 2D TMDCs

Transition metal dichalcogenides (TMDCs) are layered materials with form of M-X-M, where M is a transition metal element from group IV (Ti, Zr, Hf and so on), group V (for instance V, Nb or Ta) or group VI (Mo, W and so on), and X is a chalcogen (S, Se or Te). Similar as their carbon counterpart, the strong in-plane bonding and weak out-of-plane interactions enable them to be exfoliated into two-dimensional layers of single unit cell thickness. Differently, a single layer of 2D TMDCs is composed of more than one layer of metal and chalcogen atoms, depending on the stacking orders and metal atom coordination, as shown in Figure 6.1^{36-39, 70}. The overall symmetry of TMDCs can be hexagonal (2H, two layers per repeat unit), rhombohedral (3R, three layers per repeat unit) or tetragonal (1T, one layer per repeat unit), and the metal atoms can have octahedral or trigonal prismatic coordination.

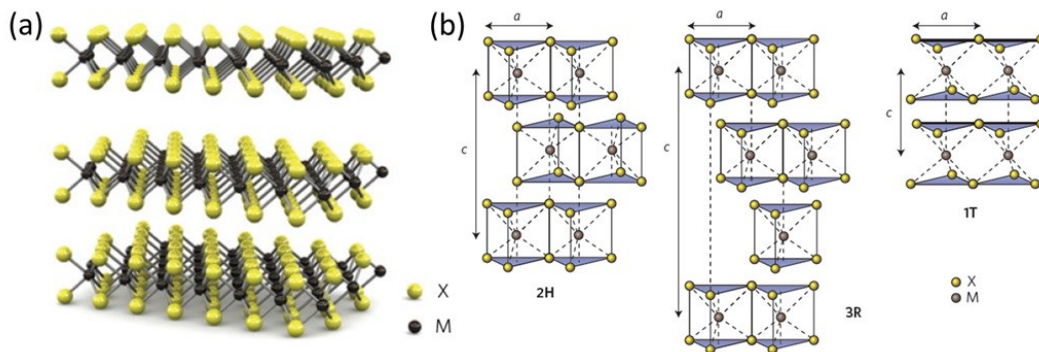


Figure 6.1 (a) 3D representation of typical TMDCs structure, with chalcogen atoms (X) in yellow and metal atoms (M) in grey. (b) Schematic drawings of structural polytypes: 2H (hexagonal symmetry), 3R (rhombohedral symmetry) and 1T (tetragonal symmetry).

Also the electronic properties of TMDCs range from metallic to semiconducting. Among them, MoS₂ and WS₂ as semiconductors, have sizable bandgaps which evolve from indirect to

direct as dimension reduces from bulk to single layers. It's more advantageous than graphene for applications such as transistors, photodetectors and electroluminescent devices. But it should be mentioned that the samples presented in current studies mostly prepared by chemical or mechanical exfoliation from bulk material. And the study of CVD grown 2D MoS₂ and WS₂ still stay at the first page^{36-39, 70}.

6.2 Synthesis of MoS₂ and WS₂ Crystals by Chemical Vapor Deposition

Alike their sibling graphene, atomic layer of TMDC crystals can be isolated from the bulk form using mechanical or chemical exfoliation (Figure 6.2)^{172, 173}. Suffering a low yield and a size limitation, typically in micrometer scale, as-prepared samples can only fit in fundamental studies and proof-of-concept demonstrations, but not in real device applications.

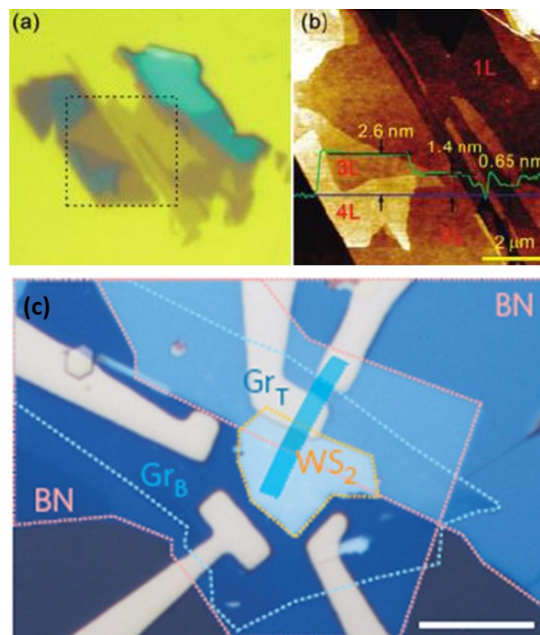


Figure 6.2 Optical (a) and atomic force microscope (AFM) (b) images of exfoliated MoS₂ flake on SiO₂/Si substrate. (c) Optical image of graphene-WS₂ heterotransistor, scale bar 10 μm.

Therefore, great efforts have been devoted to realizing synthesis of 2D MoS₂ and WS₂ crystals by chemical vapor deposition in our group. But considering the major contribution belongs to one of the collaborators, a brief introduction of deposition mechanism and only experimental details relevant with the optical spectroscopy study will be covered here. Different from the transition metal catalytic reactions involved in CVD of graphene, the deposition mechanism of MoS₂ and WS₂ is mainly based on the sulfurization of molybdenum and tungsten or their relative oxides. According to different form of solid precursor applied, the experimental details of MoS₂ and WS₂ growth will be discussed separately.

6.2.1 Synthesis of MoS₂ Crystals

Currently, solid precursors such as Mo, MoO₃, or (NH₄)₂MoS₄ have been employed to achieve 2D growth of MoS₂, in form of either thin film or powders^{174, 175}. With predefined 2D geometry, thin film is favorable to produce large area MoS₂ films. The polycrystalline nature of precursory films will be inherited by as-grown MoS₂ film and the number of layers is not easy to control. Thereby, to accomplish synthesis of single-crystal MoS₂ grains, a strategy starting with sulfur and MoO₃ powders is accommodated in this study¹⁷⁶.

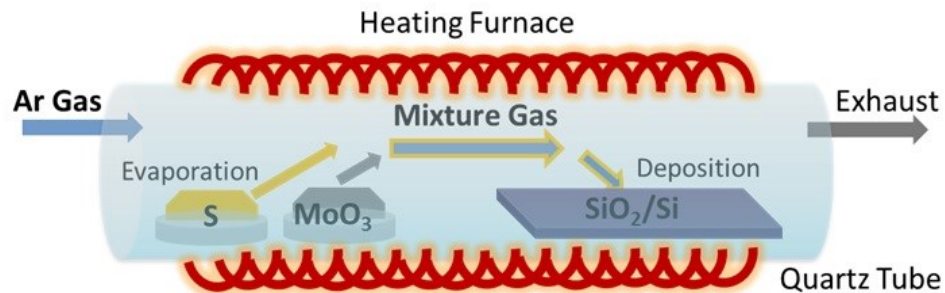


Figure 6.3 Schematic of the CVD system applied for MoS₂ growth in this study.

The MoO₃ powder (0.1 g, Alfa, 99.5%) is placed in an alumina boat and loaded into the center uniform-temperature zone of a conventional horizontal quartz tube furnace, as shown in Figure 6.3. And the sulfur powder (0.4 g, Alfa, 99.5%) is placed in another alumina boat and loaded upstream in a low-temperature zone. Target substrate, Si wafer with 300 nm SiO₂ layer, is put downstream in a separate boat. Before growth, the furnace is evacuated down to ~70 mTorr and back-filled with Ar gas to ambient pressure. In the flow atmosphere of 100 sccm Ar, the furnace is heated to 700 °C at the center zone in 60 min subsequently up to 1100 °C in 130 min. The temperature of the sulfur and the substrate is increased concurrently to ~100 °C and ~700 °C, respectively. After 20 min, the furnace is cooled down naturally to room temperature. As suggested in Ref. 158, this MoO₃ powder based synthesis can be considered as a two-step process. In the first step, MoO₃ powder can be thermally evaporated and reduced by sulfur vapor in gas phase at lower temperature (~650 °C), and the resulting MoO₂ is nucleated on SiO₂/Si substrates. In the second step, when the temperature ramping above ~850 °C, the sulfurization reaction is enacted. This agrees with the observation that the residues, probably MoO₂, deposited on the wall of the quartz tube furnace also contribute to the subsequent MoS₂ growth.

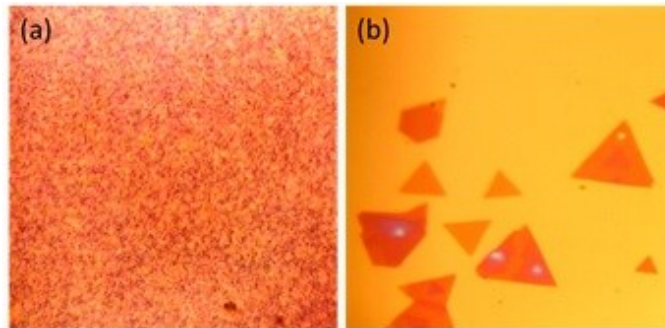


Figure 6.4 Optical microscope images of upstream (a) and downstream (b) part of one MoS₂ sample.

It should be mentioned that the SiO_2/Si substrates used for growth are regularly cut into 1 cm in width and ~ 10 cm in length. The deviations in morphology and thickness of as-deposited MoS_2 crystals are widely observed over this ~ 10 cm span, which are assumed to follow the flow and temperature variation inside the furnace (Figure 6.4).

6.2.2 Synthesis of WS_2 Crystals

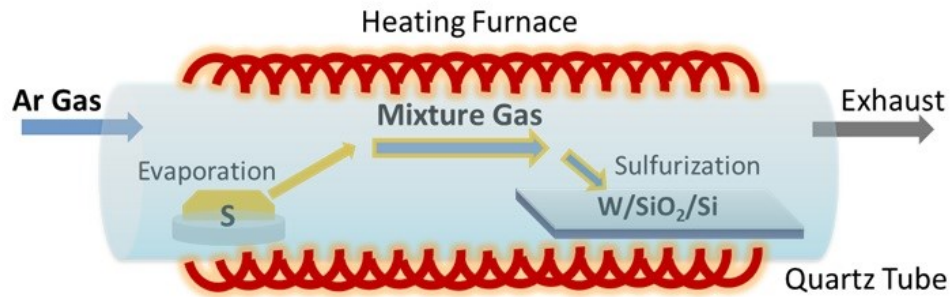


Figure 6.5 Schematic of the CVD system applied for WS_2 growth in this study.

In contrast with synthesis of MoS_2 , tungsten films (1~ 10 nm) are pre-deposited on SiO_2/Si substrates for growth of WS_2 single crystals. Similarly, the W coated substrate is placed in a stainless tube reactor and loaded into the center uniform-temperature zone, while sulfur powder is loaded upstream in a low-temperature zone. The growth is initiated after the evacuation and back-fill step. During the sulfurization, the temperature of the sulfur powder and the substrate are kept at ~ 100 °C and ~ 1000 °C, respectively. And the evaporated S is continuously carried to the downstream by argon and hydrogen flow. The growth is terminated in 30 min and the furnace is cooled down to room temperature in 20 min.

6.3 Optical Spectroscopy Study of MoS_2 and WS_2 Crystals

As demonstrated in chapter 5, Raman spectroscopy is used as a non-destructive method to characterize crystalline quality and thickness of MoS_2 grains. Representative Raman spectra of

SL and bilayer MoS₂ grains are shown in Figure 6.6. For MoS₂ crystals, two characteristic Raman active modes, E_{2g}¹ and A_{1g}, are found. They are associated with the in-plane and out-of-plane vibration of sulfides, respectively. It has been reported that the band frequency difference between E_{2g}¹ and A_{1g} (Δ) can be used to identify the number of MoS₂ layers. As shown in Figure 6.6, for single layer, E_{2g}¹ peak is at 386 cm⁻¹ and A_{1g} peak at 404 cm⁻¹, giving a difference Δ of 18cm⁻¹. While for bilayer, the frequency difference expands to 22 cm⁻¹, with E_{2g}¹ at 385 cm⁻¹ and A_{1g} at 407 cm⁻¹, respectively. Figures 6.7 (a) and (b) show Raman intensity mappings of E_{2g}¹ at 385 cm⁻¹ and A_{1g} at 407 cm⁻¹ of a triangular shape MoS₂ grain, which confirms the thickness and quality uniformity of the CVD grains. A Δ of 22 cm⁻¹ suggests the grain is a bilayer MoS₂ crystal. MoS₂ grains with different shape, triangle and hexagon, have been found in as-prepared samples, however, little difference in Raman features has been discovered, as demonstrated in Figure 6.8.

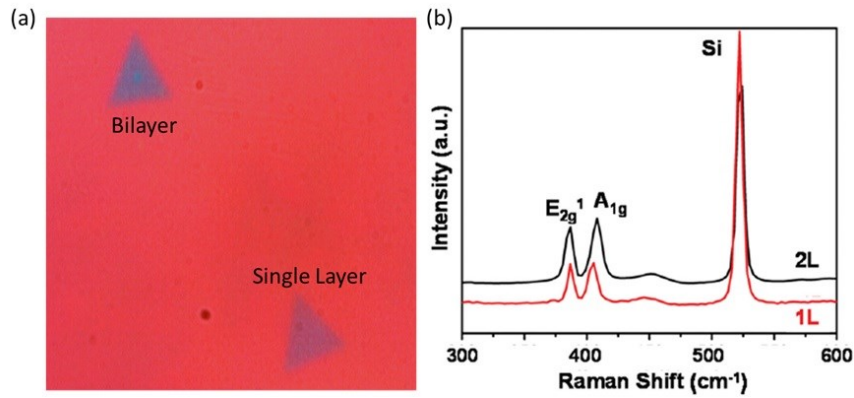


Figure 6.6 Optical microscope image and Raman spectra of typical single-layer and bilayer MoS₂ crystals. The laser excitation wavelength is 532 nm.

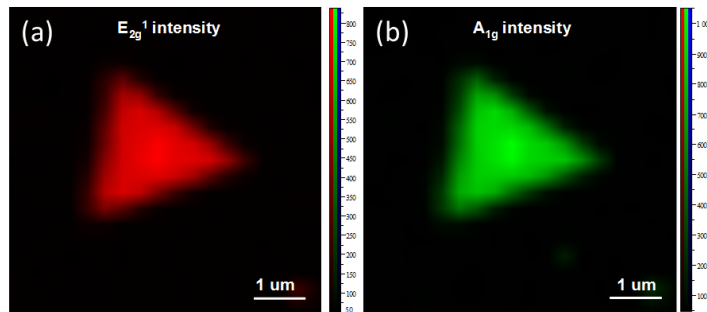


Figure 6.7 Raman intensity mappings of (a) E_{2g}¹ and (b) A_{1g} of a typical bilayer MoS₂ grain.

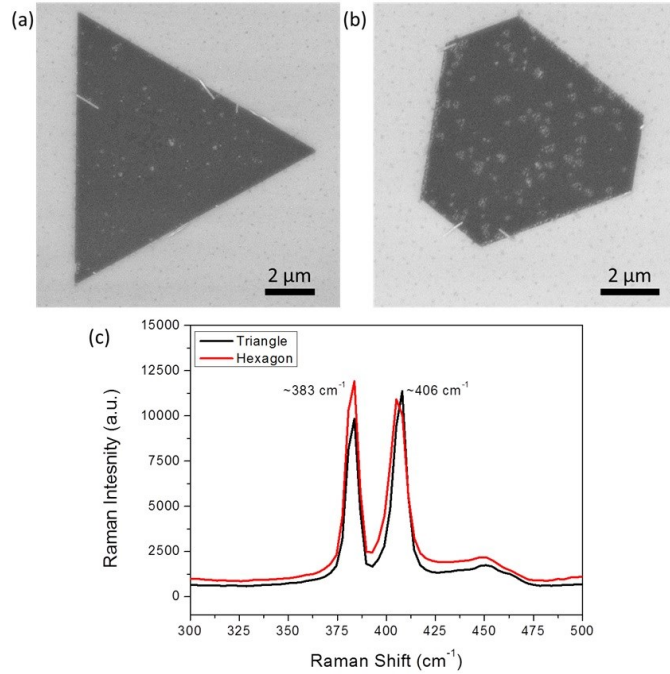


Figure 6.8 SEM images (a-b) and Raman spectra (c) of MoS₂ domains with triangle and hexagon shape.

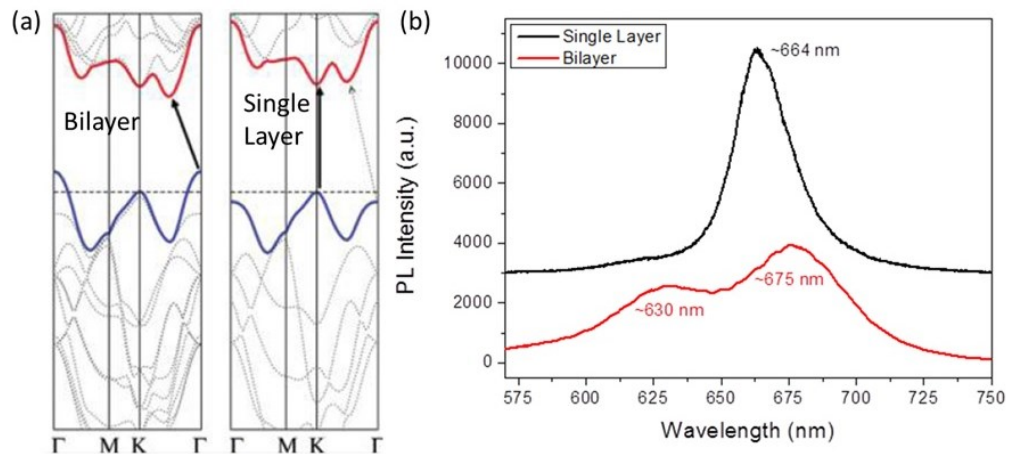


Figure 6.9 (a) Schematic of electronic band structures of single-layer and bilayer MoS₂. (b) Photoluminescence spectra of typical single-layer and bilayer MoS₂ crystals. The laser excitation wavelength is 532 nm.

One of the most peculiar behaviors of 2D MoS₂ is the transform from indirect band gap semiconductor to a one with direct band gap, as illustrated in Figure 6.8 (a)^{177, 178}. Strong photoluminescence (PL) has been expected for single-layer MoS₂, related with the direct transition between conduction and valence bands. In Figure 6.8 (b), PL spectrum of a single-layer

triangle presents a sharp, single peak at 664 nm, while the one of bilayer grain contains two emission bands at 676 nm and 630 nm, known as A1 and B1 direct excitonic transitions, respectively. The PL result is also consistent with recent studies of exfoliated flakes and large-area CVD MoS₂ films¹⁷⁹.

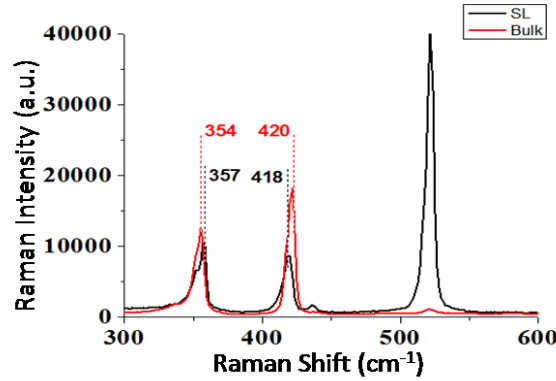


Figure 6.10 Typical Raman spectra of single-layer and bulk WS₂, under 532 nm laser excitation.

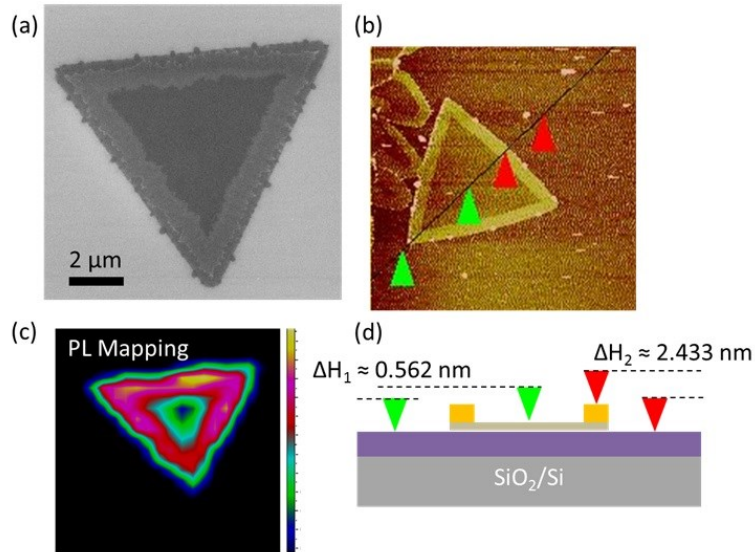


Figure 6.11 SEM (a) and AFM (b) images of WS₂ triangles. (c) Raman mapping of domain in (a), with 532 nm laser excitation. (d) Schematic of thickness distribution across the domain in (b).

Similarly, thickness-dependent Raman difference between E_{2g}¹ and A_{1g} peaks has been witnessed for WS₂ samples (Figure 6.10). However, due to the special morphology, of which edges appear thicker than the inner parts, the photoluminescence of as-synthesized WS₂ domains is under influence of certain edge effects and desires a further investigation (Figure 6.11)¹⁸⁰⁻¹⁸².

Chapter 7 Conclusions and Outlook

In order to synthesize hexagon graphene single crystals, some key factors in chemical vapor deposition, including the catalytic growth mechanism on Cu foil, pretreatment of Cu foil, methane and hydrogen concentration, duration of growth, have been evaluated. It is found that the annealing step of Cu foil prior to the growth is crucial to reduce the nucleation density of graphene, hereby increase the opportunity for growing expansively. And the hydrogen gas play dual roles in the synthesis: it can catalytically assist the methane decomposing and forming active carbon radius, and meanwhile scissor the edge of C-C lattice to expose a zigzag termination. Balancing aforementioned impacts, growth recipes are proposed and have been demonstrated successfully. Over millimeter size monolayer and micrometer size bilayer domains have been achieved in this study with well-defined hexagon shape and good uniformity. Further, these monolayer crystals are manipulated as building blocks to create complex structures, twisted bilayer graphene (tBLGs).

Instead of sophisticated energy spectrum measurements, Raman spectroscopy is employed to characterize the samples synthesized in this study, considering its applicability in both laboratory and mass production. With this fast and non-destructive tool, some characteristic features, revealing structural and electronic properties of monolayer graphene crystals and twisted bilayer graphene domains, have been witnessed and investigated. Especially for twisted bilayer graphene, the underlying relation between the Raman signatures, G resonance, rotation angle dependent folded phonon, and enhancement of 2D has been revealed. A comprehensive imaging of Raman behavior and electronic band structure of twisted bilayer graphene have been created

from a graphene superlattice point of view.

Beyond graphene, synthesis and optical spectral feature of 2D transition metal dichalcogenides, molybdenum disulphide and tungsten disulphide, are also investigated in this dissertation. These fundamental understandings of 2D crystals can serve as stepping stones for further application. More importantly, this study offers valuable experience in manipulating individual atomic layers to construct novel structures, which is predicted as one of the future directions of nano engineering and materials science (Figure 7.1)³⁵.

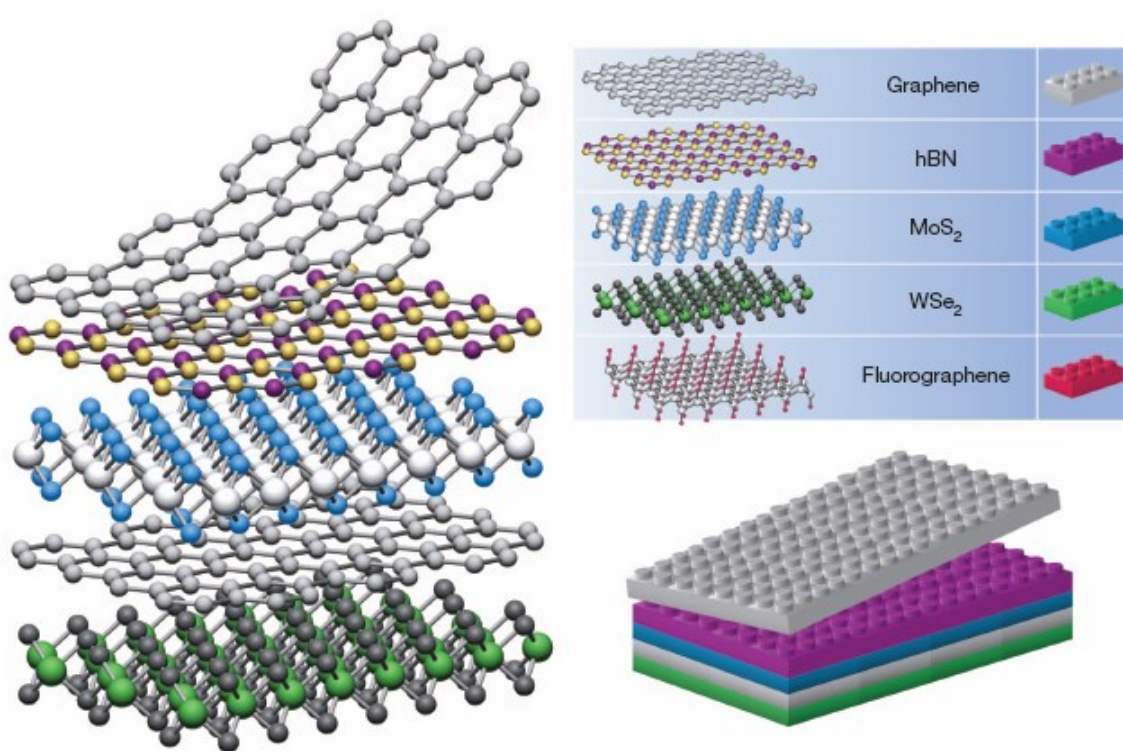


Figure 7.1 Building van der Waals heterostructures with 2D crystals as Lego blocks.

REFERENCE

1. Mas-Balleste, R.; Gomez-Navarro, C.; Gomez-Herrero, J.; Zamora, F. 2D materials: to graphene and beyond. *Nanoscale* 2011, 3, 20-30.
2. Ariga, K.; Li, M.; Richards, G. J.; Hill, J. P. Nanoarchitectonics: A Conceptual Paradigm for Design and Synthesis of Dimension-Controlled Functional Nanomaterials. *Journal of Nanoscience and Nanotechnology* 2011, 11, 1-13.
3. Osada, M.; Sasaki, T. Two-Dimensional Dielectric Nanosheets: Novel Nanoelectronics From Nanocrystal Building Blocks. *Advanced Materials* 2012, 24, 210-228.
4. Loomis, J.; Panchapakesan, B. Dimensional dependence of photomechanical response in carbon nanostructure composites: a case for carbon-based mixed-dimensional systems. *Nanotechnology* 2012, 23.
5. Mermin, N. D.; Wagner, H. ABSENCE OF FERROMAGNETISM OR ANTIFERROMAGNETISM IN ONE- OR 2-DIMENSIONAL ISOTROPIC HEISENBERG MODELS. *Physical Review Letters* 1966, 17, 1133-&.
6. Venables, J. A.; Spiller, G. D. T.; Hanbucken, M. NUCLEATION AND GROWTH OF THIN-FILMS. *Reports on Progress in Physics* 1984, 47, 399-459.
7. Novoselov, K. S.; Geim, A. K.; Morozov, S. V.; Jiang, D.; Zhang, Y.; Dubonos, S. V.; Grigorieva, I. V.; Firsov, A. A. Electric field effect in atomically thin carbon films. *Science* 2004, 306, 666-669.
8. Novoselov, K. S.; Geim, A. K.; Morozov, S. V.; Jiang, D.; Katsnelson, M. I.; Grigorieva, I. V.; Dubonos, S. V.; Firsov, A. A. Two-dimensional gas of massless Dirac fermions in graphene.

Nature 2005, 438, 197-200.

9. Meyer, J. C.; Geim, A. K.; Katsnelson, M. I.; Novoselov, K. S.; Booth, T. J.; Roth, S. The structure of suspended graphene sheets. *Nature* 2007, 446, 60-63.
10. Berger, C.; Song, Z. M.; Li, T. B.; Li, X. B.; Ogbazghi, A. Y.; Feng, R.; Dai, Z. T.; Marchenkov, A. N.; Conrad, E. H.; First, P. N.; de Heer, W. A. Ultrathin epitaxial graphite: 2D electron gas properties and a route toward graphene-based nanoelectronics. *Journal of Physical Chemistry B* 2004, 108, 19912-19916.
11. Marchini, S.; Gunther, S.; Wintterlin, J. Scanning tunneling microscopy of graphene on Ru(0001). *Physical Review B* 2007, 76.
12. Yu, Q. K.; Lian, J.; Siriponglert, S.; Li, H.; Chen, Y. P.; Pei, S. S. Graphene segregated on Ni surfaces and transferred to insulators. *Applied Physics Letters* 2008, 93.
13. Li, X. S.; Cai, W. W.; Colombo, L.; Ruoff, R. S. Evolution of Graphene Growth on Ni and Cu by Carbon Isotope Labeling. *Nano Letters* 2009, 9, 4268-4272.
14. Geim, A. K.; Novoselov, K. S. The rise of graphene. *Nature Materials* 2007, 6, 183-191.
15. Geim, A. K. Graphene: Status and Prospects. *Science* 2009, 324, 1530-1534.
16. Park, S.; Ruoff, R. S. Chemical methods for the production of graphenes. *Nature Nanotechnology* 2009, 4, 217-224.
17. Nair, R. R.; Blake, P.; Grigorenko, A. N.; Novoselov, K. S.; Booth, T. J.; Stauber, T.; Peres, N. M. R.; Geim, A. K. Fine structure constant defines visual transparency of graphene. *Science* 2008, 320, 1308-1308.
18. Balandin, A. A.; Ghosh, S.; Bao, W. Z.; Calizo, I.; Teweldebrhan, D.; Miao, F.; Lau, C. N.

Superior thermal conductivity of single-layer graphene. *Nano Letters* 2008, 8, 902-907.

19. Lee, C.; Wei, X. D.; Kysar, J. W.; Hone, J. Measurement of the elastic properties and intrinsic strength of monolayer graphene. *Science* 2008, 321, 385-388.

20. Zhu, Y. W.; Murali, S.; Cai, W. W.; Li, X. S.; Suk, J. W.; Potts, J. R.; Ruoff, R. S. Graphene and Graphene Oxide: Synthesis, Properties, and Applications. *Advanced Materials* 2010, 22, 3906-3924.

21. Guo, S. J.; Dong, S. J. Graphene nanosheet: synthesis, molecular engineering, thin film, hybrids, and energy and analytical applications. *Chemical Society Reviews* 2011, 40, 2644-2672.

22. Huang, X.; Yin, Z. Y.; Wu, S. X.; Qi, X. Y.; He, Q. Y.; Zhang, Q. C.; Yan, Q. Y.; Boey, F.; Zhang, H. Graphene-Based Materials: Synthesis, Characterization, Properties, and Applications. *Small* 2011, 7, 1876-1902.

23. Schwierz, F. Graphene transistors. *Nature Nanotechnology* 2010, 5, 487-496.

24. Chen, D.; Tang, L. H.; Li, J. H. Graphene-based materials in electrochemistry. *Chemical Society Reviews* 2010, 39, 3157-3180.

25. Kim, K.; Choi, J. Y.; Kim, T.; Cho, S. H.; Chung, H. J. A role for graphene in silicon-based semiconductor devices. *Nature* 2011, 479, 338-344.

26. Balandin, A. A. Thermal properties of graphene and nanostructured carbon materials. *Nature Materials* 2011, 10, 569-581.

27. Shao, Y. Y.; Wang, J.; Wu, H.; Liu, J.; Aksay, I. A.; Lin, Y. H. Graphene Based Electrochemical Sensors and Biosensors: A Review. *Electroanalysis* 2010, 22, 1027-1036.

28. He, Q. Y.; Wu, S. X.; Yin, Z. Y.; Zhang, H. Graphene-based electronic sensors. *Chemical*

Science 2012, 3, 1764-1772.

29. Xiang, Q. J.; Yu, J. G.; Jaroniec, M. Graphene-based semiconductor photocatalysts.

Chemical Society Reviews 2012, 41, 782-796.

30. Bonaccorso, F.; Sun, Z.; Hasan, T.; Ferrari, A. C. Graphene photonics and optoelectronics.

Nature Photonics 2010, 4, 611-622.

31. Grigorenko, A. N.; Polini, M.; Novoselov, K. S. Graphene plasmonics. *Nature Photonics*

2012, 6, 749-758.

32. Bao, Q. L.; Loh, K. P. Graphene Photonics, Plasmonics, and Broadband Optoelectronic

Devices. *Acs Nano* 2012, 6, 3677-3694.

33. Hu, Y. H.; Wang, H.; Hu, B. Thinnest Two-Dimensional Nanomaterial-Graphene for Solar

Energy. *Chemsuschem* 2010, 3, 782-796.

34. Brownson, D. A. C.; Kampouris, D. K.; Banks, C. E. An overview of graphene in energy

production and storage applications. *Journal of Power Sources* 2011, 196, 4873-4885.

35. Geim, A. K.; Grigorieva, I. V. Van der Waals heterostructures. *Nature* 2013, 499, 419-425.

36. Xu, M. S.; Liang, T.; Shi, M. M.; Chen, H. Z. Graphene-Like Two-Dimensional Materials.

Chemical Reviews 2013, 113, 3766-3798.

37. Novoselov, K. S.; Jiang, D.; Schedin, F.; Booth, T. J.; Khotkevich, V. V.; Morozov, S. V.;

Geim, A. K. Two-dimensional atomic crystals. *Proceedings of the National Academy of Sciences*

of the United States of America 2005, 102, 10451-10453.

38. Wang, Q. H.; Kalantar-Zadeh, K.; Kis, A.; Coleman, J. N.; Strano, M. S. Electronics and

optoelectronics of two-dimensional transition metal dichalcogenides. *Nature Nanotechnology*

2012, 7, 699-712.

39. Butler, S. Z.; Hollen, S. M.; Cao, L. Y.; Cui, Y.; Gupta, J. A.; Gutierrez, H. R.; Heinz, T. F.; Hong, S. S.; Huang, J. X.; Ismach, A. F.; Johnston-Halperin, E.; Kuno, M.; Plashnitsa, V. V.; Robinson, R. D.; Ruoff, R. S.; Salahuddin, S.; Shan, J.; Shi, L.; Spencer, M. G.; Terrones, M.; Windl, W.; Goldberger, J. E. Progress, Challenges, and Opportunities in Two-Dimensional Materials Beyond Graphene. *Acs Nano* 2013, 7, 2898-2926.
40. McCann, E.; Koshino, M. The electronic properties of bilayer graphene. *Reports on Progress in Physics* 2013, 76.
41. Li, G. H.; Luican, A.; Andrei, E. Y. Scanning Tunneling Spectroscopy of Graphene on Graphite. *Physical Review Letters* 2009, 102.
42. Malard, L. M.; Pimenta, M. A.; Dresselhaus, G.; Dresselhaus, M. S. Raman spectroscopy in graphene. *Physics Reports-Review Section of Physics Letters* 2009, 473, 51-87.
43. Li, G. H.; Luican, A.; dos Santos, J.; Neto, A. H. C.; Reina, A.; Kong, J.; Andrei, E. Y. Observation of Van Hove singularities in twisted graphene layers. *Nature Physics* 2010, 6, 109-113.
44. Andrei, E. Y.; Li, G. H.; Du, X. Electronic properties of graphene: a perspective from scanning tunneling microscopy and magnetotransport. *Reports on Progress in Physics* 2012, 75.
45. Huang, P. Y.; Meyer, J. C.; Muller, D. A. From atoms to grains: Transmission electron microscopy of graphene. *Mrs Bulletin* 2012, 37, 1214-1221.
46. Robertson, A. W.; Warner, J. H. Atomic resolution imaging of graphene by transmission electron microscopy. *Nanoscale* 2013, 5, 4079-4093.

47. Irene Lee. Electronic Structure and Bonding.

http://wps.prenhall.com/wps/media/objects/724/741576/chapter_01.html.

48. Wilson, M. Electrons in atomically thin carbon sheets behave like massless particles. *Physics Today* 2006, 59, 21-23.

49. Yan, Z.; Lin, J.; Peng, Z.; Sun, Z.; Zhu, Y.; Li, L.; Xiang, C.; Samuel, E. L.; Kittrell, C.; Tour, J. M. Toward the Synthesis of Wafer-Scale Single-Crystal Graphene on Copper Foils. *Acs Nano* 2012, 6, 9110-9117.

50. Zhou, H.; Yu, W. J.; Liu, L.; Cheng, R.; Chen, Y.; Huang, X.; Liu, Y.; Wang, Y.; Huang, Y.; Duan, X. Chemical vapour deposition growth of large single crystals of monolayer and bilayer graphene. *Nature Communications* 2013, 4.

51. Chen, S.; Ji, H.; Chou, H.; Li, Q.; Li, H.; Suk, J. W.; Piner, R.; Liao, L.; Cai, W.; Ruoff, R. S. Millimeter-Size Single-Crystal Graphene by Suppressing Evaporative Loss of Cu During Low Pressure Chemical Vapor Deposition. *Advanced Materials* 2013, 25, 2062-2065.

52. Mohsin, A.; Liu, L.; Liu, P.; Deng, W.; Ivanov, I. N.; Li, G.; Dyck, O. E.; Duscher, G.; Dunlap, J. R.; Xiao, K.; Gu, G. Synthesis of Millimeter-Size Hexagon-Shaped Graphene Single Crystals on Resolidified Copper. *Acs Nano* 2013, 7, 8924-8931.

53. Hao, Y.; Bharathi, M. S.; Wang, L.; Liu, Y.; Chen, H.; Nie, S.; Wang, X.; Chou, H.; Tan, C.; Fallahzad, B.; Ramanarayan, H.; Magnuson, C. W.; Tutuc, E.; Yakobson, B. I.; McCarty, K. F.; Zhang, Y.-W.; Kim, P.; Hone, J.; Colombo, L.; Ruoff, R. S. The Role of Surface Oxygen in the Growth of Large Single-Crystal Graphene on Copper. *Science* 2013, 342, 720-723.

54. Gan, L.; Luo, Z. Turning off Hydrogen To Realize Seeded Growth of Subcentimeter

- Single-Crystal Graphene Grains on Copper. *Acs Nano* 2013, 7, 9480-9488.
55. Ohta, T.; Bostwick, A.; Seyller, T.; Horn, K.; Rotenberg, E. Controlling the electronic structure of bilayer graphene. *Science* 2006, 313, 951-954.
56. Castro, E. V.; Novoselov, K. S.; Morozov, S. V.; Peres, N. M. R.; Dos Santos, J. M. B. L.; Nilsson, J.; Guinea, F.; Geim, A. K.; Neto, A. H. C. Biased bilayer graphene: Semiconductor with a gap tunable by the electric field effect. *Physical Review Letters* 2007, 99.
57. Oostinga, J. B.; Heersche, H. B.; Liu, X.; Morpurgo, A. F.; Vandersypen, L. M. K. Gate-induced insulating state in bilayer graphene devices. *Nature Materials* 2008, 7, 151-157.
58. dos Santos, J. M. B. L.; Peres, N. M. R.; Castro Neto, A. H. Graphene bilayer with a twist: Electronic structure. *Physical Review Letters* 2007, 99.
59. Lu, C.-C.; Lin, Y.-C.; Liu, Z.; Yeh, C.-H.; Suenaga, K.; Chiu, P.-W. Twisting Bilayer Graphene Superlattices. *Acs Nano* 2013, 7, 2587-2594.
60. Luican, A.; Li, G. H.; Reina, A.; Kong, J.; Nair, R. R.; Novoselov, K. S.; Geim, A. K.; Andrei, E. Y. Single-Layer Behavior and Its Breakdown in Twisted Graphene Layers. *Physical Review Letters* 2011, 106.
61. Ni, Z. H.; Wang, Y. Y.; Yu, T.; You, Y. M.; Shen, Z. X. Reduction of Fermi velocity in folded graphene observed by resonance Raman spectroscopy. *Physical Review B* 2008, 77.
62. Havener, R. W.; Zhuang, H. L.; Brown, L.; Hennig, R. G.; Park, J. Angle-Resolved Raman Imaging of Inter layer Rotations and Interactions in Twisted Bilayer Graphene. *Nano Letters* 2012, 12, 3162-3167.
63. Kim, K.; Coh, S.; Tan, L. Z.; Regan, W.; Yuk, J. M.; Chatterjee, E.; Crommie, M. F.; Cohen,

- M. L.; Louie, S. G.; Zettl, A. Raman Spectroscopy Study of Rotated Double-Layer Graphene: Misorientation-Angle Dependence of Electronic Structure. *Physical Review Letters* 2012, 108.
64. Righi, A.; Costa, S. D.; Chacham, H.; Fantini, C.; Venezuela, P.; Magnuson, C.; Colombo, L.; Bacsa, W. S.; Ruoff, R. S.; Pimenta, M. A. Graphene Moire patterns observed by umklapp double-resonance Raman scattering. *Physical Review B* 2011, 84.
65. Ni, Z. H.; Liu, L.; Wang, Y. Y.; Zheng, Z.; Li, L. J.; Yu, T.; Shen, Z. X. G-band Raman double resonance in twisted bilayer graphene: Evidence of band splitting and folding. *Physical Review B* 2009, 80.
66. Nie, S.; Wu, W.; Xing, S. R.; Yu, Q. K.; Bao, J. M.; Pei, S. S.; McCarty, K. F. Growth from below: bilayer graphene on copper by chemical vapor deposition. *New Journal of Physics* 2012, 14.
67. Rao, C. N. R.; Sood, A. K.; Subrahmanyam, K. S.; Govindaraj, A. Graphene: The New Two-Dimensional Nanomaterial. *Angewandte Chemie-International Edition* 2009, 48, 7752-7777.
68. Singh, V.; Joung, D.; Zhai, L.; Das, S.; Khondaker, S. I.; Seal, S. Graphene based materials: Past, present and future. *Progress in Materials Science* 2011, 56, 1178-1271.
69. Novoselov, K. S.; Fal'ko, V. I.; Colombo, L.; Gellert, P. R.; Schwab, M. G.; Kim, K. A roadmap for graphene. *Nature* 2012, 490, 192-200.
70. Bonaccorso, F.; Lombardo, A.; Hasan, T.; Sun, Z. P.; Colombo, L.; Ferrari, A. C. Production and processing of graphene and 2d crystals. *Materials Today* 2012, 15, 564-589.
71. Edwards, R. S.; Coleman, K. S. Graphene synthesis: relationship to applications. *Nanoscale*

2013, 5, 38-51.

72. Yan, Z.; Lin, J.; Peng, Z. W.; Sun, Z. Z.; Zhu, Y.; Li, L.; Xiang, C. S.; Samuel, E. L.; Kittrell, C.; Tour, J. M. Toward the Synthesis of Wafer-Scale Single-Crystal Graphene on Copper Foils. *Acs Nano* 2012, 6, 9110-9117.

73. Zhou, H. L.; Yu, W. J.; Liu, L. X.; Cheng, R.; Chen, Y.; Huang, X. Q.; Liu, Y.; Wang, Y.; Huang, Y.; Duan, X. F. Chemical vapour deposition growth of large single crystals of monolayer and bilayer graphene. *Nature Communications* 2013, 4.

74. Chen, S. S.; Ji, H. X.; Chou, H.; Li, Q. Y.; Li, H. Y.; Suk, J. W.; Piner, R.; Liao, L.; Cai, W. W.; Ruoff, R. S. Millimeter-Size Single-Crystal Graphene by Suppressing Evaporative Loss of Cu During Low Pressure Chemical Vapor Deposition. *Advanced Materials* 2013, 25, 2062-2065.

75. Mohsin, A.; Liu, L.; Liu, P. Z.; Deng, W.; Ivanov, I. N.; Li, G. L.; Dyck, O. E.; Duscher, G.; Dunlap, J. R.; Xiao, K.; Gu, G. Synthesis of Millimeter-Size Hexagon-Shaped Graphene Single Crystals on Resolidified Copper. *Acs Nano* 2013, 7, 8924-8931.

76. Hao, Y. F.; Bharathi, M. S.; Wang, L.; Liu, Y. Y.; Chen, H.; Nie, S.; Wang, X. H.; Chou, H.; Tan, C.; Fallahazad, B.; Ramanarayan, H.; Magnuson, C. W.; Tutuc, E.; Yakobson, B. I.; McCarty, K. F.; Zhang, Y. W.; Kim, P.; Hone, J.; Colombo, L.; Ruoff, R. S. The Role of Surface Oxygen in the Growth of Large Single-Crystal Graphene on Copper. *Science* 2013, 342, 720-723.

77. Gan, L.; Luo, Z. T. Turning off Hydrogen To Realize Seeded Growth of Subcentimeter Single-Crystal Graphene Grains on Copper. *Acs Nano* 2013, 7, 9480-9488.

78. Bae, S.; Kim, H.; Lee, Y.; Xu, X. F.; Park, J. S.; Zheng, Y.; Balakrishnan, J.; Lei, T.; Kim, H. R.; Song, Y. I.; Kim, Y. J.; Kim, K. S.; Ozyilmaz, B.; Ahn, J. H.; Hong, B. H.; Iijima, S.

Roll-to-roll production of 30-inch graphene films for transparent electrodes. *Nature Nanotechnology* 2010, 5, 574-578.

79. Graphene Supermarket. <https://graphene-supermarket.com/>.

80. Blake, P.; Hill, E. W.; Neto, A. H. C.; Novoselov, K. S.; Jiang, D.; Yang, R.; Booth, T. J.; Geim, A. K. Making graphene visible. *Applied Physics Letters* 2007, 91.

81. Van Noorden, R. PRODUCTION Beyond sticky tape. *Nature* 2012, 483, S32-S33.

82. Coleman, J. N. Liquid-Phase Exfoliation of Nanotubes and Graphene. *Advanced Functional Materials* 2009, 19, 3680-3695.

83. Cui, X.; Zhang, C. Z.; Hao, R.; Hou, Y. L. Liquid-phase exfoliation, functionalization and applications of graphene. *Nanoscale* 2011, 3, 2118-2126.

84. Coleman, J. N. Liquid Exfoliation of Defect-Free Graphene. *Accounts of Chemical Research* 2013, 46, 14-22.

85. Ciesielski, A.; Samori, P. Graphene via sonication assisted liquid-phase exfoliation. *Chemical Society Reviews* 2014, 43, 381-398.

86. Stankovich, S.; Dikin, D. A.; Dommett, G. H. B.; Kohlhaas, K. M.; Zimney, E. J.; Stach, E. A.; Piner, R. D.; Nguyen, S. T.; Ruoff, R. S. Graphene-based composite materials. *Nature* 2006, 442, 282-286.

87. Fan, X. B.; Peng, W. C.; Li, Y.; Li, X. Y.; Wang, S. L.; Zhang, G. L.; Zhang, F. B. Deoxygenation of Exfoliated Graphite Oxide under Alkaline Conditions: A Green Route to Graphene Preparation. *Advanced Materials* 2008, 20, 4490-4493.

88. Eda, G.; Chhowalla, M. Chemically Derived Graphene Oxide: Towards Large-Area

- Thin-Film Electronics and Optoelectronics. *Advanced Materials* 2010, 22, 2392-2415.
89. Compton, O. C.; Nguyen, S. T. Graphene Oxide, Highly Reduced Graphene Oxide, and Graphene: Versatile Building Blocks for Carbon-Based Materials. *Small* 2010, 6, 711-723.
90. Chua, C. K.; Pumera, M. Chemical reduction of graphene oxide: a synthetic chemistry viewpoint. *Chemical Society Reviews* 2014, 43, 291-312.
91. Li, C. X.; Adamcik, J.; Mezzenga, R. Biodegradable nanocomposites of amyloid fibrils and graphene with shape-memory and enzyme-sensing properties. *Nature Nanotechnology* 2012, 7, 421-427.
92. de Heer, W. A.; Berger, C.; Wu, X. S.; First, P. N.; Conrad, E. H.; Li, X. B.; Li, T. B.; Sprinkle, M.; Hass, J.; Sadowski, M. L.; Potemski, M.; Martinez, G. Epitaxial graphene. *Solid State Commun.* 2007, 143, 92-100.
93. Seyller, T.; Bostwick, A.; Emtsev, K. V.; Horn, K.; Ley, L.; McChesney, J. L.; Ohta, T.; Riley, J. D.; Rotenberg, E.; Speck, F. Epitaxial graphene: a new material. *Physica Status Solidi B-Basic Solid State Physics* 2008, 245, 1436-1446.
94. Hass, J.; de Heer, W. A.; Conrad, E. H. The growth and morphology of epitaxial multilayer graphene. *Journal of Physics-Condensed Matter* 2008, 20.
95. Emtsev, K. V.; Bostwick, A.; Horn, K.; Jobst, J.; Kellogg, G. L.; Ley, L.; McChesney, J. L.; Ohta, T.; Reshanov, S. A.; Rohrl, J.; Rotenberg, E.; Schmid, A. K.; Waldmann, D.; Weber, H. B.; Seyller, T. Towards wafer-size graphene layers by atmospheric pressure graphitization of silicon carbide. *Nature Materials* 2009, 8, 203-207.
96. Unarunotai, S.; Murata, Y.; Chialvo, C. E.; Kim, H. S.; MacLaren, S.; Mason, N.; Petrov, I.

- Rogers, J. A. Transfer of graphene layers grown on SiC wafers to other substrates and their integration into field effect transistors. *Applied Physics Letters* 2009, 95.
97. Lee, Y.; Bae, S.; Jang, H.; Jang, S.; Zhu, S. E.; Sim, S. H.; Song, Y. I.; Hong, B. H.; Ahn, J. H. Wafer-Scale Synthesis and Transfer of Graphene Films. *Nano Letters* 2010, 10, 490-493.
98. Yan, Z.; Peng, Z. W.; Tour, J. M. Chemical Vapor Deposition of Graphene Single Crystals. *Accounts of Chemical Research* 2014, 47, 1327-1337.
99. Sutter, P.; Sadowski, J. T.; Sutter, E. Graphene on Pt(111): Growth and substrate interaction. *Physical Review B* 2009, 80.
100. Sutter, P. W.; Flege, J. I.; Sutter, E. A. Epitaxial graphene on ruthenium. *Nature Materials* 2008, 7, 406-411.
101. Coraux, J.; N'Diaye, A. T.; Busse, C.; Michely, T. Structural coherency of graphene on Ir(111). *Nano Letters* 2008, 8, 565-570.
102. Coraux, J.; N'Diaye, A. T.; Engler, M.; Busse, C.; Wall, D.; Buckanie, N.; Heringdorf, F.; van Gastel, R.; Poelsema, B.; Michely, T. Growth of graphene on Ir(111). *New Journal of Physics* 2009, 11.
103. Ago, H.; Ito, Y.; Mizuta, N.; Yoshida, K.; Hu, B.; Orofeo, C. M.; Tsuji, M.; Ikeda, K.; Mizuno, S. Epitaxial Chemical Vapor Deposition Growth of Single-Layer Graphene over Cobalt Film Crystallized on Sapphire. *Acs Nano* 2010, 4, 7407-7414.
104. Li, X. S.; Cai, W. W.; An, J. H.; Kim, S.; Nah, J.; Yang, D. X.; Piner, R.; Velamakanni, A.; Jung, I.; Tutuc, E.; Banerjee, S. K.; Colombo, L.; Ruoff, R. S. Large-Area Synthesis of High-Quality and Uniform Graphene Films on Copper Foils. *Science* 2009, 324, 1312-1314.

105. Wintterlin, J.; Bocquet, M. L. Graphene on metal surfaces. *Surface Science* 2009, 603, 1841-1852.
106. Edwards, R. S.; Coleman, K. S. Graphene Film Growth on Polycrystalline Metals. *Accounts of Chemical Research* 2013, 46, 23-30.
107. Tsen, A. W.; Brown, L.; Havener, R. W.; Park, J. Polycrystallinity and Stacking in CVD Graphene. *Accounts of Chemical Research* 2013, 46, 2286-2296.
108. Huang, P. Y.; Ruiz-Vargas, C. S.; van der Zande, A. M.; Whitney, W. S.; Levendorf, M. P.; Kevek, J. W.; Garg, S.; Alden, J. S.; Hustedt, C. J.; Zhu, Y.; Park, J.; McEuen, P. L.; Muller, D. A. Grains and grain boundaries in single-layer graphene atomic patchwork quilts. *Nature* 2011, 469, 389-+.
109. Biro, L. P.; Lambin, P. Grain boundaries in graphene grown by chemical vapor deposition. *New Journal of Physics* 2013, 15.
110. Batzill, M. The surface science of graphene: Metal interfaces, CVD synthesis, nanoribbons, chemical modifications, and defects. *Surface Science Reports* 2012, 67, 83-115.
111. Munoz, R.; Gomez-Aleixandre, C. Review of CVD Synthesis of Graphene. *Chemical Vapor Deposition* 2013, 19, 297-322.
112. Seah, C. M.; Chai, S. P.; Mohamed, A. R. Mechanisms of graphene growth by chemical vapour deposition on transition metals. *Carbon* 2014, 70, 1-21.
113. Frank, O.; Kavan, L.; Kalbac, M. Carbon isotope labelling in graphene research. *Nanoscale* 2014, 6, 6363-6370.
114. Mattevi, C.; Kim, H.; Chhowalla, M. A review of chemical vapour deposition of graphene on

copper. *Journal of Materials Chemistry* 2011, 21, 3324-3334.

115. Wu, Y. P.; Hao, Y. F.; Jeong, H. Y.; Lee, Z.; Chen, S. S.; Jiang, W.; Wu, Q. Z.; Piner, R. D.; Kang, J. Y.; Ruoff, R. S. Crystal Structure Evolution of Individual Graphene Islands During CVD Growth on Copper Foil. *Advanced Materials* 2013, 25, 6744-6751.

116. Jacobberger, R. M.; Arnold, M. S. Graphene Growth Dynamics on Epitaxial Copper Thin Films. *Chemistry of Materials* 2013, 25, 871-877.

117. Han, G. H.; Gunes, F.; Bae, J. J.; Kim, E. S.; Chae, S. J.; Shin, H. J.; Choi, J. Y.; Pribat, D.; Lee, Y. H. Influence of Copper Morphology in Forming Nucleation Seeds for Graphene Growth. *Nano Letters* 2011, 11, 4144-4148.

118. Wu, W. Synthesis of graphene by chemical vapor deposition and its application in electronics and sensing. University of Houston, Houston, 2011.

119. Luo, Z. T.; Lu, Y.; Singer, D. W.; Berck, M. E.; Somers, L. A.; Goldsmith, B. R.; Johnson, A. T. C. Effect of Substrate Roughness and Feedstock Concentration on Growth of Wafer-Scale Graphene at Atmospheric Pressure. *Chemistry of Materials* 2011, 23, 1441-1447.

120. Fan, L. L.; Zou, J.; Li, Z.; Li, X.; Wang, K. L.; Wei, J. Q.; Zhong, M. L.; Wu, D. H.; Xu, Z. P.; Zhu, H. W. Topology evolution of graphene in chemical vapor deposition, a combined theoretical/experimental approach toward shape control of graphene domains. *Nanotechnology* 2012, 23.

121. Murdock, A. T.; Koos, A.; Ben Britton, T.; Houben, L.; Batten, T.; Zhang, T.; Wilkinson, A. J.; Dunin-Borkowski, R. E.; Lekka, C. E.; Grobert, N. Controlling the Orientation, Edge Geometry, and Thickness of Chemical Vapor Deposition Graphene. *Acs Nano* 2013, 7,

1351-1359.

122. Frank, O.; Vejpravova, J.; Holy, V.; Kavan, L.; Kalbac, M. Interaction between graphene and copper substrate: The role of lattice orientation. *Carbon* 2014, 68, 440-451.

123. Ago, H.; Ogawa, Y.; Tsuji, M.; Mizuno, S.; Hibino, H. Catalytic Growth of Graphene: Toward Large-Area Single-Crystalline Graphene. *Journal of Physical Chemistry Letters* 2012, 3, 2228-2236.

124. Dhingra, S.; Hsu, J. F.; Vlassioug, I.; D'Urso, B. Chemical vapor deposition of graphene on large-domain ultra-flat copper. *Carbon* 2014, 69, 188-193.

125. Wood, J. D.; Schmucker, S. W.; Lyons, A. S.; Pop, E.; Lyding, J. W. Effects of Polycrystalline Cu Substrate on Graphene Growth by Chemical Vapor Deposition. *Nano Letters* 2011, 11, 4547-4554.

126. Vlassioug, I.; Regmi, M.; Fulvio, P. F.; Dai, S.; Datskos, P.; Eres, G.; Smirnov, S. Role of Hydrogen in Chemical Vapor Deposition Growth of Large Single-Crystal Graphene. *Acs Nano* 2011, 5, 6069-6076.

127. Wu, B.; Geng, D. C.; Guo, Y. L.; Huang, L. P.; Xue, Y. Z.; Zheng, J.; Chen, J. Y.; Yu, G.; Liu, Y. Q.; Jiang, L.; Hu, W. P. Equiangular Hexagon-Shape-Controlled Synthesis of Graphene on Copper Surface. *Advanced Materials* 2011, 23, 3522-+.

128. Vlassioug, I.; Smirnov, S.; Regmi, M.; Surwade, S. P.; Srivastava, N.; Feenstra, R.; Eres, G.; Parish, C.; Lavrik, N.; Datskos, P.; Dai, S.; Fulvio, P. Graphene Nucleation Density on Copper: Fundamental Role of Background Pressure. *Journal of Physical Chemistry C* 2013, 117, 18919-18926.

129. Fan, L.; Li, Z.; Li, X.; Wang, K.; Zhong, M.; Wei, J.; Wu, D.; Zhu, H. Controllable growth of shaped graphene domains by atmospheric pressure chemical vapour deposition. *Nanoscale* 2011, 3, 4946-4950.
130. Bonaccorso, F.; Lombardo, A.; Hasan, T.; Sun, Z.; Colombo, L.; Ferrari, A. C. Production and processing of graphene and 2d crystals. *Materials Today* 2012, 15, 564-589.
131. Kang, J.; Shin, D.; Bae, S.; Hong, B. H. Graphene transfer: key for applications. *Nanoscale* 2012, 4, 5527-5537.
132. Jia, C.; Jiang, J.; Gan, L.; Guo, X. Direct optical characterization of graphene growth and domains on growth substrates. *Scientific Reports* 2012, 2.
133. Kim, K. S.; Zhao, Y.; Jang, H.; Lee, S. Y.; Kim, J. M.; Kim, K. S.; Ahn, J.-H.; Kim, P.; Choi, J.-Y.; Hong, B. H. Large-scale pattern growth of graphene films for stretchable transparent electrodes. *Nature* 2009, 457, 706-710.
134. Wang, Y.; Zheng, Y.; Xu, X.; Dubuisson, E.; Bao, Q.; Lu, J.; Loh, K. P. Electrochemical delamination of CVD-grown graphene film: toward the recyclable use of copper catalyst. *ACS Nano* 2011, 5, 9927-9933.
135. Lock, E. H.; Baraket, M.; Laskoski, M.; Mulvaney, S. P.; Lee, W. K.; Sheehan, P. E.; Hines, D. R.; Robinson, J. T.; Tosado, J.; Fuhrer, M. S. High-quality uniform dry transfer of graphene to polymers. *Nano Letters* 2011, 12, 102-107.
136. Yoon, T.; Shin, W. C.; Kim, T. Y.; Mun, J. H.; Kim, T.-S.; Cho, B. J. Direct measurement of adhesion energy of monolayer graphene as-grown on copper and its application to renewable transfer process. *Nano Letters* 2012, 12, 1448-1452.

137. Koenig, S. P.; Boddeti, N. G.; Dunn, M. L.; Bunch, J. S. Ultrastrong adhesion of graphene membranes. *Nature Nanotechnology* 2011, 6, 543-546.
138. Kang, S. J.; Kim, B.; Kim, K. S.; Zhao, Y.; Chen, Z.; Lee, G. H.; Hone, J.; Kim, P.; Nuckolls, C. Inking Elastomeric Stamps with Micro-Patterned, Single Layer Graphene to Create High-Performance OFETs. *Advanced Materials* 2011, 23, 3531-3535.
139. Bie, Y. Q.; Zhou, Y. B.; Liao, Z. M.; Yan, K.; Liu, S.; Zhao, Q.; Kumar, S.; Wu, H. C.; Duesberg, G. S.; Cross, G. L. Site-Specific Transfer-Printing of Individual Graphene Microscale Patterns to Arbitrary Surfaces. *Advanced Materials* 2011, 23, 3938-3943.
140. Song, J.; Kam, F.-Y.; Png, R.-Q.; Seah, W.-L.; Zhuo, J.-M.; Lim, G.-K.; Ho, P. K.; Chua, L.-L. A general method for transferring graphene onto soft surfaces. *Nature Nanotechnology* 2013, 8, 356-362.
141. Reina, A.; Jia, X.; Ho, J.; Nezich, D.; Son, H.; Bulovic, V.; Dresselhaus, M. S.; Kong, J. Large area, few-layer graphene films on arbitrary substrates by chemical vapor deposition. *Nano Letters* 2008, 9, 30-35.
142. Li, X.; Cai, W.; An, J.; Kim, S.; Nah, J.; Yang, D.; Piner, R.; Velamakanni, A.; Jung, I.; Tutuc, E. Large-area synthesis of high-quality and uniform graphene films on copper foils. *Science* 2009, 324, 1312-1314.
143. Li, X.; Zhu, Y.; Cai, W.; Borysiak, M.; Han, B.; Chen, D.; Piner, R. D.; Colombo, L.; Ruoff, R. S. Transfer of large-area graphene films for high-performance transparent conductive electrodes. *Nano Letters* 2009, 9, 4359-4363.
144. Suk, J. W.; Kitt, A.; Magnuson, C. W.; Hao, Y.; Ahmed, S.; An, J.; Swan, A. K.; Goldberg, B.

B.; Ruoff, R. S. Transfer of CVD-grown monolayer graphene onto arbitrary substrates. *ACS Nano* 2011, 5, 6916-6924.

145. Caldwell, J. D.; Anderson, T. J.; Culbertson, J. C.; Jernigan, G. G.; Hobart, K. D.; Kub, F. J.; Tadjer, M. J.; Tedesco, J. L.; Hite, J. K.; Mastro, M. A.; Myers-Ward, R. L.; Eddy, C. R.; Campbell, P. M.; Gaskill, D. K. Technique for the Dry Transfer of Epitaxial Graphene onto Arbitrary Substrates. *ACS Nano* 2010, 4, 1108-1114.

146. Bae, S.; Kim, H.; Lee, Y.; Xu, X.; Park, J.-S.; Zheng, Y.; Balakrishnan, J.; Lei, T.; Ri Kim, H.; Song, Y. I.; Kim, Y.-J.; Kim, K. S.; Ozyilmaz, B.; Ahn, J.-H.; Hong, B. H.; Iijima, S. Roll-to-roll production of 30-inch graphene films for transparent electrodes. *Nat Nano* 2010, 5, 574-578.

147. Kang, J.; Hwang, S.; Kim, J. H.; Kim, M. H.; Ryu, J.; Seo, S. J.; Hong, B. H.; Kim, M. K.; Choi, J.-B. Efficient Transfer of Large-Area Graphene Films onto Rigid Substrates by Hot Pressing. *ACS Nano* 2012, 6, 5360-5365.

148. Neumann, P. L.; Tovari, E.; Csonka, S.; Kamaras, K.; Horvath, Z. E.; Biro, L. P. Large scale nanopatterning of graphene. *Nuclear Instruments & Methods in Physics Research Section B-Beam Interactions with Materials and Atoms* 2012, 282, 130-133.

149. Hong, J.; Park, M. K.; Lee, E. J.; Lee, D.; Hwang, D. S.; Ryu, S. Origin of New Broad Raman D and G Peaks in Annealed Graphene. *Scientific Reports* 2013, 3.

150. Jiang, J. W.; Wang, B. S.; Rabczuk, T. Why twisting angles are diverse in graphene Moire patterns? *Journal of Applied Physics* 2013, 113.

151. Ferrari, A. C. Raman spectroscopy of graphene and graphite: Disorder, electron-phonon coupling, doping and nonadiabatic effects. *Solid State Commun.* 2007, 143, 47-57.

152. Gupta, A.; Chen, G.; Joshi, P.; Tadigadapa, S.; Eklund, P. C. Raman scattering from high-frequency phonons in supported n-graphene layer films. *Nano Letters* 2006, 6, 2667-2673.
153. Tang, B.; Hu, G. X.; Gao, H. Y. Raman Spectroscopic Characterization of Graphene. *Applied Spectroscopy Reviews* 2010, 45, 369-407.
154. Ferrari, A. C.; Basko, D. M. Raman spectroscopy as a versatile tool for studying the properties of graphene. *Nature Nanotechnology* 2013, 8, 235-246.
155. Popov, V. N.; Lambin, P. Theoretical polarization dependence of the two-phonon double-resonant Raman spectra of graphene. *European Physical Journal B* 2012, 85.
156. Dippel, B. Raman scattering intensity.
<http://www.raman.de/htmlEN/basics/intensityEng.html>.
157. Pimenta, M. A.; Dresselhaus, G.; Dresselhaus, M. S.; Cancado, L. G.; Jorio, A.; Saito, R. Studying disorder in graphite-based systems by Raman spectroscopy. *Physical Chemistry Chemical Physics* 2007, 9, 1276-1291.
158. Cancado, L. G.; Jorio, A.; Ferreira, E. H. M.; Stavale, F.; Achete, C. A.; Capaz, R. B.; Moutinho, M. V. O.; Lombardo, A.; Kulmala, T. S.; Ferrari, A. C. Quantifying Defects in Graphene via Raman Spectroscopy at Different Excitation Energies. *Nano Letters* 2011, 11, 3190-3196.
159. Cancado, L. G.; Pimenta, M. A.; Neves, B. R. A.; Dantas, M. S. S.; Jorio, A. Influence of the atomic structure on the Raman spectra of graphite edges. *Physical Review Letters* 2004, 93.
160. Yu, Q. K.; Jauregui, L. A.; Wu, W.; Colby, R.; Tian, J. F.; Su, Z. H.; Cao, H. L.; Liu, Z. H.; Pandey, D.; Wei, D. G.; Chung, T. F.; Peng, P.; Guisinger, N. P.; Stach, E. A.; Bao, J. M.; Pei, S. S.;

- Chen, Y. P. Control and characterization of individual grains and grain boundaries in graphene grown by chemical vapour deposition. *Nature Materials* 2011, 10, 443-449.
161. Lahiri, J.; Lin, Y.; Bozkurt, P.; Oleynik, II; Batzill, M. An extended defect in graphene as a metallic wire. *Nature Nanotechnology* 2010, 5, 326-329.
162. Ni, Z. H.; Wang, Y. Y.; Yu, T.; Shen, Z. X. Raman Spectroscopy and Imaging of Graphene. *Nano Research* 2008, 1, 273-291.
163. Ferrari, A. C.; Meyer, J. C.; Scardaci, V.; Casiraghi, C.; Lazzeri, M.; Mauri, F.; Piscanec, S.; Jiang, D.; Novoselov, K. S.; Roth, S.; Geim, A. K. Raman spectrum of graphene and graphene layers. *Physical Review Letters* 2006, 97.
164. Graf, D.; Molitor, F.; Ensslin, K.; Stampfer, C.; Jungen, A.; Hierold, C.; Wirtz, L. Spatially resolved raman spectroscopy of single- and few-layer graphene. *Nano Letters* 2007, 7, 238-242.
165. Bostwick, A. In *Coexisting massive and massless Dirac fermions in symmetry-broken bilayer graphene*, APS March Meeting, Denver, CO, Denver, CO, 2014.
166. Carozo, V.; Almeida, C. M.; Fragneaud, B.; Bede, P. M.; Moutinho, M. V. O.; Ribeiro-Soares, J.; Andrade, N. F.; Souza Filho, A. G.; Matos, M. J. S.; Wang, B.; Terrones, M.; Capaz, R. B.; Jorio, A.; Achete, C. A.; Cancado, L. G. Resonance effects on the Raman spectra of graphene superlattices. *Physical Review B* 2013, 88.
167. Ni, Z.; Wang, Y.; Yu, T.; You, Y.; Shen, Z. Reduction of Fermi velocity in folded graphene observed by resonance Raman spectroscopy. *Physical Review B* 2008, 77.
168. Jorio, A.; Cancado, L. G. Raman spectroscopy of twisted bilayer graphene. *Solid State Commun.* 2013, 175, 3-12.

169. Cocemasov, A. I.; Nika, D. L.; Balandin, A. A. Phonons in twisted bilayer graphene. *Physical Review B* 2013, 88.
170. Wang, Y.; Su, Z.; Wu, W.; Nie, S.; Xie, N.; Gong, H.; Guo, Y.; Lee, J. H.; Xing, S.; Lu, X.; Wang, H.; Lu, X.; McCarty, K.; Pei, S.-s.; Robles-Hernandez, F.; Hadjiev, V. G.; Bao, J. Resonance Raman spectroscopy of G-line and folded phonons in twisted bilayer graphene with large rotation angles. *Applied Physics Letters* 2013, 103.
171. Carozo, V.; Almeida, C. M.; Ferreira, E. H. M.; Cancado, L. G.; Achete, C. A.; Jorio, A. Raman Signature of Graphene Superlattices. *Nano Letters* 2011, 11, 4527-4534.
172. Lee, C.; Yan, H.; Brus, L. E.; Heinz, T. F.; Hone, J.; Ryu, S. Anomalous Lattice Vibrations of Single- and Few-Layer MoS₂. *Acs Nano* 2010, 4, 2695-2700.
173. Georgiou, T.; Jalil, R.; Belle, B. D.; Britnell, L.; Gorbachev, R. V.; Morozov, S. V.; Kim, Y. J.; Gholinia, A.; Haigh, S. J.; Makarovskiy, O.; Eaves, L.; Ponomarenko, L. A.; Geim, A. K.; Novoselov, K. S.; Mishchenko, A. Vertical field-effect transistor based on graphene-WS₂ heterostructures for flexible and transparent electronics. *Nature Nanotechnology* 2013, 8, 100-103.
174. Zhan, Y. J.; Liu, Z.; Najmaei, S.; Ajayan, P. M.; Lou, J. Large-Area Vapor-Phase Growth and Characterization of MoS₂ Atomic Layers on a SiO₂ Substrate. *Small* 2012, 8, 966-971.
175. Lee, Y. H.; Zhang, X. Q.; Zhang, W. J.; Chang, M. T.; Lin, C. T.; Chang, K. D.; Yu, Y. C.; Wang, J. T. W.; Chang, C. S.; Li, L. J.; Lin, T. W. Synthesis of Large-Area MoS₂ Atomic Layers with Chemical Vapor Deposition. *Advanced Materials* 2012, 24, 2320-2325.
176. Wang, X. S.; Feng, H. B.; Wu, Y. M.; Jiao, L. Y. Controlled Synthesis of Highly Crystalline

- MoS₂ Flakes by Chemical Vapor Deposition. *Journal of the American Chemical Society* 2013, 135, 5304-5307.
177. Splendiani, A.; Sun, L.; Zhang, Y.; Li, T.; Kim, J.; Chim, C.-Y.; Galli, G.; Wang, F. Emerging Photoluminescence in Monolayer MoS₂. *Nano Letters* 2010, 10, 1271-1275.
178. Zhao, W.; Ghorannevis, Z.; Chu, L.; Toh, M.; Kloc, C.; Tan, P.-H.; Eda, G. Evolution of Electronic Structure in Atomically Thin Sheets of WS₂ and WSe₂. *Acs Nano* 2013, 7, 791-797.
179. Mak, K. F.; Lee, C.; Hone, J.; Shan, J.; Heinz, T. F. Atomically Thin MoS₂: A New Direct-Gap Semiconductor. *Physical Review Letters* 2010, 105.
180. van der Zande, A. M.; Huang, P. Y.; Chenet, D. A.; Berkelbach, T. C.; You, Y.; Lee, G.-H.; Heinz, T. F.; Reichman, D. R.; Muller, D. A.; Hone, J. C. Grains and grain boundaries in highly crystalline monolayer molybdenum disulphide. *Nature Materials* 2013, 12, 554-561.
181. Gutierrez, H. R.; Perea-Lopez, N.; Elias, A. L.; Berkdemir, A.; Wang, B.; Lv, R.; Lopez-Urias, F.; Crespi, V. H.; Terrones, H.; Terrones, M. Extraordinary Room-Temperature Photoluminescence in Triangular WS₂ Monolayers. *Nano Letters* 2013, 13, 3447-3454.
182. Cong, C.; Shang, J.; Wu, X.; Cao, B.; Peimyoo, N.; Qiu, C.; Sun, L.; Yu, T. Synthesis and Optical Properties of Large-Area Single-Crystalline 2D Semiconductor WS₂ Monolayer from Chemical Vapor Deposition. *Advanced Optical Materials* 2014, 2, 131-136.

APPENDIX I: JOURNAL PUBLICATIONS

- **Yanan Wang**, Zhihua Su, Wei Wu, Shu Nie, Xinghua Lu, Haiyan Wang, Kevin McCarty, Shin-Shem Pei, Francisco Robles-Hernandez, Viktor G. Hadjiev, Jiming Bao. “Four-fold Raman Enhancement of 2D Band in Twisted Bilayer Graphene: Evidence for Doubly Degenerate Dirac Band and Quantum Interference”, *Nanotechnology* 25, 335201 (2014).
- **Yanan Wang**, Archana Kar, Andrew Paterson, Katerina Kourentzi, Han Le, Paul Ruchhoeft, Richard Willson, and Jiming Bao. “Transmissive Nanohole Arrays for Massively-Parallel Optical Biosensing”, *ACS Photonics* 1, 241-245 (2014).
- Longb Liao, Qiuhui Zhang, Zhihua Su, Zhongzheng Zhao, **Yanan Wang**, Yang Li, Xiaoxiang Lu, Dongguang Wei, Guoying Feng, Qingkai Yu, Xiaojun Cai, Jimin Zhao, Zhifeng Ren, Hui Fang, Francisco Robles-Hernandez, Steven Baldelli, Jiming Bao. “Efficient Solar Water-Splitting Using A Nanocrystalline CoO Photocatalyst”, *Nature Nanotechnology* 9, 69–73 (2014).
- **Yanan Wang**, Zhihua Su, Wei Wu, Shu Nie, Nan Xie, Huiqi Gong, Yang Guo, Joon Hwan Lee, Sirui Xing, Xiaoxiang Lu, Haiyan Wang, Xinghua Lu, Kevin McCarty, Shin-Shem Pei, Francisco Robles-Hernandez, Viktor G. Hadjiev and Jiming Bao. “Resonance Raman Spectroscopy of G-Line and Folded Phonons in Twisted Bilayer Graphene with Large Rotation Angles”, *Applied Physics Letters* 103, 123101 (2013).
- Sirui Xing, Wei Wu, **Yanan Wang**, Jiming Bao, Shin-Shem Pei. “Kinetic Study of Graphene Growth: Temperature Perspective on Growth Rate and Film Thickness by Chemical Vapor Deposition”, *Chemical Physics Letters* 580, 62-66 (2013).

- Jiming Bao, Sirui Xing, **Yanan Wang**, Wei Wu, Francisco Robles-Hernandez, Shin-Shem Pei. “Fabrication of Large-Area Twisted Bilayer Graphene for High-Speed Ultra-Sensitive Tunable Photodetectors”, *Proceedings of SPIE 8725*, 872503 (2013) (Invited Paper).
- Rui He, Ting-Fung Chung, Conor Delaney, Courtney Keiser, Luis A. Jauregui, Paul M. Shand, C. C. Chancey, **Yanan Wang**, Jiming Bao, and Yong P. Chen. “Observation of Low Energy Raman Modes in Twisted Bilayer Graphene”, *Nano Letter* 13, 3594-3601 (2013).
- Wei Wu, Debtanu De, Su-Chi Chang, **Yanan Wang**, Haibing Peng, Jiming Bao, Shin-Shem Pei. “High Mobility and High On/Off Ratio Field-Effect Transistors Based on Chemical Vapor Deposited Single-Crystal MoS₂ Grains”, *Applied Physics Letters* 102, 142106 (2013).

APPENDIX II: CONFERENCE PRESENTATIONS

- **Yanan Wang**, Sirui Xing, Xiaoxiang Lu, Francisco Robles-Hernandez, Shin-Shem Pei, Jiming Bao. “Twisted Bilayer Graphene with Controlled Rotation Angles”, APS March Meeting, Denver, CO, 2014.
- **Yanan Wang**, Archana Kar, Andrew Paterson, Katerina Kourentzi, Paul Ruchhoeft, Richard Willson, Jiming Bao. “Optical Imaging Based Nanohole System for Ultrasensitive Bio-Detection”, 245th ACS National Meeting, New Orleans, LA, 2013.
- **Yanan Wang**, Zhihua Su, Wei Wu, Sirui Xing, Xiaoxiang Lu, Xinghua Lu, Shin-Shem Pei, Francisco Robles-Hernandez, Viktor G. Hadjiev and Jiming Bao. “Folded Optical Phonons in Twisted Bilayer Graphene: Raman Signature of Graphene Superlattices”, APS March Meeting, Baltimore, MD, 2013.
- **Yanan Wang**, Yiyan Zheng, Zhihong Liu, Peng Peng, Qilin Cao and Jiming Bao. “Nano-Engineered Multi-Channel Scaffolds for Axon Regeneration”, MRS Fall Meeting, Boston, MA, 2010.

